LOCAL STRUCTURE AND STRUCTURAL SIGNATURE UNDERLYING PROPERTIES IN METALLIC GLASSES AND SUPERCOOLED LIQUIDS

by

Jun Ding

A dissertation submitted to Johns Hopkins University in conformity with the requirements for the degree of Doctor of Philosophy

Baltimore, Maryland

September, 2014

Abstract

Metallic glasses (MGs), discovered five decades ago as a newcomer in the family of glasses, are of current interest because of their unique structures and properties. There are also many fundamental materials science issues that remain unresolved for metallic glasses, as well as their predecessor above glass transition temperature, the supercooled liquids. In particular, it is a major challenge to characterize the local structure and unveil the structure-property relationship for these amorphous materials. This thesis presents a systematic study of the local structure of metallic glasses as well as supercooled liquids via classical and *ab initio* molecular dynamics simulations. Three typical MG models are chosen as representative candidate, $Cu_{64}Zr_{36}$, $Pd_{82}Si_{18}$ and $Mg_{65}Cu_{25}Y_{10}$ systems, while the former is dominant with full icosahedra short-range order and the prism-type short-range order dominate for latter two. Furthermore, we move to unravel the underlying structural signature among several properties in metallic glasses. Firstly, the temperature dependence of specific heat and liquid fragility between Cu-Zr and Mg-Cu-Y (also Pd-Si) in supercooled liquids are quite distinct: gradual versus fast evolution of specific heat and viscosity/relaxation time with undercooling. Their local structural ordering are found to relate with the temperature dependence of specific heat and relaxation time. Then elastic heterogeneity has been studied to correlate with local structure in Cu-Zr MGs. Specifically, this part covers how the degree of elastic deformation correlates with the internal structure at the atomic level, how to quantitatively evaluate the local

solidity/liquidity in MGs and how the network of interpenetrating connection of icosahedra determine the corresponding shear modulus. Finally, we have illustrated the structure signature of quasi-localized low-frequency vibrational normal modes, which resides the intriguing vibrational properties in MGs. Specifically, the local atomic packing structure in a model MG strongly correlate with the corresponding participation fraction in quasi-localized soft modes, while the highest and lowest participation correspond to geometrically unfavored motifs and ISRO respectively. In addition, we clearly demonstrate that quasi-localized low-frequency vibrational modes correlate strongly with fertile sites for shear transformations in a MG.

(Advisor: Prof. En Ma)

(Reader: Prof. Michael Falk)

Dedicated to my family

Acknowledgements

First and foremost, I am grateful to my advisor, Prof. En Ma, who is always thoughtful and considerate to students and gives me lots of guidance and encouragement during my PhD study at the Johns Hopkins University. Starting as a fresh graduate student when I entered JHU four years ago, Prof. Ma sets the example of academic research by insightful and critical thoughts, as well as passion towards solving scientific challenge. It's a great experience to learn from Prof. Ma how to find valuable topics, how to think rigorously and critically, how to conduct research and organize a paper during the past few years. Besides, sufficient research freedom is always allowed by Prof. Ma, and it's helpful for me to explore my interested fields and develop my ability of independent research.

I would like to thank my defense committee members, Prof. Michael Falk, Prof. Robert Cammarata, Prof. Somnath Ghosh and Prof. Jaafar El-Awady. Your critical reading of my thesis and insightful comments are greatly appreciated. Especially, I am indebted to Prof. Michael Falk as the second reader for important suggestions of writing the thesis.

I am grateful to the former and current group member for valuable discussions and collaborations. Especially I worked closely with Dr. Yongqiang Cheng, Dr. Ming Xu as well as Prof. Howard Sheng in the past years and they guided me to start up my

scientific research at JHU. I also thank Mr. Qingjie Li and Ms. Lin Tian as well as all my friends at JHU, for their help on my work and daily life.

I also thank to many other collaborators during my PhD study for their marvelous work, valuable discussion and critical comments. At Hopkins, I learned a lot of computer simulation techniques and analysis methodologies from Dr. Pengfei Guan and Dr. Sylvain Patinet, while Mr. Shengwei Deng taught me MD simulation upon polymer materials. In addition, I appreciate the host by Prof. Zhiwei Shan and Prof. Jun Sun at XJTU.

I own many thanks to Marge Weaver, Dot Reagle, Jeanine Majewski and Ada Simari for their assistance in the administrative issues. The financial support from the US National Science Foundation and Department of Energy are also sincerely acknowledged.

Last but not least, I am grateful to my beloved wife Yuan and my dearest unborn baby daughter. They are the most powerful faith that supports my pursuit in my everyday life and work. Also, my parents are always supportive and patient during my study at Hopkins. I am greatly indebted to their deepest love.

Contents

List of Tables

List of Figures

List of Abbreviations and Symbols

AIMD: *ab initio* molecular dynamics

AQS: athermal quasi-static shear

BMG: bulk metallic glass

BOO: bond orientational order

CN: coordination number

CNA: common neighbor analysis

CPE: configurational potential energy

DFT: density functional theory

DOS: density of states

EAM: embedded atom method

ELF: electron localization function

FI: full icosahedra

FISRO: full icosahedra short-range order

GFA: glass-forming ability

GUM: geometrically unfavored motif

ICOI: interpenetrating connection of icosahedra

IS: inherent structure

MC: Monte Carlo

MD: molecular dynamics

MG: metallic glass

MRO: medium-range order

NN: nearest neighbor

NPT: constant number, pressure and temperature

NVT: constant number, volume and temperature

PDF: pair distribution function

PEL: potential energy landscape

RMC: reverse Monte Carlo

SRO: short-range order

STZ: shear transformation zone

TEM: transmission electron microscopy

VASP: Vienna *ab initio* simulation package

PAW: projector augmented-waves

VDOS: vibrational density of states

XRD: X-ray diffraction

G: shear modulus

B: bulk modulus

υ: Poisson's ratio

C_{ij}: elastic constant

η: viscosity

T_g: glass transition temperature

T_l: liquidus temperature

T_R: room temperature

W: activation energy barrier

$\boldsymbol{P}_i$: participation fraction of ith atom

D^2_{min}: non-affine displacement

X_{icos}: fraction of Cu-centered full icoshedra

Chapter 1

Introduction

Metallic glasses (MGs) are solid metallic materials, usually alloys, with a disordered atomic-level structure (8-12). Their counterparts, crystalline metals, have been extensively studied and widely used for a long time (13-15). These two categories of metallic materials have been discovered to possess different properties, and developed more or less independently. Since the discovery of the first MG several decades ago (8), there has been increasing interests in developing and understanding this new family of materials (8-12). In crystalline metals and alloys, atoms reside on a crystalline lattice with

Parts of this thesis have been published in Refs.(1-7)

long-range translational order (16, 17). In contrast, metallic glasses are amorphous or "structure-less" without long-range structural correlation (18-20). Thus, the distinct atomic and electronic structures underlying the contrasting properties of metals and metallic glasses exist. Among the many unresolved puzzles, the atomic-level structure and structure-property relationship are one of the central topics (18-22). In this thesis, we will focus on the structural aspect of MGs, as well as the structural basis for their various properties. This will help us better understand metallic glasses and their structure-properties relationship.

1.1. Metallic glasses and supercooled liquids

Glasses are usually made by rapid quenching of melts via dynamic arrest, thus glasses are essentially "frozen" liquids (23-27). As illustrated in the schematic TTT diagram in Figure 1-1, liquids can encounter the crystal phase nose with enough allowed time (see yellow arrow) when temperature (T) is below the liquidus temperature (T_l). In order to form amorphous structure from frozen liquids, faster cooling rates are needed to bring the liquid to glass transition at the glass transition temperature, T_g, before the crystals have enough time to undergo nucleation and growth (see black arrow in Figure1-1). R_c is the critical cooling rate that divided glass transition and crystallization for quenched melts.

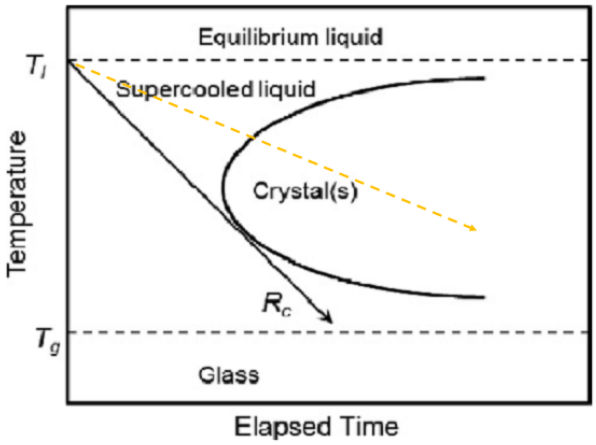

Figure 1-1. A schematic TTT diagram to describe glass transition.

The temperature dependences of a liquid's volume or enthalpy are plotted in Figure 1-2 (23). Crystallization is a typical first order phase transition with abrupt change of volume, enthalpy etc. at the melting temperature (28). But for glass transition, it is a process of dynamical arrest as indicated in Figure 1-2. Different cooling rates render different glass transition temperatures or fictive temperatures: glasses with slower cooling rate exhibit lower glass transition temperature and vice versa. Furthermore, glasses quenched with slower cooling rate are associated with "older" configurations, which show higher density, lower internal energy, higher elastic modulus etc. (6, 29-33) The origin of the terminology "older" comes from the phenomenology of aging during annealing below T_g.(23, 34, 35)

Metallic alloys are relatively easy to crystallize upon solidification, compared to the common glass formers such as organic materials or silicate. Thus it's more difficult to produce metallic glasses especially at bulk scale by suppressing crystallization, which is one of the most serious challenges that the MGs community encountered for several

decades (36). Traditionally, most MGs with excellent glass forming ability (GFA) were determined by a sequential and time-consuming trial-and-error approach, which is a daunting task especially for multicomponent BMGs, even though some advanced techniques have been designed to achieve high-throughput (37, 38) During past years, some empirical rules have been developed to carefully select constituent elements and optimize the composition in order to produce metallic alloys with excellent GFA. For instance, Inoue insightfully proposed three empirical rules (12) : metallic alloys with more than three elements, atomic size mismatch above 12%, and negative heat of mixing between the components; such systems exhibit better GFA. The underlying mechanism of these rules, as noted by Inoue (12), may be related to the atomic-level structure, including local topological and chemical ordering, as well as the electronic structure and the nature of bonding. Those good metallic glass-formers can be made by relatively slow cooling rates and, consequently, with larger thickness.

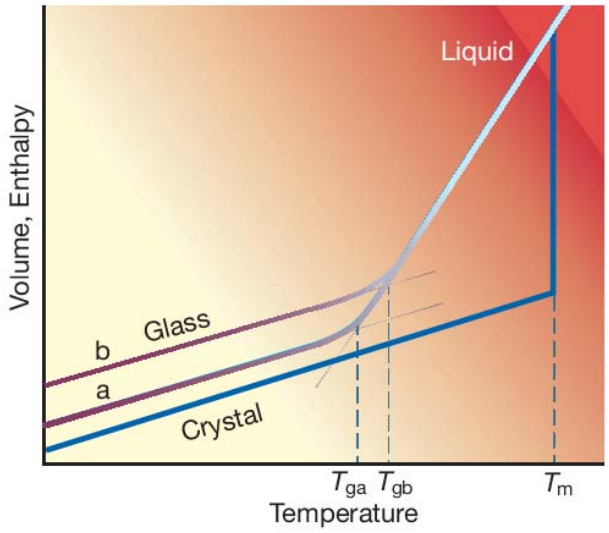

Figure 1-2. Schematic description of temperature dependence of a liquid's volume or enthalpy during crystallization and glass transition. (23)

1.2. Structure of metallic glasses

The exceptional performances of metallic glasses have pushed the research on their structural characterization since their discovery. However, unlike their crystalline metallic alloy counterparts, metallic glasses look “structure-less” and have no long-range translational order. This makes their structural characterization quite challenging. A variety of experimental and computational techniques are utilized to study the structure of metallic glasses. The former includes X-ray/neutron diffraction (39-44), X-ray absorption fine structure (45-49), fluctuation electron microscopy (50-52), transmission electron microscopy (53, 54) and nuclear magnetic resonance (55-57) etc., while the latter covers the molecular dynamics simulation (58-62) and reverse Monte Carlo modelling (63-65) etc. Current advances, such as the technique of nanobeam electron microscopy make the direct observation of local structure in metallic glasses possible (66, 67). Until now, several models have been proposed to describe the short-to-medium range order in metallic glasses. Although they have already been well studied in this field, there still remains vast room for better understanding the structure in metallic glasses, especially from the perspective beyond the short-range scale.

1.2.1. Theoretical models

Early structural models for glasses have been proposed, such as dense random packing of hard spheres (68-70) , Gaskell’s stereochemical model (71), etc., but they are insufficient to describe the structure of MGs. That’s mainly because the atomic packing is

dense, and the non-directional metallic bonding in metallic glasses are relatively flexible, unlike silicate or organic glasses from which many early models were inspired from (72). For the SRO in MGs, if only the spherical packing efficiency of the nearest neighbors is considered, local icosahedral order (see Figure 1-3) is even more efficient than face-centered-cubic (fcc) or hexagonal order, although icosahedra alone cannot be repeated to fully fill up the 3D space.

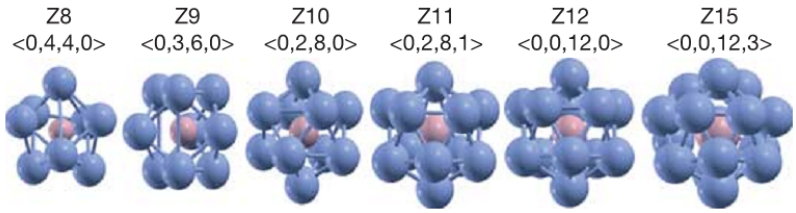

Figure 1-3. Schematic plot of Kasper polyhedra with corresponding CNs. (19)

In recent years, the model of "efficient packing of solute-centered clusters" has been developed to characterize the structure of MGs, as illustrated in Figure 1-4 (18-20, 73, 74). In this proposed model, the solute-centered cluster with solvent atoms in the nearest-neighbor shell as schematically described in Figure 1-3, is the basic building block of MG and those quasi-equivalent clusters are arranged to pack the 3D space efficiently. There are two main proposed schemes about how those quasi-equivalent clusters pack. One is F.C.C pattern for local packing of quasi-equivalent clusters as described in Figure 1-4 (a-b), which was firstly introduced by Miracle (20). The other packing scheme is to form icosahedra-like order (five-fold symmetry) among local quasi-

equivalent clusters (19, 73), as seen in Figure 1-4 (c-d). Such packing features of quasi-efficient cluster are then indicated to be the characteristic medium-range order (MRO) in solute-lean MGs. Those advances are instructive and inspiring, but it's still insufficient to fully describe MRO among general kinds of MGs because majority of MGs family are not lean in solute and are usually multi-component (more than two constituent elements). In the case of multicomponent BMGs or non-solute-lean, the task to satisfyingly develop theoretical models and describe their structural features beyond short range still remains quite challenging.

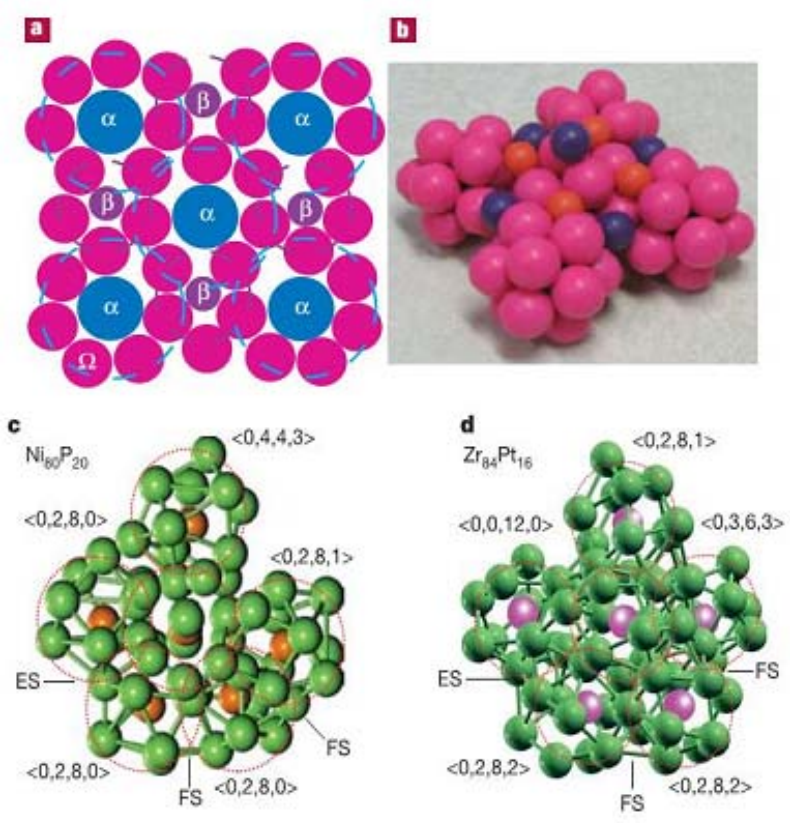

Figure 1-4. Efficient packing of solute centered clusters to describe short-to-medium range order in metallic glasses. (19, 20)

In addition, other models have been proposed to illustrate the structure of metallic glasses. For example, on the basis of neutron and X-ray diffraction experiments, the self-similar packing of atomic clusters has been proposed (75, 76). They show that the medium-range order has the characteristics of a fractal network with a dimension of $n<3$ (2.31 for (75) and 2.5 for (76)), and is described by a power-law correlation function over the medium-range length scale.

Finally, since the distribution of local structure (as well as various local properties) in metallic glasses are continuous: span the limit from order to disorder, there would be question in depth upon their structural models: is a simple structural model appropriate or useful for those amorphous materials? More study will be needed in the future to better describe the structural feature among amorphous alloys.

1.2.2. Topological structural analysis methods

It's crucial to define structural parameters that can describe the structure of an MG. Unlike the methods and techniques implemented for crystals, this necessarily requires a more complex way to characterize internal structure in MGs given multiplicity inherent in amorphous configurations. Specifically, to look into the glass structure by the statistical information may be more relevant than the well-defined ideal structures by which we commonly characterize crystalline materials. We briefly introduce several commonly used structural parameters to describe the structure of MGs.

1.2.2.1. Pair distribution function

Pair distribution function (PDF) is a two-body pair correlation that describes the distribution of distances (r) between pairs of particles contained within a given volume. It is independent of orientation and can be directly calculated from physical measurements like light scattering or x-ray powder diffraction through the use of a Fourier Transform. The partial PDF is defined as (18, 77):

$$g_{ab}(r) = \frac{N}{4\pi r^2 \rho N_a N_b} \sum_{i=1}^{N_a} \sum_{j=1}^{N_b} \delta\left(\left|\vec{r}_{ij} - r\right|\right) \tag{1-1}$$

where N_a and N_b are the number of atoms of type a and type b, respectively and ρ is the number density of atoms in the system . r_{ij} is the interatomic distance between two atoms i (of type a) and atom j (of type b). This definition of PDFs are for isotropic materials, while anisotropic amorphous materials can be evaluated by anisotropic PDFs, which has been discussed in (78).

1.2.2.2. Structure factor

In condensed matter physics and crystallography, the structure factor is a mathematical description of how a material scatters incident radiation. In reciprocal space, the partial structure factors can be calculated from the partial PDFs via Fourier transformation (18),

$$S_{ab}(q) - 1 = \frac{4\pi\rho}{q} \int_0^\infty r\left[g_{ab}(r) - 1\right] \sin(qr) dr \tag{1-2}$$

where q is the variable in the reciprocal space, which corresponds to the magnitude of the diffraction vector ($4\pi\sin\theta/\lambda$) under X-ray.

1.2.2.3. Common neighbor analysis

Common neighbor analysis (CNA) is an indicator of topological order between neighboring atoms (18). Each pair of neighboring atoms has a CNA characterized by a three number index, *ijk* (for example, 555, 444, 533 etc). The three number index correspond respectively to 1) the number of nearest neighbors shared to both atoms in the specific pair; 2) the number of bonds between the shared nearest neighbors themselves; 3) the number of bonds in the longest continuous chain formed by the *j* bonds. Using CNA, different local atomic arrangements can be characterized, such as icosahedral order, crystal-like order etc (19, 79).

1.2.2.4. Voronoi tessellation

The Voronoi tessellation (18, 80) is a way to divide the space into cells centered at each atom. The cell is formed by planes that are drawn to bisect each line connecting the center atom and each neighboring atom, and the Voronoi cell is the space enclosed by all the inner planes and the part of space is closer to the center atom than any other atoms. This method can be used to unambiguously determine the CN without the need of a cutoff: those and only those atoms sharing a common cell surface are considered nearest neighbors. For MGs with more than one species, the bisection can be weighted by the atomic size. Faces of Voronoi cell with area smaller than a small fraction (e.g., 0.25%) of the total area are discounted as negligible partition error. The four-number Voronoi index, $<i_3, i_4, i_5, i_6>$, describes the arrangement and topology of the nearest-neighbor atoms around the center atom. Specifically, i_3 represents the number of triangles on the Voronoi

polyhedron, i_4 the number of quadrangles, i_5 the number of pentagons, and i_6 the number of hexagons. In metallic glasses, five-fold symmetry (n_5) is quite important (e.g. <0, 0, 12, 0> for full icosahedra motifs in MGs) compared with crystalline materials. Via Voronoi tessellation, the Voronoi volume can be obtained as an evaluation of the atomic volume.

1.2.2.5. Bond orientational order

Bond orientational order (BOO) (18, 81, 82) associates a set of spherical harmonics with every bond joining an atom to surrounding nearest neighbor atoms. For each nearest neighbor bond, the polar angles of the bond measured with respect to an external coordinate system are used to calculate the spherical harmonics:

$$Q_{lm}(\vec{r}) \equiv Y_{lm}(\theta(\vec{r}), \phi(\vec{r})) \tag{1-3}$$

where $Y_{lm}(\theta(\vec{r}), \phi(\vec{r}))$ are spherical harmonics and $\theta(\vec{r}), \phi(\vec{r})$ are the polar angles. It's important to consider rotationally invariant combinations, such as:

$$Q_l \equiv \left[\frac{4\pi}{2l+1} \sum_{m=-l}^{l} \left| \bar{Q}_{lm} \right|^2 \right]^{1/2} \tag{1-4}$$

and

$$W_l \equiv \sum_{m_1, m_2, m_3, m_1+m_2+m_3=0} \begin{bmatrix} l & l & l \\ m_1 & m_2 & m_3 \end{bmatrix} \times \bar{Q}_{lm_1} \bar{Q}_{lm_2} \bar{Q}_{lm_3} \tag{1-5}$$

The coefficients

$$\begin{bmatrix} l & l & l \\ m_1 & m_2 & m_3 \end{bmatrix}$$

is the third order invariants are Wigner 3*j* symbols.

1.3. Properties of metallic glasses and supercooled liquids

The MGs combine "structure-less" features with metallic bonding, exhibiting atomic configurations quite different from their crystalline counterparts. Thus, the intrinsic properties of these two categories of materials are also different. In this section, several typical properties of MGs will be introduced, including their thermodynamic, kinetic, vibrational and mechanical behaviors. The underlying structural origins of those properties are the main focus of this thesis. This introduction of properties of MGs provides grounds for detailed structure-property relationships, which will be discussed in the following sections.

1.3.1. Thermodynamic and kinetic properties

The thermodynamics and kinetics of supercooled liquids are essential to understanding glass formation or crystallization (10, 23, 25, 26, 83-89). In fact, the supercooled liquid is where all the mysteries of glasses originate from. The driving force towards crystallization is the Gibbs free energy difference ΔG between the supercooled liquid and competing crystals (86) when liquids are undercooling with temperature below T_l or T_m. That driving force depends on the undercooling as illustrated in Figure 1-5 (86), where deeper supercooling leads to higher driving force. Obviously, to reduce the chance for crystallization to achieve a high GFA, the increase of ΔG per degree of undercooling should be relatively low in the supercooled regime (from T_l and T_g).

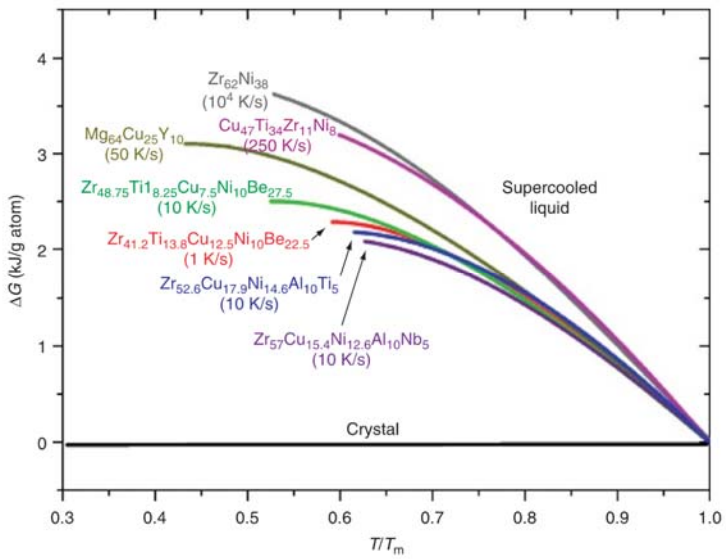

Figure 1-5. Temperature dependence of ΔG (differences in Gibbs free energy between the liquid and the crystalline state) for various metallic glass-forming liquids (86).

At the same time, the specific heat in the supercooled liquid increases upon undercooling towards glass transition (90), as indicated in Figure 1-6. Two contrasting behaviors can be clearly observed: one is relatively shallow evolution of C_p with temperature while the other is rapid increase (86). The supercooled liquids with good GFA exhibit a shallow specific heat curve, and vice versa. The underlying structural origin of this contrasting C_p behavior will be discussed in Section 4 in this thesis.

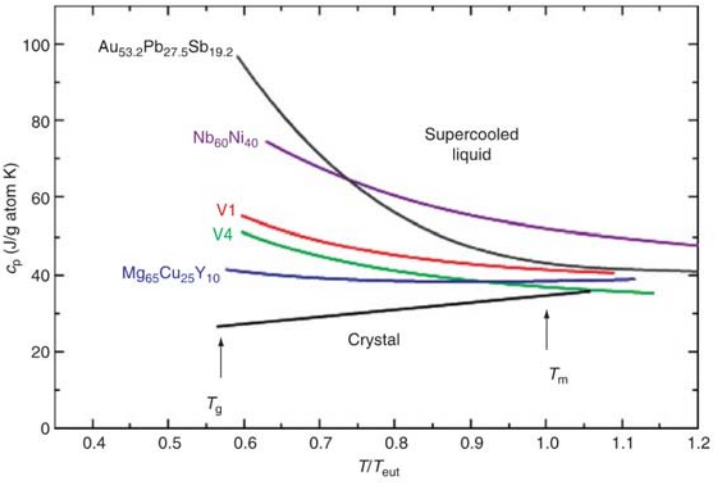

Figure 1-6. Temperature dependence of specific heat capacities in the supercooled liquid for several BMG alloys. (86)

The kinetic properties of supercooled liquids are mainly studied by monitoring the evolution of viscosity (η) or relaxation time with temperature (see Figure 1-7). Apparently, the viscosity decreases exponentially with rising temperature (83), and different liquids exhibit quite different behavior. Some liquids follow the Arrhenius equation, a nearly linear relationship in Angell's plot (such as SiO_2), while for some others the temperature dependence of viscosities in Angell's plot exhibit bending curve with deviation from the linear relationship (83), as indicated in Figure 1-7. Data on the Angell plot in Figure 1-7 can be fitted by the widely used Vogel-Fulcher-Tammann (VFT) equation (58) with the expression $\eta = A\exp\left[\frac{B}{T-T_0}\right]$, where T_0 is the lower limit of T, at which the configurational entropy difference vanishes. The "entropy crisis" has been theorized to correspond to the ideal glass transition at the so-called Kauzmann

temperature, T_K (91). The glass transition temperature occurs, by convention, when the viscosity reaches a critical value (e.g., 10^{12} Pa*s or 10^{13} poise), and the slope at the glass transition in Angell's plot is defined as the fragility (83), $m = \left[\frac{d\eta(T_g/T)}{d(T_g/T)}\right]_{T=T_g}$. Liquids with lower fragility are termed "stronger" (e.g., SiO_2), whereas those with higher fragility are more "fragile" (e.g, o-terphenyl). However, this concept is under careful examination and, the fragile-to-strong transition in metallic glass-forming liquids is an area of ongoing investigation (92-96).

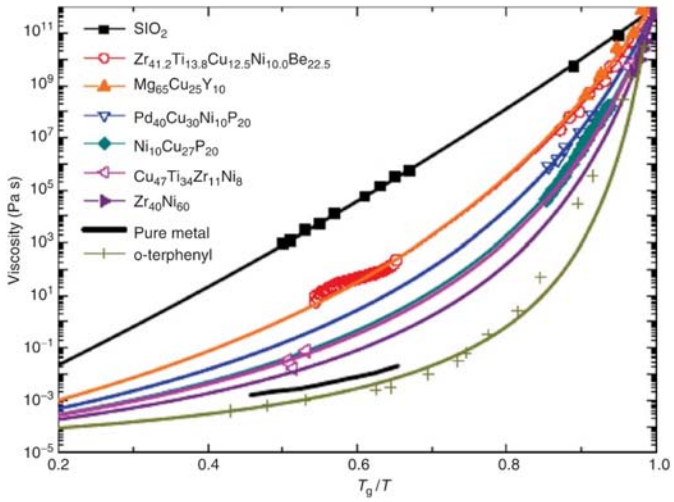

Figure 1-7. Angell plot of the viscosities of different types of glass-forming liquids including oxide, metallic and organic glasses.(86)

In following Section 4, we will discuss the structural signature of different liquid fragility in metallic glass-forming supercooled liquids. Despite the unsolved puzzles, however, it is clear that the evolution trend of energy barrier W ($\eta(T) = \eta_0 \exp(W/kT)$, where η_0 is the high T limit of $\eta(T)$) with temperature is determined by the reduction of

configurational entropy, which is further connected with the structural ordering while the liquid is cooled. In other words, how and how fast (with normalized temperature) the atoms order themselves to reduce the configurational entropy is the underlying structural process behind the evolving viscosity.

1.3.2. Mechanical properties

MGs exhibit quite different mechanical behavior compared to their crystalline counterparts (97-107). One is the elastic heterogeneity. Unlike crystalline metals, elastic deformation of metallic glasses (MGs) is intrinsically non-affine (inhomogeneous). In an *in situ* X-ray experiment on an MG sample under uniaxial loading, the elastic heterogeneity manifests itself as the length-scale dependence of the peak shift in the extracted radial distribution functions (108-111), as well as their unusual orientation dependence (structural anisotropy) (100, 112). Recent studies suggested that there are about ¼ volume fraction of liquid-like sites (112), which are much larger than typical fraction of free volume (around 1-2%). The observation is consistent with the shear modulus of MG, which is 10-30% lower (99, 113, 114) than their corresponding crystalline counterparts. Very recent experiments also report that there are even observable variations in local modulus (115) and local viscoelasticity (116) at the nanometer scale. These are obviously related to the internal structure of the amorphous metals, which are characterized by a hierarchy of local structures (including atomic packing and bonding) with varying degrees of order (2, 4).

Another feature of mechanical deformation in MGs is that the plasticity in MGs are believed to be carried by STZs (117-123), which is a group of ~100 atoms that

transform cooperatively under shear deformation. This behavior is unlike the plasticity carried by dislocations in crystalline alloys (124). Different from dislocations in crystals, STZs prior to loading usually do not exist as obvious defects with distinctly different structure compared to the matrix; they are local groups of atoms responding to the given applied load to produce shear strains. Thus to identify those "soft spots" that are prone to shear transformation will be important to understand mechanical behavior of amorphous alloys (7). In Section 6, we will discuss the structural signature of soft spots characterized by quasi-localized low-frequency vibrational normal modes.

Furthermore, another eye-catching feature of MGs is the very high elastic strain limit: the elastic strain at the onset of yielding is ~2% at room temperature (97, 125) as seen in Figure 1-8 (L, H, C are different BMGs under deformation). This is about one order of magnitude higher than that in conventional crystalline metals and alloys, which is not only much smaller (e.g., 0.2%) but also varies depending on the material and content of defects (124). The ~2% uniaxial yield strain, usually measured in compression tests of BMG samples, corresponds to a shear strain limit of 2.67% (126) .

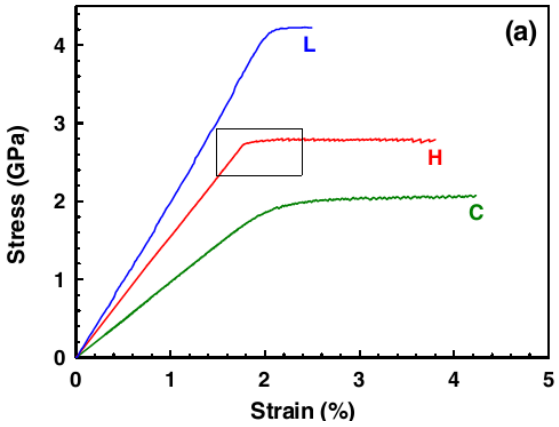

Figure 1-8 Stress-strain curve for typical deformation of BMGs under compression (125).

Recently, Johnson and Samwer (126) developed a cooperative shear model (CSM) from the perspective potential energy landscape (31, 127), which by fitting to available experimental data gives a "universal" expression for the shear strain limit as a function of temperature,

$$\gamma_{MG,C}(T) = \tau_{MG,C}(T)/G = 0.036 - 0.016(T/T_g)^{2/3}, \quad (1\text{-}6)$$

where $\tau_{MG,C}(T)$ is the temperature-dependent shear stress at yielding and T_g is the glass transition temperature (126, 128). The experiments data and Johnson-Samwer equation about yielding limit of BMGs can be seen in Figure 1-9. Interestingly, Eq. (1-6) suggests that $\gamma_{MG,C}$ is identical for all BMGs, at any given T/T_g .(126, 128-130)

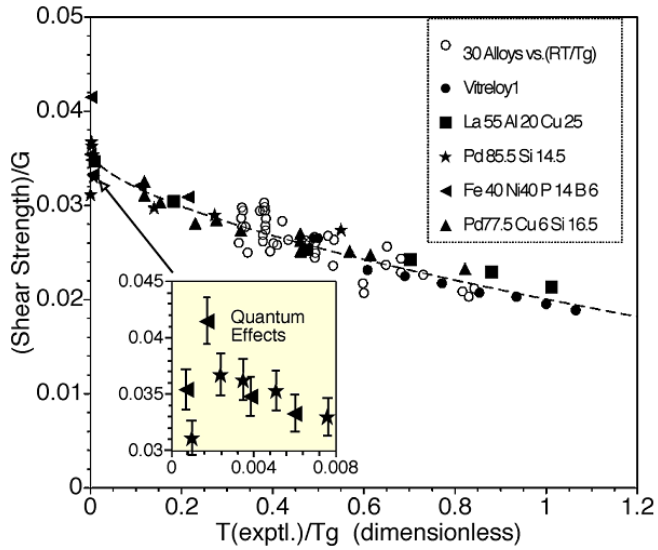

Figure 1-9. Yielding limits of various BMGs determined by experiments, which are fitted by Johnson-Samwer equation with dashed line. (126)

A major shortcoming that prevents MGs from extensive industrial applications is its brittleness at room temperature because of shear softening and auto-catalytic propagation of shear bands (122, 131-136). Monolithic MGs usually exhibit limited compressive plasticity and no tensile ductility. Thus one of the most challenging and crucial task for BMG scientists and engineers is to improve the ductility of BMGs by innovative approaches, such as tuning compositions and constituents, introducing crystalline composites, applying external processing (102, 137-145) or strengthening by nanoscale engineering (146-153).

1.3.3. Vibrational properties

Vibrational properties of MGs are fundamental aspects that can be directly related to their thermodynamic and kinetic behavior. One of the universal features in glasses (including MGs) is the boson peak (BP), which has been observed in neutron and Raman scattering and remains as a serious puzzle in condensed-matter physics and materials science (154-159). The BP is an excess peak at low vibrational frequency over the prediction by Debye theory in $g(\omega)$ (proportional relationship between $g(\omega)$ and ω). Theoretical work suggests that the BP arises from (quasi)localized and anharmonic vibrational modes associated with some defective structures (160-163), although the structural origin for the BP remains unsolved. In Section 6, we attempt to resolve the structural origin of the quasi-localized low-frequency vibrational normal modes by associating these with the atomic packing structure in MGs (7).

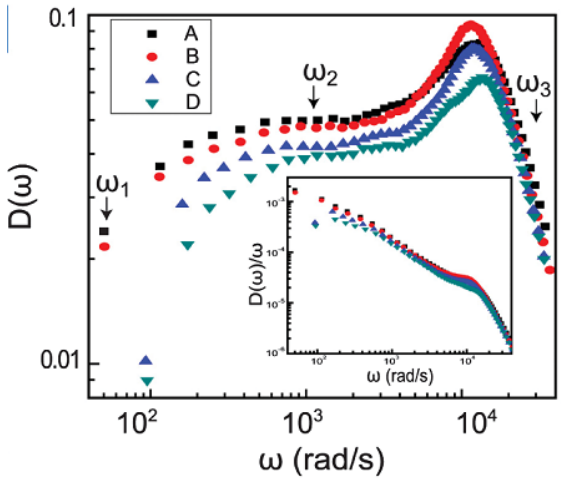

Figure 1-10. The density of states of four glassy models. (164)

1.4. Objective and organization of the thesis

The objective of this thesis work is to improve our understanding of the properties of metallic glasses and supercooled liquids from a structural perspective. We aim to systematically probe the local structure of metallic glasses via classical and *ab initio* molecular dynamics simulations. Through those investigation we will monitor how the evolution of local structures leads to different temperature dependence of the specific heat and relaxation in supercooled liquids, how the structural developments correlate with the elasticity and shear transformation of metallic glasses and how the low-frequency vibrational normal modes originate from local structure. The "local structure" here includes not only short-range order, but also the arrangements and connection of coordination polyhedra in the medium or even longer range.

The organization of this thesis is as follows.

Chapter 1 is an introduction to several basic aspects of MGs, such as glass formation, their structure model and characterization as well as thermodynamic, kinetic, mechanical and vibrational properties of MGs. This sets the stage for detailed discussion of atomic-level structure and structure-property relationship in MGs in the following chapters.

In Chapter 2, we focus on the full icosahedra order dominated $Cu_{64}Zr_{36}$ model, and systematically analyze the role of Cu-centered full icosahedral short-range order (FISRO) and interpenetrating connection of icosahedra (ICOI) in determining several important properties, such as dynamical slowdown, reduction of internal energy and so on. Since only MGs composed of particular constituent elements and composition contain full icosahedral order, we also present MD simulation work to study two MG models without FISRO, $Pd_{82}Si_{18}$ and $Mg_{65}Cu_{25}Y_{10}$ in Chapter 3. Their characteristic SRO as Kasper polyhedra are revealed to be bi-capped square antiprisms (BSAP, in $Mg_{65}Cu_{25}Y_{10}$ MG) and tri-capped trigonal prisms (TTP, in $Mg_{65}Cu_{25}Y_{10}$ and $Pd_{82}Si_{18}$ MGs) rather than full icosahedra.

After the characterization of local structure among Cu-Zr, Mg-Cu-Y and Pd-Si models, the explicit correlation between atomic-level structure and properties will be discussed from Chapter 4 to Chapter 6. As revealed in Chapter 4, the temperature dependence of specific heat and liquid fragility between Cu-Zr and Mg-Cu-Y (also Pd-Si) are quite distinct. Thus we present MD simulation results to illustrate the underlying structural origin of those two important behaviors in supercooled liquids. Local structural ordering is found to relate to the evolution of specific heat and liquid relaxation during undercooling.

Chapter 5 details several aspects of mechanical behavior in MGs. Firstly elastic heterogeneity has been studied to correlate with local structure in Cu-Zr MGs. Specifically, we illustrate how the degree of elastic deformation correlates with the internal structure at the atomic level and how to quantitatively evaluate the local solidity/liquidity in MGs. In addition, the network of icosahedral order is revealed to form a stiff backbone and its percolation corresponds to the onset of slope change of shear modulus.

Also in Chapter 6, we have illustrated the structural signature of quasi-localized low-frequency vibrational normal modes, which may account for the intriguing anomalous vibrational properties in MGs. Specifically, the local atomic packing structure in a model MG strongly correlate with the corresponding participation fraction in quasi-localized soft modes, while the highest and lowest participation correspond to geometrically unfavored motifs (GUMs) and ISRO respectively. Besides, we also demonstrate that quasi-localized low-frequency vibrational modes correlate strongly with fertile sites for shear transformations in a MG.

Chapter 7 presents a summary of this thesis and proposed future work

I include as an appendix several papers which were published during my PhD study but which are not directly related to the frame of this thesis and hence not discussed in detail.

Chapter 2

Development of full icosahedra order in $Cu_{64}Zr_{36}$ supercooled liquids†

Starting from this chapter, we will make extensive use of molecular dynamics simulations to reveal the local order developed in liquids and amorphous alloys. In the present chapter we first monitor the development of icosahedral order, which is prevalent in a Cu-rich Cu-Zr ($Cu_{64}Zr_{34}$) liquid and metallic glass (1, 6). We illustrate that at this Cu-rich Cu-Zr alloy composition, Cu-centered full icosahedra constitute the dominant and characteristic short-range-order coordination motif. Our work below extends bonding

† Part of the results has been published in Refs. (6):
Ding, J et al. Acta Mater. 69: 343-354 Copyright 2014 Elsevier

previous findings in this liquid/glass, and addresses several questions regarding the ordering of Cu-centered coordination polyhedral towards full icosahedra (6), including i) their evolution and extent during prolonged structural relaxation, ii) the resulting reduction in potential energy and slowing-down of dynamics, iii) the accompanying preference of a particular type of Zr-centered Kapser coordination polyhedron, iv) the evolution and conversion of polyhedral connection schemes in the medium range. We also clarify five additional related issues (6), to i) differentiate full-icosahedra based ordering from the generally favorable five-fold bonds, ii) compare the Cu-based perspective with a Zr-centric view, iii) systematically list the rationales behind focusing on icosahedral order for explaining the $Cu_{64}Zr_{34}$ MG/liquid properties, iv) discuss other non-full-icosahedral ordering varieties, and v) comment on the most liquid-like local environments. Taken together, the issues addressed set the stage for understanding structure-property relations in a category of amorphous alloys that can be characterized based on full-icosahedral ordering.

2.1. Introduction to full icosahedra short-range order (FISRO)

As introduced in Chapter 1 (Section 1.2), the internal structure of metallic glasses needs to be understood on the atomic level (18-21, 50, 67, 74, 75, 79, 165-168). In particular, a meaningful description of the local order, in terms of characteristic short-to-medium range features (18-20, 74), is desirable. This, obviously, is a highly challenging proposition. In general, metallic bonds have minimal directionality, such that to lower energy there should be a tendency to surround any given (center) atom with as many

neighbors as possible. Regarding the efficient use of space, tetrahedral packing is advantageous because each atom in the tetrahedron is in contact with all the other three atoms. The polytetrahedral packing model (22) is therefore widely embraced. One sub-category of such packing, in the case of packing 12 atoms around a center atom (when the coordination number is twelve, CN=12), is icosahedral packing (22) (see Figure 2-1, gold spheres are for Cu atoms and grey are for Zr). This is an efficient way of maximizing tetrahedral atomic arrangements and triangulated shell faces: the 12 shell atoms form an icosahedron composed of 20 tetrahedra. The geometrically perfect/ideal icosahedron has a slightly smaller **A** atom at center, surrounded by shell atoms of the same kind (**B**), at an atomic size ratio (r_A/r_B) of 0.902 (74). Such an icosahedron is actually more centrosymmetric, and establishes more bonds, than the 13-atom fcc/hcp cluster. Icosahedra could be the favored local structure in amorphous metals, as originally postulated by Frank for monoatomic liquids (169).

Indeed, in recent years many experimental studies (for example, Refs. (19, 66, 67, 75, 79, 170-173)) using X-ray/neutron scattering and nanobeam electron diffraction, as well as numerous computer simulations employing *ab initio* or empirical interatomic interactions, e.g., Ref. (2, 5, 6, 61, 174-177), have identified local icosahedral order in metallic liquids and glasses. Of course, the icosahedra detected are not the prototypical ideal icosahedra mentioned earlier that have 20 identical and almost equilateral tetrahedra (edges formed between neighboring shell atoms are slightly longer). Instead, the icosahedra are distorted to various degrees; this is because in a real MG/liquid the center-to-shell atomic size ratio is not exactly 0.902, the average CN deviates slightly from 12, and the glass/liquid is often a concentrated alloy such that the shell is composed of both

A and B atoms of different sizes. In the recent publications (1, 2, 5, 6, 18, 174, 178-181), we have defined a category of CN=12 Cu-centered clusters as "full icosahedra". These Cu-centered full icosahedra (Cu-FI) have a Voronoi index of <0, 0, 12, 0> (see Figure 2-1). That is, the icosahedral motif is "complete" in the sense that the center Cu has all the 12 neighbors that enclose an icosahedron, and all the 12 bonds are five-fold bonds, even though the cluster is not unique but comprises of a range of quasi-equivalent configurations featuring the same CN and Voronoi index. This Cu-FI designation differentiates them from fragments of icosahedra, heavily distorted icosahedra-like polyhedra (e.g., those with Voronoi index <0, 2, 8, 2>, <0, 3, 6, 3> or even <0, 2, 8, 1>) as seen in Figure 2-1, or merely bond-pairs with a fivefold environment (see additional discussions in Section 2.4.1). While all of these varieties have been reported in the literature as evidence of icosahedral short-range order (ISRO), the full-icosahedra short-range ordering (FISRO) that we have singled out is arguably the tell-tale sign of ISRO and often the most property-controlling structural indicator (2, 4-6, 18, 174, 175).

There are however a number of unresolved issues regarding FISRO in metallic glasses and liquids (6). We will touch upon nine of such questions in this chapter. We will present the results of a systematic molecular dynamics (MD) simulation study looking into the FISRO development in a Cu-rich amorphous alloy, $Cu_{64}Zr_{34}$; at this alloy composition Cu-FI are known to be highly populous for Cu-centered coordination polyhedra (6, 178). Using this model liquid/glass, we address four questions regarding FISRO that have so far not been adequately explored. We first begin with a query into the extent of FISRO. Second, we intend to monitor the evolution of configurational potential energy (CPE) of the alloy along with the extensive structural evolution inside, to shed

light on the driving force for pronounced FISRO at this alloy composition. Third, as most of previous studies examined the Cu-Zr MG structure from the perspective of the dominant Cu-centered clusters, we probe the Zr-centered SRO in this liquid/glass. The fourth question to address is the development of extended icosahedra ordering with connection schemes of coordination polyhedra.

In the subsequent section, Section 2.4, we will address five additional issues. First, we will further clarify the definition of ISRO, in particular the FISRO based on Cu-FI, versus the presence/population of five-fold bonds. Second, after much discussion on Cu-centered motifs, one is naturally curious about a comparison with a characterization of the MG structure from the Zr-centric perspective (or by taking a global average of all atoms). Third, we will discuss the rationales behind focusing on Cu-FI as the characteristic SRO for the $Cu_{64}Zr_{34}$ MG/liquid, and the reasons for explaining MG/liquid properties from the FISRO standpoint. Fourth, we will briefly comment on the non-FISRO ordering types, e.g., the other preferable types of polytetrahedral clusters/motifs at other Cu-Zr compositions and in other amorphous alloy systems. The fifth and final question that we will discuss briefly is the coordination environments at the opposite-extreme, those that are the furthest away from FI. These are the least ordered local structures, or fragmented motifs, and low in population. But such local environments also deserve attention as they can be relevant or even controlling for certain important properties.

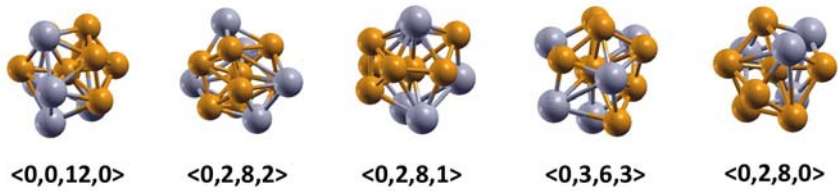

Figure 2-1. Schematic description (and Voronoi indices) of five most populous Cu-centered coordination polyhedra in $Cu_{64}Zr_{36}$ supercooled liquids/glasses.

2.2. Model systems

Here in this chapter we employ molecular dynamics (MD) simulations to study $Cu_{64}Zr_{36}$ model systems. They are simulated with optimized embedded atom method (EAM) potential, adapted from Ref. (174). Each sample contains 32,000 atoms, and the liquids of those samples were equilibrated for 10 ns at high temperature (2500K) to assure equilibrium and then quenched to room temperature (300 K) at cooling rates of 10^9 - 10^{12} K/s using a Nose-Hoover thermostat (the external pressure was barostated at zero) (58). The periodic boundary condition (PBC) is applied in all three directions. Another simulation procedure was to cool the liquid to 800 K at the cooling rate of 10^{12} K/s, then hold the supercooled liquid for structural relaxation (under *NPT* ensemble) at that temperature for 300 ns before quenching down to room temperature. The time step used in all simulations was 2 femtoseconds (shorter time step of 1 fs was applied to simulate the high temperature liquid). Smaller $Cu_{64}Zr_{36}$ samples with 10,000 atoms via Mendelev's Finnis-Sinclair EAM potential (176) were also quenched at 10^9 K/s and 10^{10}

K/s following the same procedure presented above. We monitor the local coordination in $Cu_{64}Zr_{36}$ liquids and MGs by conducting Voronoi analysis on their corresponding inherent structures, as discussed in Section 1.2.2.4.

2.3. The evolution of FISRO in $Cu_{64}Zr_{36}$ supercooled liquids

Using the model supercooled liquid of $Cu_{64}Zr_{36}$, we address four questions regarding FISRO that have so far not been adequately explored (6). We first begin with a query into the extent of FISRO. The constructed glass structure based on experimental data from laboratory MGs relied on the Reverse Monte Carlo (RMC) method (19). But the RMC samples the configurational space in a random manner, such that the final configuration reached is essentially the most random structure that can reproduce/fit the target experimental input within a given tolerance. As a result (172), the fraction of Cu in centers of FI is even less than that given by computer simulations conducted at very fast quench rates. The first pending question is therefore the potential extent/degree of FISRO. To monitor the (possibly significant) further development of FISRO, we will purposely prolong our MD simulations by cooling the liquid at a relatively fast quench rate (10^{12} K/s) and aging the supercooled liquid at 800 K for as long as >300 nanosecond. Second, we intend to monitor the evolution of configurational potential energy (CPE) of the alloy along with the extensive structural evolution inside, to shed light on the driving force for pronounced FISRO at this alloy composition. Third, previous studies examined the Cu-Zr MG structure from the perspective of the dominant Cu-centered clusters. It was believed that the behavior of the Zr environment is relatively featureless (18), with a rather broad

distribution of many cluster types each accounting for only a few percent of all the Zr atoms. With our prolonged simulation, we are now in the position to identify the preferential development of certain Zr-centered Frank-Kasper coordination polyhedra (182). The fourth question to address is the development of extended icosahedra ordering. As enormous Cu-FI clusters permeate the system with aging and/or slow cooling, we will get a better feel as to how the Cu-FI connect to one another, and how connection schemes in the medium range (second neighbors) evolve and convert to one another, as a function of decreasing temperature during supercooling, and over a range of cooling rates.

2.3.1. The extent of FISRO

Figure 2-2a plots the fractions of Cu atoms that center different coordination polyhedra, out of all the Cu atoms in the alloy, as a function of temperature during cooling of the $Cu_{64}Zr_{36}$ liquid at the slowest cooling rate (10^9 K/s) used in this study. We observe that the dominant CN is 12, and the FISRO development become evident in the supercooled liquid region. The trend is obvious that Cu-FI is the group that exhibits the most pronounced rise, relative to the other competing Cu-centered coordination polyhedra in Figure 2-2a. The fraction of Cu atoms centering FI reaches as high as 40% of all Cu atoms in the alloy; and since each FI involves 13 atoms (12 Cu and Zr atoms in the shell), these Cu-FI quasi-equivalent clusters involve as much as 90% of all the (Cu+Zr) atoms in the system. To make sure that our finding is not artifact of a particular interatomic potential, we also monitored the fraction of Cu-FI in a $Cu_{64}Zr_{36}$ liquid/MG obtained using the Mendelev potential (176). A data point is included in Figure 2-2a for comparison as solid star (red) for the fraction of Cu-centered icosahedra in $Cu_{64}Zr_{36}$

glasses obtained with the cooling rate of 10^9 K/s using Mendelev's potential (176). While the latter potential produces a slightly lower fraction of icosahedra, a very similar trend is observed. The structure factors of simulated $Cu_{64}Zr_{36}$ glasses are displayed in Figure 2-2c, in comparison with X-ray diffraction data for $Cu_{64.5}Zr_{35.5}$ glass in experiment (176).

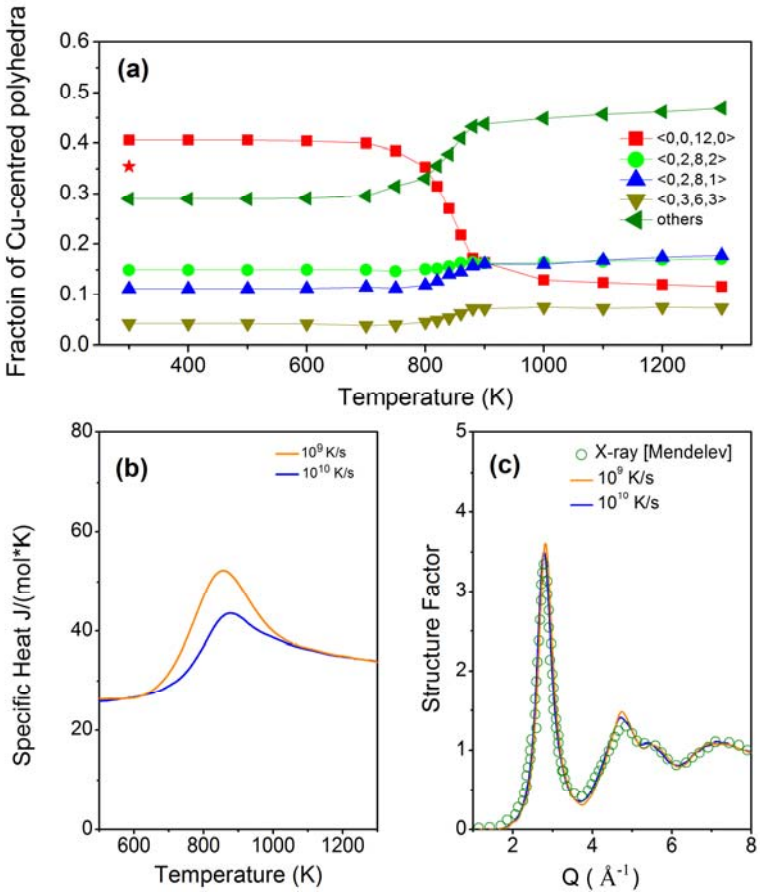

Figure 2-2. (a) Temperature dependence of the fractions of Cu-centered coordination polyhedra (6). (b) Temperature dependence of specific heat for $Cu_{64}Zr_{36}$ with the cooling rate of 10^9 K/s and 10^{10} K/s from supercooled liquids to glassy states (6). (c) Structure factor of simulated $Cu_{64}Zr_{36}$ glasses (6) with comparison with X-ray diffraction of $Cu_{64.5}Zr_{35.5}$ glass in experiment (176).

Similar structural evolution towards extensive FISRO is also observed upon aging the $Cu_{64}Zr_{36}$ supercooled liquid at 800 K. The relaxation time at this temperature was extended to 300 ns, which is exceedingly long when compared with all previous MD simulations (the typical quench rate used before was $>10^{10}$ K/s, with a total simulation time of no more than a few ns, over the temperature range in the supercooled liquid region), before cooling down to room temperature. As seen in Figure 2-2a, among all the Cu-centered coordination polyhedra, the only type that experienced persistent and pronounced increase in population is the Cu-FI. Similar to the continuous cooling case, the fraction of Cu atoms centering FI rise to 41% of all Cu atoms in the alloy, far exceeding that previously reported for this alloy (18). FISRO based on Cu-FI is clearly the dominant local motifs in $Cu_{64}Zr_{36}$ supercooled liquid and MG.

2.3.2. The role of FISRO in reducing energy and dynamical slowdown

Having confirmed the progressive development of FISRO in "slowly cooled" or "aged" $Cu_{64}Zr_{36}$, the second point to ascertain is that FISRO indeed brings down the system energy. This point is made in Figure 2-2b and Figure 2-3b. Indeed, the steep rise in Cu-FI during undercooling in Figure 2-2a apparently coincides with the fast increase of specific heat (the derivative of system energy with respect to temperature) with cooling in Figure 2-2b, which was also revealed in our earlier studies (1, 3). Since Cu is the majority species, the system energy reduction during structural evolution is expected to go hand in hand with the decreasing CPE of the Cu atoms. In Figure 2-3b for the aging experiment at 800 K, the pronounced increase of Cu-FI observed in Figure 2-3a also

correlates very well with a continuously decreasing CPE of the alloy. These results suggest that it is the pronounced reduction in CPE due to the topological and chemical ordering associated with the formation of Cu-FI that drives the preferential conversion of other viable local environments towards FISRO (see Figure 2-3).

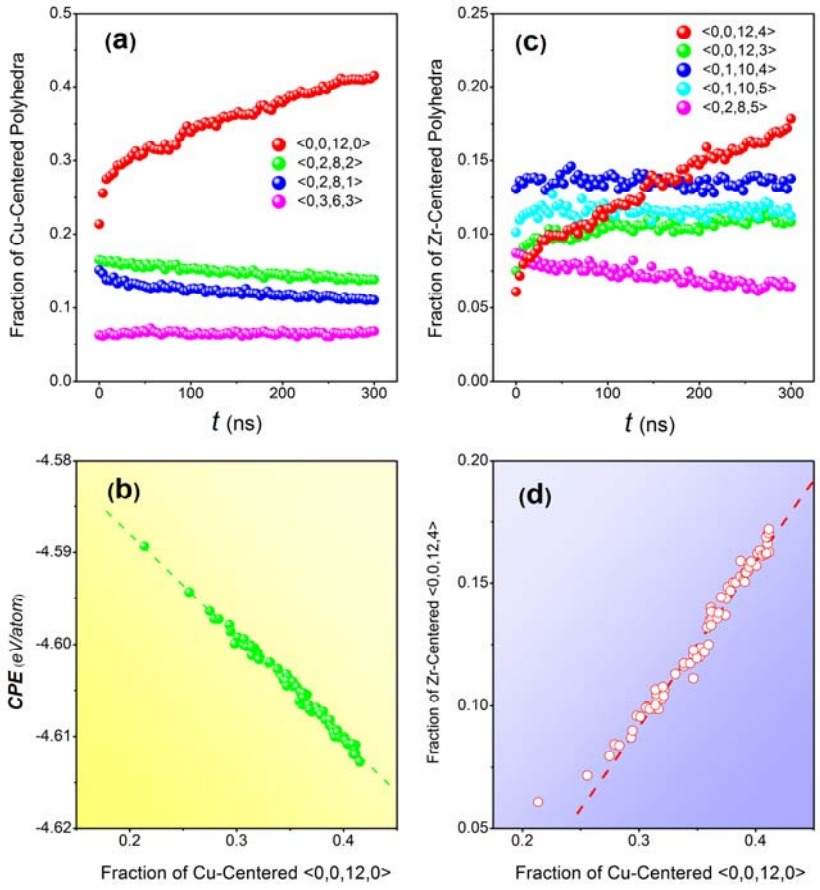

Figure 2-3. Structural relaxation of $Cu_{64}Zr_{36}$ supercooled liquids at 800 K (6). (a) Fractions of Cu-centered coordination polyhedral with relaxation time; (b) Correlation between the fraction of Cu-FI and CPE of the alloy; (c) Fractions of Zr-centered coordination polyhedral with relaxation time; (d) Correlation between the fractions of Cu-centered <0,0,12,0> and Zr centered <0,0,12,4>.

To further establish the critical role of FISRO, we add that the pronounced development of Cu-FI in supercooled $Cu_{64}Zr_{36}$ liquid also has the consequence of slowing down the dynamics of the cooling liquid (6). Indeed, as shown in Figure 2-4, the average bond lifetime, τ_{delay}, which measures the delay time for the breakage of an atomic bond (as defined in Ref (183)) for $Cu_{64}Zr_{36}$ supercooled liquids under structural relaxation at 800 K, is observed to increase by orders of magnitude due to the increased fraction of Cu-FI. Figure 2-5 plots the spatial distribution of bond lifetime for all atoms in a slice of $Cu_{64}Zr_{36}$ supercooled liquid (with 35% Cu-FI) at 800 K. The slice has a layer thickness of ~2.5 Angstrom (roughly equal to average atomic spacing). The colors in the plot denote the bond lifetime in logarithmic scale, see corresponding sidebar for τ_{delay}, in $\log_{10} \tau_{delay}$ (picosecond). The open circles are for Cu atoms at the centers of full icosahedra. There is clearly a strong correlation between the two: regions with slow dynamics are statistically more enriched in Cu-FI (correspondingly, the bond life time inversely scales with the fraction/population of non-icosahedral Cu-centered polyhedra). This is another indicator of the important role of FISRO in contributing to the overall properties of the alloy, i.e., clear evidence of structural relaxation (viscosity) correlating with local atomic arrangements.

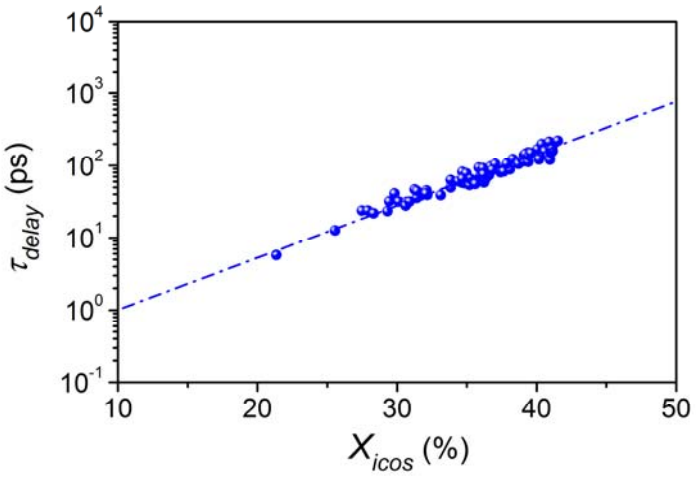

Figure 2-4. Relationship between the fraction of Cu-centered icosahedra (X_{icos}) and average bond lifetime in $Cu_{64}Zr_{36}$ supercooled liquid under structural relaxation at 800 K (6).

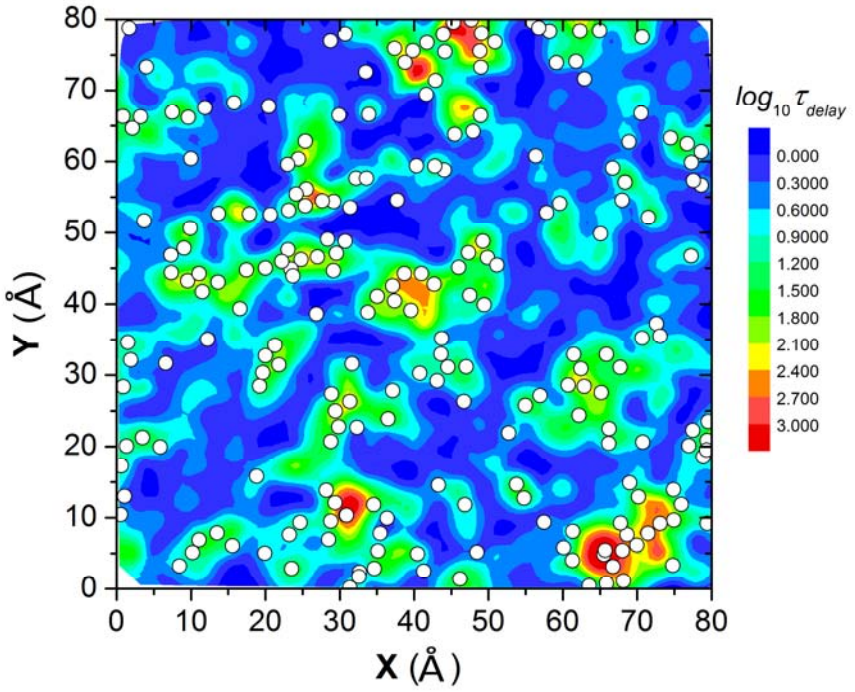

Figure 2-5. Spatial distribution of bond lifetime for all atoms in a slice of $Cu_{64}Zr_{36}$ supercooled liquid at 800 K (6).

2.3.3. Zr-centered Z16 Kasper coordination polyhedra

The extensive MD aging we used afforded us the opportunity to resolve a third question, namely, the preferential development of a specific type of coordination polyhedra around Zr. In Figure 2-3c, we see that the preferred CN moves towards 16 around Zr. The motif favorable for CN=16 has been predicted to be the <0, 0, 12, 4> polyhedra (Z16 cluster), which is the configuration with the lowest disclination content (18). But instead <0, 1, 10, 4> and <0, 1, 10, 5> were observed in earlier studies to be relatively more populous in $Cu_{64}Zr_{36}$, and the Zr atoms centering these coordination polyhedra only amount to 10-13% of all the Zr atoms (18). As shown in Figure 2-3c, this dilemma is now resolved: given sufficiently long relaxation, the <0, 0, 12, 4> Kasper polyhedra indeed take over to become the most populous, reaching a fraction of 17% of all Zr-centered polyhedra. As expected, the evolution towards favorable Kasper polyhedra holds for both of the two species in the alloy: the rise of Z16 polyhedra goes hand in hand with the escalating population of Cu-FI, as shown in the almost linear correlation (upon sufficient relaxation) between the two, Figure 2-3d. Together they reduce the density of extrinsic disclinations (18) for more regular polytetrahedral packing.

2.3.4. Evolution of polyhedra connections in the medium range

We now monitor the extended ordering, in term of the connection schemes that link the short-range-ordered polyhedra together. Here two basic types, which are simultaneously present in the alloy, are analyzed. The first type is a Cu-centered full

icosahedron overlapping with another Cu-centered full icosahedron; this scenario is termed "interpenetrating connection of icosahedra" (ICOI) (184, 185). Inset is a schematic showing a segment of interpenetrating connection of icosahedra (ICOI, grey atoms are Zr and yellow ones are Cu). Here the latter Cu atom, while being the center of another full icosahedron, is a nearest neighbor of the former Cu. Such a connection joins FI together, to build networks of FI that eventually constitutes the backbone of the glass (see Section 5.3). The second type is more general, concerning the connection schemes that link any two Cu-centered coordination polyhedra (3, 174), where the two center atoms are second nearest neighbor (see schematic description in Figure 2-7a). A consideration of these two connection types thus reveal certain aspects of correlations over the medium range, i.e., beyond nearest-neighbor atoms and extending to first-neighbor and second-neighbor polyhedral motifs.

For the first type, we present in Figure 2-6 the fraction of interpenetrating icosahedra out of all the surrounding Cu, on average for each Cu full icosahedron (left y axis, orange symbols). As expected, the former increases fast with increasing fraction of Cu-FI. Apparently, the measured fraction of interpenetrating icosahedra is much higher than that expected from a random distribution of Cu-FI (see the orange solid line). This indicates that the Cu-FI tend to aggregate, at least in the short-to-medium range, as building blocks of the amorphous structure (19). This role of ICOI will be discussed further in Section 5.3. Meanwhile, the separated Cu-FIs without interpenetrating connection (right y axis in Figure 2-6) become fewer and fewer with increasing fraction of Cu-FI.

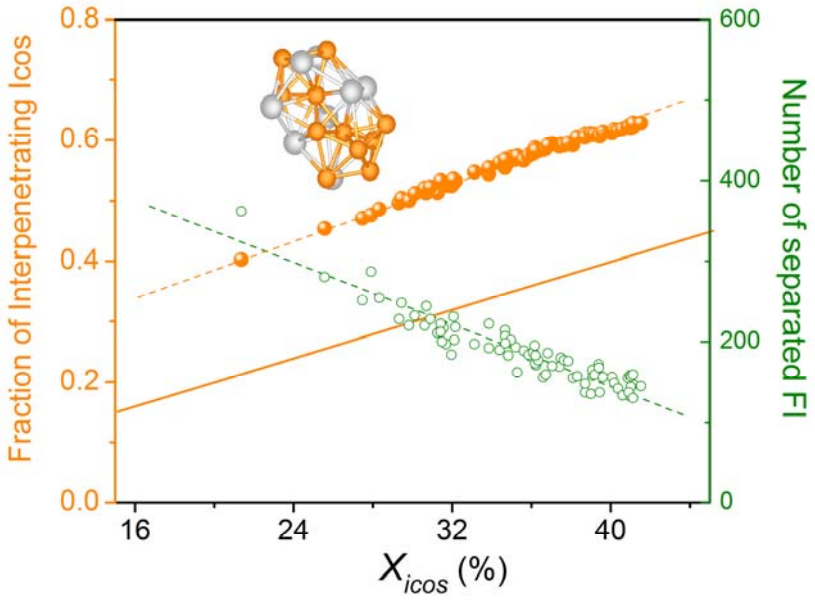

Figure 2-6. The rising fraction of interpenetrating connection of icosahedra per Cu-centered full icosahedron scales with the fraction of Cu-centered icosahedra (6). Correspondingly, the number of separated Cu-centered icosahedra decreases with increasing X_{icos}.

For the second type, the connection schemes examined here cover a wide range, including vertex sharing (VS), edge sharing (ES) and face sharing (FS). In these three cases, the two neighboring atomic clusters share 1, 2 and 3 atoms, respectively, as shown schematically in the insets in Figure 2-7a. For the two atoms at centers, they are second nearest neighbor in all these schemes (see schematics in Figure 2-7a). In Figure 2-7a, the evolution of coordination polyhedra connections is plotted as a function of temperature, during cooling from the liquid state to the glassy state. Three different cooling rates, 10^9 K/s, 10^{10} K/s and 10^{12} K/s, are compared. The corresponding curves, from the fastest to

the slowest cooling rate in the direction of the arrow, are displayed together. The degree of ES and FS evolves with increasing supercooling in the liquid (3): FS increases while ES decreases. Also, slower cooling rate, in other words more structural relaxation, leads to more pronounced growth of FS and reduction of ES. The steep rise of FS in the supercooled liquid region, as T approaches T_g, is analogous to the behavior of FISRO reported in Figure 2-2a. The total number of connections to other motifs (between centered atoms as second nearest neighbor) does not change significantly, because the increase of FS connections appears to be accompanied by the reduction of ES connections. In sum, structural relaxation during supercooling leads to the growth of the more favorable FS connection, at the expense of ES. In contrast, the average number of VS connection per atom experiences little change from 1500 K to 300 K, perhaps because VS exerts little additional atomic stresses due to the longer distance between the centers of the two connecting clusters.

The same trend, i.e., the increasing FS versus decreasing ES during supercooling, is observed for both Cu-FI and non-icosahedral Cu-centered polyhedra (Cu-non-FI). But the difference is that the average number of FS connections to a Cu-FI is greater than that around a Cu-non-FI, by as much as ~4. This is shown in Figure 2-7b, in the eventual glass formed by cooling from the liquid state at different rates. It demonstrates that compared with all other Cu-centered polyhedra types, Cu-FI are better connected (with clusters each centered by a second-neighbor Cu in this case) by transforming more ES to FS, again lending support to the role of FISRO in forming more stable/slow regions (see Section 2.3.2).

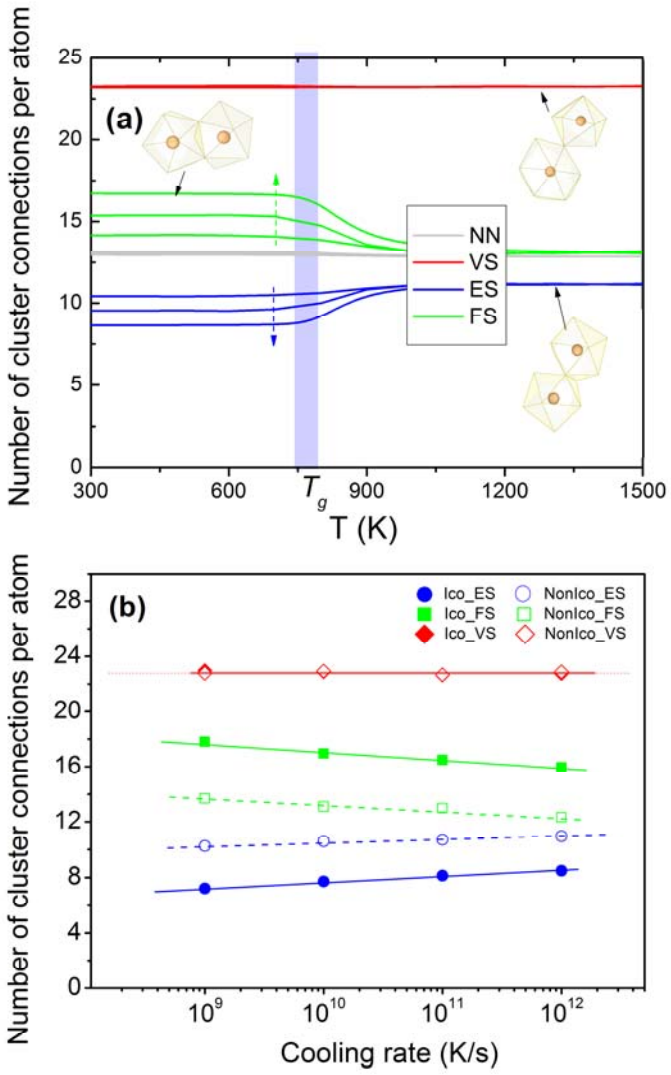

Figure 2-7. (a) The evolution of average number of nearest neighbors (NN) and coordination polyhedra connected via various schemes in $Cu_{64}Zr_{36}$ supercooled from the liquid state to the glass state. Arrows indicate that from the fastest to slowest cooling rate. (b) The average number of connected clusters for Cu-centered icosahedra and non-icosahderal coordination polyhedra in $Cu_{64}Zr_{36}$ metallic glasses obtained at various cooling rates. (6)

2.4. Five additional issues regarding FISRO in metallic glasses/liquids

In the subsequent section, Section 2.4, we will address five additional issues. These questions naturally emerge from the storyline presented in Section 2.1. First, we will further clarify the definition of ISRO, in particular the FISRO based on Cu-FI, versus the presence/population of five-fold bonds. We emphasize that FISRO dominates only in a limited number of alloys (at certain MG compositions), while five-fold bonds and triangulated shell faces are always preferred. Second, after much discussion on Cu-centered motifs, one is naturally curious about a comparison with a characterization of the MG structure from a Zr-centric perspective (or by taking a global average of all atoms). Third, we will discuss the rationales behind focusing on Cu-FI as the characteristic SRO for the $Cu_{64}Zr_{34}$ MG/liquid, and the reasons for explaining MG/liquid properties from the FISRO standpoint. Fourth, we will briefly comment on the non-FISRO ordering types, e.g., the other preferable types of polytetrahedral clusters/motifs at other Cu-Zr compositions and in other amorphous alloy systems. The fifth and final question that we will discuss briefly is the coordination environments at the opposite-extreme, those that are the furthest away from FI. These are the least ordered local structures, or fragmented motifs, and low in population. But such local environments also deserve attention as they can be relevant or even controlling for certain important properties.

2.4.1. FISRO vs. fivefold bonds

As mentioned in the introductory section, the literature may have generated the impression that the most general feature in metallic glasses and liquids is ISRO. But the definition of the ISRO claimed by different authors is not the same, and this is often where confusions arise. Some authors used the term ‘‘icosahedral order” in a more loosely defined way, compared with our FISRO. For example, the preponderance of “five-fold bonds”, based on the number of 555 pairs from common neighbor analysis (CNA) or of 1551 pairs (Honeycutt–Andersen index (186)), has been taken as evidence of icosahedral order (79, 187). However, it should be clarified that almost all the preferred clusters in any MGs/liquids would have high fractions of fivefold bonds (and thus high fractions of 555 or 1551 pairs). This can been seen directly from the Voronoi indices of the Frank-Kasper clusters (the Z clusters (18, 182)), which are the preferable motifs at different CNs in various MGs/liquids. Different from fcc/hcp, for which the Voronoi index is <0, 12, 0, 0>, here the third number in the Voronoi indices indicating the number of pentagon faces is appreciably larger than the other face types. For example, for <0, 3, 6, 0> for CN=9, <0, 2, 8, 0> for CN=10, all the way to <0, 0, 12, 4> for CN=16, the five-edged faces are always the most populous. The *n*-edged polygon between the bonding atoms is usually associated with *n* common neighbors surrounding the pair, and such a configuration would constitute an “*n*-fold bond” local environment reflected by the CNA index. In other words, five-fold bonds are significant across the board, including for Zr in $Cu_{64}Zr_{36}$ (CN=16) and for Cu in Zr-rich Cu-Zr MGs (CN=10), and even in trigonal-prism type metal-metalloid glasses (CN=9). Obviously, in these amorphous alloys none of the characteristic motifs is actually an icosahedron. Also, in previous

reports on dense random packing of hard spheres or monatomic metallic liquids, the fivefold bonds were found populous, and other bond orientational order parameters (82) also suggest high icosahedral order, but the fraction of <0, 0, 12, 0> full icosahedra is not high, as the majority of the fivefold bonds are in the fragmented icosahedra or icosahedral-like polyhedra. Therefore, on the level of packing motifs in terms of quasi-equivalent <0, 0, 12, 0>, the FISRO dominates only in some amorphous alloys at certain compositions (here Cu-rich Cu–Zr). However, the polytetrahedral packing principles, encouraging five-fold bonds and triangulated shell faces, are generally applicable to all MGs and liquids (18). The polytetrahedral packing includes FISRO (and other types of ISRO people report), but the full icosahedral order *per se* should not be considered universal.

For $Cu_{64}Zr_{36}$, the preponderance of <0, 0, 12, 0> Cu-FI can also be appreciated from the standpoint of an appropriate effective atomic size ratio (174). For Cu surrounded by Cu only, the atomic size ratio is 1, and for Cu surrounded by Zr only, the atomic size ratio is ~0.82. In either case, the size ratio is not close to 0.902. In an Cu-Zr alloy, Cu is surrounded by both Cu and Zr, and at a certain alloy composition the Cu:Zr ratio is such that the effective size ratio is close to 0.902, for the center atom relative to the average of 12 (Cu+Zr) neighbors. This appears to be the situation near $Cu_{64}Zr_{36}$.

2.4.2. Can the structure be dissected from a different perspective?

For the MG/liquid alloy, can the structure be analyzed from the perspective of an average atom? First off, we note that MG-forming liquids and MGs contain as least two

constituent elements. In other words, different from monatomic systems, now we have two intrinsically different local environments that follow the packing principles underlying the structure formation. In $Cu_{64}Zr_{36}$, the average CN around Cu is about 11.8, while that around the larger Zr is about 15.3 (increasing towards 16 upon relaxation). The advantage and importance of viewing the structure from the perspective of each species is that Cu and Zr centered clusters have very different center to shell atomic size ratio, and thus very different CN and local topological order. The information about the respective local environment is contained in the Cu-centered and Zr-centered partial pair-distribution functions (PDFs).

If one instead elects to view the structure from the standpoint of an average atom (total PDF), the average CN would be ~13. That may result in the misleading conclusion that the local packing is dictated by CN=13 polyhedra and that icosahedra and Z16 Kasper clusters would not be important (or do not even exist).

One can of course take a Zr-centric view; from the minority Zr standpoint the popular structural motif has been found to be the Z16 cluster, <0, 0, 12, 4>, as revealed in our prolonged simulation in Section 2.3.3. For Zr, CN is approaching 16 (and 13, for an average atom in the system). The CN is obviously away from the 12 needed for the FI to be the dominant topology. As such, FISRO featuring Cu-FI is prevalent only for Cu-centered local packing, not for Zr surroundings or for the global average. Also note that at Zr-rich Cu-Zr compositions, even for the Cu local environment FI would not be the most populous polyhedra either, as the average CN around Cu shifts to 10~11. The advantage of singling out Cu-FI is that one can make the point that there is a preferential and in fact dominant FISRO scheme around Cu in Cu-rich Cu-Zr alloys, and this

particular FISRO is special in that it has consequences on the stability, rigidity, dynamics and rheological properties (next in Section 2.3.2).

2.4.3. Why do we prefer to characterize the $Cu_{64}Zr_{36}$ structure as FISRO dominated?

We now discuss further the rationales behind choosing Cu-FI as the characteristic SRO. First of all, Cu is the majority constituent element in the $Cu_{64}Zr_{36}$ alloy. On can also argue that icosahedra with the five-fold rotational symmetry are incompatible with the long-range translational crystal order. This "dilemma" leads to a barrier for the transition from the icosahedral packing in the amorphous state to the long-range ordered crystal (79), thus stabilizing the glass against crystallization. Our main reason, however, is the mounting evidence we have contributed, which indicates that this particular FISRO based on Cu environments is highly effective in accounting for the properties of the Cu-Zr MGs/liquids (18).

The results presented in Section 5.3 later indicate that Cu-FI help build the backbone of the $Cu_{64}Zr_{36}$ structure. We see that Cu-FI reach about 40% (compared with 17% for Zr <0,0,12,4> motifs), and all the atoms involved in these FI account for as much as ~90% of the total Cu+Zr atoms. Cu-FI are therefore indeed predominant. We showed that Cu-FI brings down CPE, see Figure 2-2b and 2-3b in Section 2.3.2, as it involves less free volume and atomic stresses (5), and has a uniform CN and 5-fold bonds only. Their interconnections evolve with undercooling, in favor of FS, more so than non-icosahedral motifs.

In addition, our previous studies (18) have revealed that that Cu prefers more unlike neighbors due to the negative heat of mixing, i.e., chemical SRO. In elastic deformation, we have shown that Cu-FI offer the highest resistance (lower elastic strain, higher anisotropy index), more than any other type of motifs including those centered around Zr, and thus representing the regions with higher solidity (lower liquidity) (2, 4) (see detailed discussion in Chapter 5). The correlation with the propensity for non-affine shear transformations is also noteworthy (179, 188): the sample that exhibits more localized plastic deformation correlate statistically with those that contain more Cu-FI. Moreover, atoms associated with Cu-FI show lower mobility in the supercooled liquid (181). In the liquid, the rise of Cu-FI population coincides with the rising relaxation time, thus controlling the dynamical slowdown with supercooling (1, 3). This is supported by the scaling between bond breaking delay time and the Cu-FI fraction, see Figure 2-4. Tracking the behavior of Cu thus adequately reflects the response of the system.

2.4.4. What happens at alloy compositions where Cu-FI is not dominant?

As already emphasized above in Section 2.4.1, although ISRO has been claimed in many of the published papers on MG/liquid structures, and while five-fold bonds are indeed ubiquitous and populous, the FISRO dominates only in a limited number of alloys (at certain MG compositions). Even for other compositions in the Cu-Zr system, such as those on the Zr-rich side, FI are not the most populous motifs (18, 181). Other characteristic local motifs are better suited for describing the amorphous structure, as demonstrated before in many other amorphous alloy systems, including Al-based MGs (solute-centered quasi-equivalent clusters) (73), Mg-based MGs (3) and metal-metalloid

MGs (1, 5, 19, 162), where the characteristic coordination polyhedra are prism-like (such as tri-capped trigonal prisms, bi-capped square anti-prism, etc.).

As outlined in a recent review (18), at various CNs and compositions, there are still featured Kasper polyhedra which we call Z-clusters. Each type in this variety of polytetrahedral packing schemes still represents a particular preferred (albeit quasi-equivalent) motif, for a given atomic size ratio. It is yet to be determined if any Z-cluster can be as dominant and as energy-favorable as Cu-FI in the alloy discussed in this Chapter. The roles of these Z-clusters in controlling properties also requrie systematic study.

2.4.5. Should one care about the cluster types that are the furthest away from FI?

The answer is yes, even though such local structures are of low population in the as-prepared amorphous metals (179). These are the least ordered local structures and the most "liquid like" (21, 112), in the spectrum of the inherently inhomogeneous glass structure. There are many occasions when one should pay attention to the "fragmented" local environments, at the opposite-extreme from FI. This is because such local environments can be relevant or even controlling for certain important properties. For example, they are expected to be the most fertile sites where shear transformations would tend to take place, when the amorphous alloy is exposed to applied stresses (179, 188). Therefore, for improving plastic flow, an adequate fraction of the liquid-like sites (179), rather than focusing on the solid-like backbone, is more desirable. They are obviously of interest, if the objective is to identify the local structures most prone to change, or most likely to respond to external stimuli (such as stresses or temperature). However, a

detailed discussion of these high-liquidity (4, 112) local regions is beyond the scope of this Chapter, and will be the focal point of our next step on fertility index and structure-relaxation relations.

Finally, we point out a misconception that can sometimes be misleading in the community. While in our discussions (and in the literature) the amorphous structure is dissected and described in terms of clusters and motifs, one should not perceive the structure as a composite of "clusters and empty space". Instead, different from oxide/silicate glasses (189-193) or polymer glasses (194, 195), amorphous metals are atomic glasses. Each atom is the center of its own coordination polyhedron. The non-directional metallic bonding entails space-filling, leading to a continuous spectrum of generally high local packing densities (and usually high CNs), without bifurcation into connected (or even separated) cluster units (or molecules) plus "holes".

2.5. Conclusions

Although icosahedral order in metallic liquids/glasses has been studied by many researchers since Frank's first proposition in 1952 (169), it is still a topic under ongoing debate. The answers to many important questions are still vague or (seemingly) inconsistent. This is partly due to the intrinsic complexity of the problem (there are many different metallic-glass forming systems involving virtually all common metals at a variety of compositions), and partly due to the lack of consensus on what can be called "icosahedral order" (although the ideal icosahedron is unambiguously defined, the real icosahedra in a liquid/glass are always distorted to some extent, leaving ambiguities in setting the "tolerance" for the distortion before the local environment is designated to be

a different polyhedron). This is often the root of the inconsistencies and misconceptions found in recent literature.

In this chapter, we have clarified several issues related to the definition and description of icosahedral order in metallic liquids/glasses, particularly the full icosahedra we recently employed to characterize the structure and structure-property relations in certain Cu-Zr amorphous systems (6). The connections and differences between the ideal icosahedra, full icosahedra, icosahedra-like clusters (as often used in literature), distorted icosahedra, and five-fold bonds (as obtained from the CNA or the HA-index) are discussed. Further, the icosahedral order is understood in a more general context, which is the polytetrahedral packing featured by the Frank-Kasper polyhedra (Z-clusters) – a full icosahedron can be classified as the Z12 cluster (CN=12) with complete five-fold bonds and no disclination (i.e., highest rotational symmetry), whereas other Z-clusters with larger or smaller CNs (corresponding to greater atomic size mismatch) contain the maximum possible number of five-fold bonds and minimum inevitable/intrinsic disclinations for the given CN (18). In general, the SRO in metallic liquids/glasses is polytetrahedral in nature, and which Z-clusters are favored depends on the relative atomic size of the constituent elements, as well as their chemical SRO. FISRO is dominant only when the appropriate atomic size ratio is reached, such as in $Cu_{64}Zr_{36}$.

Full icosahedra do play an important and distinctive role, at least in Cu-rich Cu-Zr alloys, as recently reported in literature and further highlighted in the current work (6). By conducting more systematic simulations, we have revealed additional details regarding the evolution of FISRO with extended relaxation, the conversion of sharing

schemes between neighboring icosahedral clusters, the formation of spatial connection and percolation over longer length-scale, and their impact on various properties such as configurational potential energy, specific heat, bond lifetime. Analysis is also conducted from the Zr-centric view, based on which we rationalize why Cu-centered full icosahedral ordering in this alloy is the tell-tale indicator we should focus on – not just because it is dominant in terms of population, but more for how it can be directly and effectively connected with the response and behavior of the alloy system. It is the latter fundamental structure-property correlation that is what we have long been pursuing for amorphous materials.

Chapter 3

Local structure of $Mg_{65}Cu_{25}Y_{10}$ and $Pd_{82}Si_{18}$ MGs: MG models without dominant FISRO†

In Chapter 2, we have extensively studied the full icosahedral short-range order (FISRO, with Voronoi index <0, 0, 12, 0>) in $Cu_{64}Zr_{36}$ metallic glass and supercooled liquid. As discussed in Section 2.5.1, there are specific reasons why FISRO is dominant in that alloy. However, most MGs are not inclined to form full icosahedra short-range order, even though five-fold bonds are still dominant, e.g. Al-based MGs (solute-centered

† Part of the results has been published in Refs. (1, 3, 5):
Ding, J et al. Phys. Rev. B 85(6) Copyright 2012, American Physical Society
Ding, J et al. Acta Mater. 61(8) Copyright 2013, Elsevier
Cheng, YQ et al. Mater. Res. Lett. 1(1) Copyright 2013, Taylor&Francis

quasi-equivalent clusters) (73), Mg-based MGs (3, 196-198) and metal-metalloid MGs (1, 5, 19, 162, 199, 200). Among those MG models without dominant FISRO, we select two typical model systems, $Mg_{65}Cu_{25}Y_{10}$ and $Pd_{82}Si_{18}$ (1, 3, 5), then investigate their local structure and properties via classical and *ab initio* molecular dynamics simulations in this chapter.

3.1. Local structure of $Mg_{65}Cu_{25}Y_{10}$ metallic glasses and supercooled liquids

In the entire BMG family discovered so far, Mg-based BMGs (197, 198, 201-207) constitute an important group. One intriguing aspect is that their behavior often puts them near one end of the whole BMG spectrum. As a first example, Mg-BMG forming alloys often possess an outstanding glass-forming ability (GFA), among the highest of all the BMG formers; the critical thickness for BMG formation is usually on the order of centimeters (for the normally used Cu-mold casting process) (208). Even for the base ternary Mg-Cu-Y system, from which many Mg-based BMGs are built, fully glassy rods of 9 mm in diameter can be easily obtained (207).

Second, the thermodynamic and kinetic properties of BMG-forming Mg alloys are intriguing. In terms of the fragility of the supercooled liquids, Mg alloys are one of the strongest among all the BMG-forming liquids (see for example the viscosity data reported for $Mg_{65}Cu_{25}Y_{10}$ (85-87)). This relatively strong liquid behavior, comparable to that of some great BMG-formers such as the multicomponent Zr-Ti-Cu-Ni-Be liquid (209), is likely to be a major contributor to the high GFA mentioned above. Meanwhile,

the supercooled $Mg_{65}Cu_{25}Y_{10}$ liquid exhibits a shallow heat capacity curve that is even less temperature-dependent than Vitroloy 1 and Vitroloy 4 (85-87).

Third, Mg-based BMGs are generally brittle, arguably the most brittle group among all BMGs, often shattering before or at yielding during compression tests (204). For $Mg_{65}Cu_{25}Y_{10}$, its Poisson's ratio was measured to be in the range of 0.302 to 0.329 (99, 105), near the low end of all BMGs. Such a low Poisson's ratio has been postulated to indicate a low fracture toughness for BMGs (210).

Fourth, the characteristic atomic-level structures remain to be clarified, despite several studies that looked into the atomic packing and local order, using reverse Monte Carlo simulations to fit the experimental data ($Mg_{60}Cu_{30}Y_{10}$ (211), $Mg_{61}Cu_{28}Gd_{11}$ (212)), *ab initio* simulations using a 140-atom supercell ($Mg_{65}Cu_{25}Y_{10}$ (196)), and molecular dynamics (MD) simulations employing empirical potential for the base binary alloy (Mg-Cu, (213)). Due to the atomic size ratios and potential electronic charge transfer involved in such systems (214), the atomic packing and characteristic local motifs are likely to be quite different from some of the BMGs that have received more systematic studies, such as those in the transition-metal based Zr-Cu (1, 18) and Zr-Cu-Al system (174).

Among all these aspects that are not well understood, the atomic structure and nature of bonding is presumably the key issue, which may provide explanations for the macroscopic properties. Therefore, we have carried out in this section a detailed analysis to systematically uncover the short-to-medium range atomic packing as well as the electronic structure, selecting $Mg_{65}Cu_{25}Y_{10}$ as the representative of the Mg-TM-Ln (TM=transition metal, Ln=lanthanide metal or Y) systems. This characterization of the glass structure from the electronic to atomic level is made possible by using a

combination of *ab initio* and empirical-potential MD simulations. We have identified their signature structural features. Specifically, different from some BMGs for which full icosahedra short-range order (FISRO) is a dominant and property-controlling structural feature, we will show that for amorphous $Mg_{65}Cu_{25}Y_{10}$ the leading polytetrahedral packing scheme is in the form of Cu-centered tri-capped trigonal prisms (TTP, Voronoi index <0,3,6,0>) and bi-capped square antiprisms (BSAP, Voronoi index <0,2,8,0>). This finding is interesting, as previously the TTP and BSAP packing varieties were mostly found in metalloid-containing systems that possess certain degree of covalent bonding (19, 162, 200). Also reported are bond shortening and charge transfer, indicating ionic bonding character, as well as their role in promoting the particular atomic packing motifs.

3.1.1. EAM empirical potential

Our simulations employed both the classical MD simulations via empirical potentials, and the *ab initio* MD (AIMD) based on density functional theory (3). The classical MD allows us to work on relatively large samples and long timescales (nanosecond to microsecond), although the development of empirical embedded atom method (EAM) potentials was time consuming. The optimized EAM potential was developed by H.W Sheng (unpublished). AIMD offers high accuracy as well as information about the electronic structure, but suffers from limitations to small length scale (hundreds of atoms) and timescale (picosecond to nanosecond). In our work, the EAM-MD is utilized to investigate the short-to-medium range order, and the electron charge distribution is the focus of the AIMD calculations.

3.1.2. Model systems

In the EAM-MD simulations (3), a 10.4 nm×10.4 nm× 10.4 nm sample of $Mg_{65}Cu_{25}Y_{10}$ with 54,000 atoms was equilibrated at 1500 K for 2 ns and then quenched to 300 K at the cooling rate of 10^{10} K/s by applying Nose-Hoover thermostat (58). The glass transition temperature T_g is estimated to be ~485 K (3), which is higher than the experimentally measured 418 K (105) and 425 K (105); this can be reasonably attributed to the much faster cooling rate in MD simulation. A typical atomic configuration of amorphous $Mg_{65}Cu_{25}Y_{10}$ obtained as such is shown in Figure 3-1. Periodic boundary conditions were applied and the external pressure was maintained around zero during the entire process of cooling. In addition to the MG sample, the supercooled liquids of $Mg_{65}Cu_{25}Y_{10}$ (between 570 K and 770 K, close to the liquidus temperature (204, 205)) were also studied (3). The liquid configurations were relaxed for about 0.1 μs to 0.2 μs in MD simulation at the designated temperatures to reach the quasi-equilibrium states (on simulation timescales).

Geometrical analysis on the atomic configurations, i.e. the Voronoi tessellation method (18) (as discussed in Section 1.2.2.4), yields information about the atomic packing, such as the pair distribution functions (PDFs), atomic coordination numbers (CNs), and types of short-range order (SRO) in terms of the coordination polyhedra. Certain Voronoi polyhedra stand out as characteristic configurations and such "quasi-equivalent clusters" are used to represent the favorable local motifs (18). As illustrated later in Section 3.1.3, the Cu atoms among $Mg_{65}Cu_{25}Y_{10}$ metallic glasses/liquids apparently tend towards two short-range local environments, the TTP with Voronoi index

<0, 3, 6, 0> and the BSAP with Voronoi index <0, 2, 8, 0>. Example atomic configurations of TTP and BSAP packing around Cu are illustrated in Figure 3-1. The grey balls are for Mg atoms, gold ones for Cu and green ones for Y atoms. As for medium-range order, its degree of development scales with that of SRO, but is more difficult to identify and quantify. In our analysis we have monitored the sharing schemes of the SRO clusters. Common neighbor analysis (CNA) (187) (see Section 1.2.2.3) was also used to provide extra information regarding the connectivity of the bonds among common neighbors of a particular pair, which is useful particularly for revealing local atomic arrangements characteristic in the fragments of standard polyhedra (18).

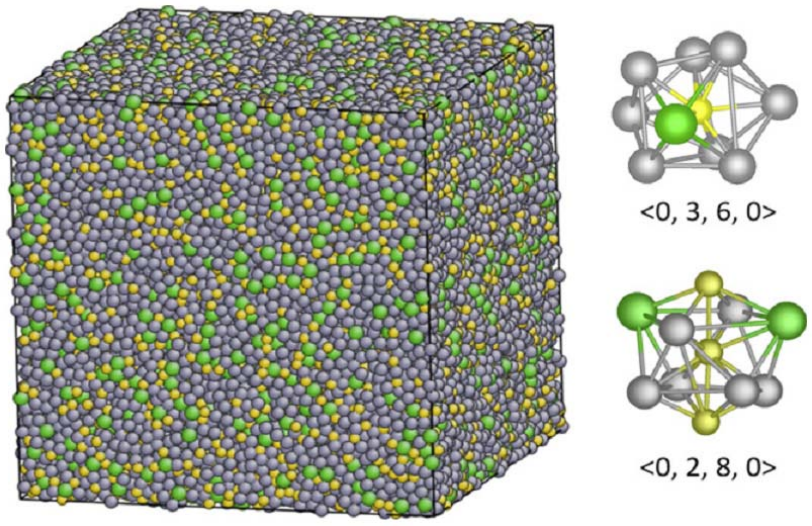

Figure 3-1. Atomic configuration for a 54,000-atom $Mg_{65}Cu_{25}Y_{10}$ MG. (3)

For the liquid and supercooled liquid at high temperatures, the local configurations fluctuate. In the MD simulations, we probed the inherent structure employing the steepest decent algorithm, to identify the energetically-preferred configurations if fluctuations are

removed. This reveals that certain clusters have an "energetic advantage" over the others in the inherent structure, although they would not be static and stay unchanged, but instead break up and reform elsewhere (different types of clusters maintain certain fractions at equilibrium).

The other sample of $Mg_{65}Cu_{25}Y_{10}$ MG was obtained via *ab initio* simulation based on density functional theory (DFT). Applying the Vienna ab intio simulation package (VASP) (215), a configuration containing 400 atoms was generated in a cubic box with periodic boundary conditions. It was equilibrated at 1500 K and then quenched to 300 K at the cooling rate of 6×10^{13} K/s under the NVT ensemble. Projector-augmented-wave (PAW) potentials (216, 217) were employed with the generalized-gradient approximation (GGA) to the exchange-correlation potential. The simulation was performed on the Γ point only. The density at 300K was adjusted to correspond to zero pressure, and the dimension of finally obtained supercell was 2.03 nm×2.03 nm× 2.03 nm. The density of the EAM MD-derived $Mg_{65}Cu_{25}Y_{10}$ MG was consistent with that derived from the AIMD.(3)

3.1.3. Atomic packing structure

PDFs of EAM-MD-derived $Mg_{65}Cu_{25}Y_{10}$ MG at 300K are shown in Figure 3-2a. The partial PDFs indicate strong correlations for Mg-Cu and Cu-Y, which show stronger and sharper peaks than the other pairs. For the Y-Y pair, the second peak is relatively strong, almost exceeding the first one, suggesting the tendency of self-avoidance, i.e., Y prefers not to interact with other Y atoms in the nearest-neighbor shell. In Figure 3-2b,

the Y-Y partial PDF of the liquid state (1500 K) is compared with that of the glassy state (300 K), obtained with EAM-MD at different cooling rates (10^{10} K/s and 6×10^{13} K/s) and obtained with AIMD. In the liquid state the first Y-Y peak is higher than the second peak, which remains so in the glasses obtained at fast cooling rates (AIMD and EAM-MD). However, when the cooling rate was slowed down by 3-4 orders of magnitude, structural ordering develops to much obvious levels to result in the avoidance between nearest Y atoms. This trend indicates that the Y-Y avoidance is expected to be even stronger in laboratory-made $Mg_{65}Cu_{25}Y_{10}$ MG, for which the applied cooling rate is much slower.

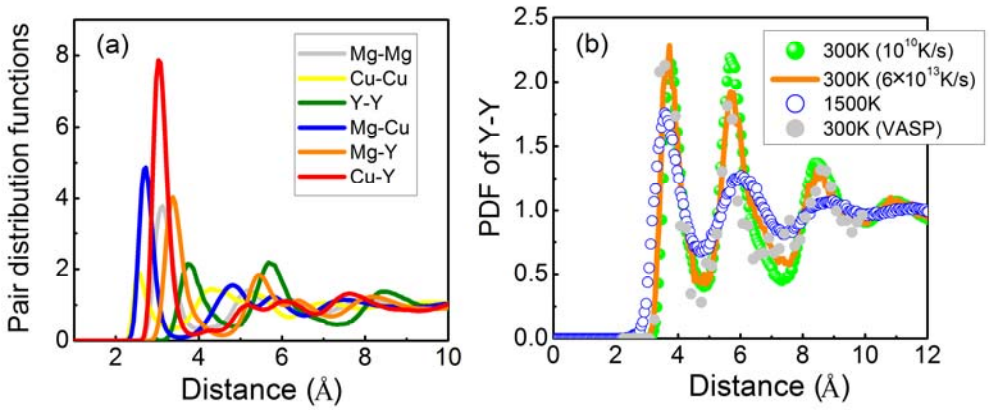

Figure 3-2. (a) Partial PDFs of $Mg_{65}Cu_{25}Y_{10}$ MG at 300 K derived from EAM-MD. (b) Partial PDF of the Y-Y pair for liquid state (1500 K) and two glassy states at 300 K from EAM-MD, in comparison with that from AIMD-quench to 300 K. (3)

The Voronoi tessellation analysis was used to monitor the SRO motifs for $Mg_{65}Cu_{25}Y_{10}$, from the supercooled liquid at 770 K to the MG at 300 K. As shown in Figure 3-3a, the Cu atoms apparently tend towards TTP and BSAP. The fraction of Cu

atoms in the center of TTP polyhedra, out of the total number of Cu atoms, is ~22.7% at 770 K and ~28% at 300 K, whereas the fraction of Cu-centered BSAP evolves from 18.4% at 770 K to 24.3% at 300 K. In other words, over half of the total Cu atoms center these prism-type motifs. As each prism involves 9 to 10 atoms (mostly Mg, plus Y and Cu) in the shell surrounding the center atom, the total number of atoms involved in these prisms account for ~85% of the total number of all atoms in the system. In addition, 10% to 15% of Cu-centered Voronoi polyhedra are of the <0, 3, 6, 1> and <0, 2, 8, 1> types, both of which can be regarded as distorted BSAP (162). As such, the TTP and BSAP Kasper polyhedra are obviously the primary local motifs, i.e., characteristic SRO clusters. Similar topological structures have been observed before, e.g., for the Si atoms in $Pd_{82}Si_{18}$ and P atoms in $Ni_{80}P_{20}$ or $Pd_{40}Ni_{40}P_{20}$ (19, 162, 200), typical for solute-centered clusters in metal-metalloid systems.

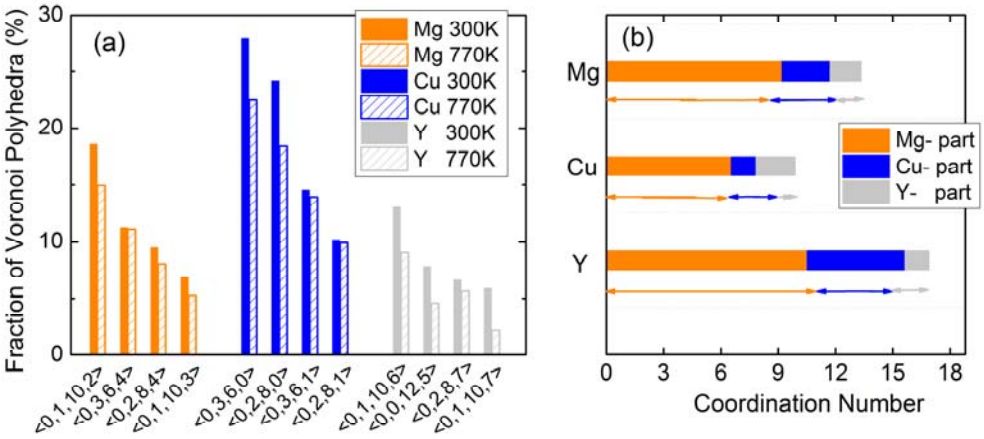

Figure 3-3. (a) Fraction of Voronoi polyhedra centered around Mg, Cu, Y atoms in both EAM MD-derived (770 K and 300 K) and AIMD-derived (300 K) $Mg_{65}Cu_{25}Y_{10}$ MG configuration. (b) Coordination number around Mg, Cu and Y atoms at 300 K. (3)

The coordination polyhedra around the other two species, Mg and Y, have also been included in Figure 3-3a. The four most populous Mg-centered Voronoi polyhedra are <0, 1, 10, 2>, <0, 3, 6, 4>, <0, 2, 8,4> and <0,1, 10,3>, and for Y-centered polyhedra they are <0, 1, 10, 6>, <0, 0, 12, 5>,<0, 2, 8, 7>, and <0, 1, 10, 7>. Among these polyhedra, <0, 1, 10, 2> and <0, 0, 12, 5> are Kasper polyhedra for CN= 13, 17, respectively, while the others are distorted ones (18). Full icosahedra (FI), with Voronoi index<0, 0, 12, 0>, have been extensively studied in Zr-Cu MG model in Chapter 2 and other MG systems (18), and believed to be a key structural feature that influences the thermodynamics, kinetics, elasticity and plasticity, which have been extensively discussed in Section.2 . Here, in the $Mg_{65}Cu_{25}Y_{10}$ MG, FI are not easily formed around all the three species: only about 7% Mg-centered clusters are arranged in this topology. One obvious reason is the atomic size ratio involved. In $Mg_{65}Cu_{25}Y_{10}$, the atomic radius for Mg, Cu and Y atoms are 0.160 nm, 0.127 nm and 0.180 nm, respectively (74). The atomic size ratios are thus r_{Cu}/r_{Mg}=0.79 and r_{Cu}/r_{Y}=0.71. The effective size ratio, assuming Cu is surrounded by Mg, Cu and Y in proportions that scale with the alloy composition (no chemical preference of certain species), is about 0.83. Correspondingly, the preferred CN around Cu is between 10 and 11 according to the efficient packing model (74), far below the 12 needed for FI (see discussion in Section 2.5.1). As seen in Figure 3-3a, the actual CN for Cu is 9.9. The further reduction (from the expected CN) can be attributed to the chemical ordering and bond shortening, which will be explained next.

In addition to topology, we also found preferential bonding between certain species, also known as chemical short-range order (CSRO). If all the atoms are randomly and uniformed mixed without any preferential bonding, the partial CN for each species around a center atom will be the same as the overall composition: 65%, 25% and 10%. The partial CNs based on these proportions for ideal mixture are shown in Figure 3-3b using bars with arrowed ends, in comparison with the actual partial CNs found around Mg, Cu and Y atoms. We observe that around each Cu with a total CN=9.9, on average there are 1.3 Cu (rather than the expected 2.5) and 2.05 Y (expected 0.99). Also, around each Y atom there are 5.1 Cu (expected 4.2) and 1.25 Y (expected 1.7). It can thus be concluded that Cu atoms are inclined to bond with Y atoms (and of course also Mg atoms) in the first-neighbor shell, rather than with other Cu. Similarly, Y tends to bond with Cu, instead of other Y atoms. The underlying reason for CSRO, in terms of the electronegativity difference or charge transfer, will be discussed later.

Figure 3-4 plots the fraction of TTPs and BSAPs as a function of temperature within the supercooled liquid regime. These SROs developed around Cu atoms increase only moderately and gradually with decreasing temperature. This contrasts with the steep rise in icosahedral ordering in the supercooled liquid region, known previously for Cu-Zr, as presented in Chapter 2 (1, 6) (this temperature dependence is presented in Section 4.3.2 for comparison).

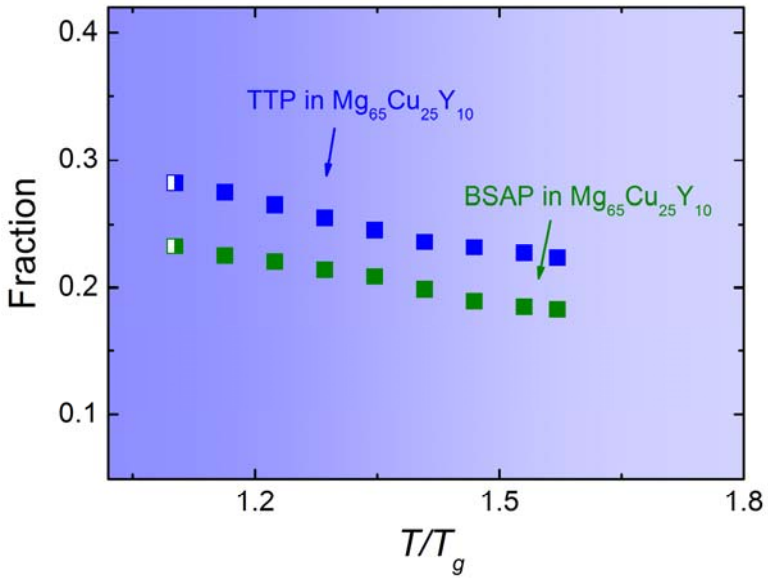

Figure 3-4. Fraction of Cu-centered TTPs and BSAPs as a function of temperature of the $Mg_{65}Cu_{25}Y_{10}$ supercooled liquid. (3)

Common neighbor analysis (CNA) (187) is another way to provide details regarding the polytetrahedral packing. The CNA results for all the pairs in the EAM-MD-derived $Mg_{65}Cu_{25}Y_{10}$ MG at room temperature are shown in Table 3-1. A significant number of five-fold bonds are found, indicated by their 555 CNA index (plus distorted variations with indices of 544 and 433 (79, 162)): the fraction is as high as ~76% out of the total number of pairs. Interestingly, there are also a quite large number of pairs with indices that are found in crystal-like environments. For example, 39% of Cu-Cu pairs have the 444 index, and 38% of Y-Y and 19% of Mg-Y are 666 pairs. The indices of 444 and 666 are typical for bonded pairs in a bcc structure. In addition, 8% of Mg-Mg pairs are 422, which is indicative of hcp order. Therefore, although there are few full coordination polyhedra that are crystal like, e.g., Voronoi polyhedra <0,12,0,0> for fcc

and hcp, <0,6,0,8> for bcc, many fragments exist that contain pairs with local surroundings resembling those in crystals.

Table 3-1. Fraction of CNA pairs in EAM MD-derived $Mg_{65}Cu_{25}Y_{10}$ MG at 300 K. (3)

Local environment		Total	Mg-Mg	Cu-Cu	Y-Y	Mg-Cu	Mg-Y	Cu-Y
	# of bonds	692808	323175	17503	6776	88056	56838	27652
Pentagonal bipyramid-like*	555	34%	32%	8%	24%	38%	30%	41%
	544	22%	26%	…	27%	10%	33%	17%
	433	20%	17%	34%	3%	31%	8%	23%
BCC-like	444	4%	3%	39%	...	5%	…	3%
	666	7%	7%	...	38%	...	19%	5%
HCP-like	422	6%	8%	...	...	6%	4%	5%

* As discussed in Section 2.4.1, a high fraction of such five-fold bonds is sometimes used to imply that there is considerable icosahedral SRO. This is indeed true, if the dominant CN is close to 12. However, five-fold bonds are also populous in other types of polytetrahedral clusters. Therefore, in systems where the CN is not close to 12, a high fraction of five-fold bonds does not mean that the local order is predominantly icosahedral. (3)

The PDFs in Figure 3-2, for example that of the AIMD quenched sample, give information regarding the bond lengths for each pair. The first peak corresponding to the Mg-Cu bond is at 2.68 Å, and that for the Cu-Y pair is at 2.94 Å (similar results were found before for a $Mg_{60}Cu_{30}Y_{10}$ MG (211)). Compared with the sum of their tabulated metallic radii, there is a noticeable "bond shortening" by 6.6% for the Cu-Mg bond, and 4.2% for the Cu-Y bond. Here bond shortening is measured by a comparison of the actual bond length between two atoms with the calculated/predicted interatomic distance based on tabulated atomic radii for the corresponding metallic elements. For "atomic glasses" and metallic bonding, the "average" bond length is not expected to be very different from the calculated/predicted value. The obvious "bond shortening" refers to the observation that the average bond length found in the glass is significantly shorter than the calculated/predicted interatomic distance from the tabulated metallic radii. This origin can be attributed to the effect of covalency or iconicity, which will be discussed below. For a Cu-centered cluster, from the standpoint of the central Cu, the Mg and Y neighbors appear closer and "larger" due to the bond shortening (174). As the larger atoms are favored in the nearest neighbors (the atomic size sequence, in decreasing order, is Y, Mg and then Cu), it is not surprising that the CN of Cu moves to below 10, which favors the TTP and BASP Kapser polyhedra from the efficient packing perspective (74).

For the structural features beyond the short-range order, we have also studied how the coordination polyhedra connect to one another, as similar approaches presented in Section 2.3.4. The common connection schemes (6, 174) are shown in Figure 3-5: vertex sharing (VS), edge sharing (ES) and face sharing (FS). Figure 3-5 plots the evolution with temperature of the number of clusters connected in a particular scheme, given as an

average for all the Cu-centered TTPs and BSAPs. The plot shows that the cluster connections via the face-sharing scheme increases with undercooling at the expense of the edge-sharing variety, while VS undergoes less change over this temperature range. This medium-range structural evolution can be simply explained from the topological viewpoint that the more stable construction (FS) gradually replaces edge-shared clusters, as the latter scheme represents looser packing and possesses an additional degree of freedom to rotate along the shared edge.

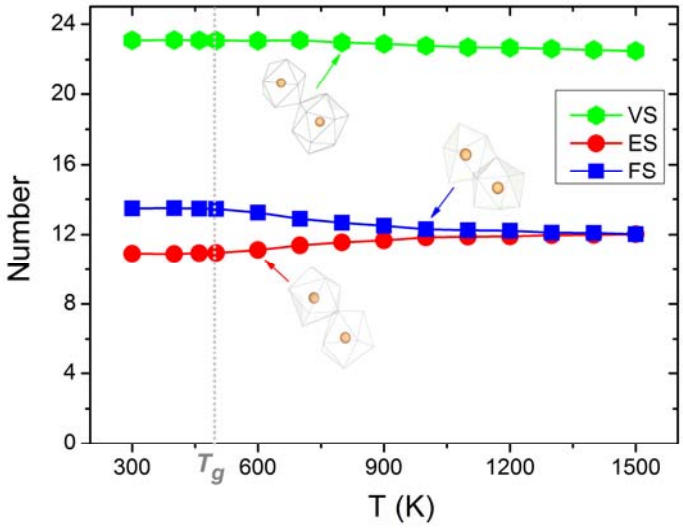

Figure 3-5. The average number of connected motifs, via vertex sharing (VS), edge sharing (ES) and face sharing (FS) schemes (see schematics insets), as a function of temperature. (3)

3.1.4. Electronic structure of $Mg_{65}Cu_{25}Y_{10}$ metallic glasses

We now switch to the discussion of the bonding nature in the amorphous $Mg_{65}Cu_{25}Y_{10}$, at the electronic level. For MGs, the electronic basis of their properties has

been explored before by several groups. For example, the valence electron concentration per atom, *e/a*, is believed to influence the GFA (218). A nearly-free-electron model (219) postulates that the maximum stability or high GFA would be achieved at the composition for which the Fermi level lies at a minimum of the electronic density of states (DOS) (220). Also, Gu *et al*. (221) attempted to improve the ductility of the Fe-based BMGs by replacing elements that create ionic and covalent bonds with other elements that favor metallic bonds. Widom *et al*. (214) studied the Ca-based MGs via *ab initio* simulations and correlated their ionicity (charge transfer) with Poisson's ratio.

Looking at the bonding in $Mg_{65}Cu_{25}Y_{10}$ MG on the basis of electronic structure, the bonds are of course mainly metallic. This is expected from the fact that Mg, Cu and Y are all metallic elements. Metallic bonding arises from the electrostatic attractive forces between the delocalized electrons gathered in an electron cloud and the positively charged metal ions (222). Ideally, conduction electrons in metallic bonds are totally non-localized as in the simplistic model of free electrons. However, in reality, metallic bonding rarely behaves as in the idealized model, but instead contains covalent and/or ionic characters to certain degree. The primary signature of covalent bonding is the sharing and localization of valence electrons between the bonding atoms, while that of ionic bonding is the charge transfer and the resulting Coulombic electrostatic force between the positively and negatively charged ions. We now examine the covalency (electron localization) and ionicity (charge transfer) in $Mg_{65}Cu_{25}Y_{10}$ MG, before linking them to the atomic structure discussed above and the properties of this MG.

First, let us consider the degree of covalency in the $Mg_{65}Cu_{25}Y_{10}$ MG. In a recent study, the shortening and covalent-like characters of the Al-Cu bond were observed in

$Zr_{47}Cu_{46}Al_7$ MG (174). To answer the question if Mg-Cu and Cu-Y have similar degree of covalency, we have calculated the electron localization function (ELF) (223, 224) that characterizes the degree of localization and the relative bond strength. $ELF = \frac{1}{1+(D_\sigma / D_\sigma^0)^2}$, where D_σ is a measure of Pauli repulsion and scales with the probability density of finding another same-spin electron near the reference electron. The smaller this probability, the stronger the Pauli repulsion and the more localized is the latter electron (224). D_σ^0, which is used to normalize D_σ, is the D_σ value in a homogeneous electron gas having the same local spin-density. ELF=0.5 thus represents the same level of Pauli repulsion as in the homogeneous electron gas, and a higher ELF value indicates that the electrons are more localized (ELF=1 can be interpreted as perfect localization). We used VASP calculations to quantify the ELF values on a 64×64×64 grid in the cubic box. To obtain the ELF profile from one atom to a neighboring atom, we first connect them with a tube (radius =0.36 Å), which is evenly divided into 21 sections. ELF data points included in each section are then averaged, and the 21 averaged ELF values profile the bond between the two atoms (225).

In Figure 3-6, we present the ELF profile obtained along the Mg-Cu bond in $Mg_{65}Cu_{25}Y_{10}$ MG, to compare with that of the Al-Cu bond in $Zr_{47}Cu_{46}Al_7$ MG. The peak region in the middle can be regarded as the bonding area (225). That the ELF values, especially those close to the center of the two bonding atoms, are below 0.5 may be attributed to the low density of valence electron close to the inner shell. For Al-Cu, there is clearly an indication of electron localization, as ELF approaches 0.6. But for Mg-Cu, the localization is not obvious, or at least much weaker. This observation is not surprising,

because Al is located at the boundary between metals and semiconductors in the periodic table (with Mg on the left and Si on the right), and its electronic structure is known to have certain degree of directionality and covalency (226), between that of Mg and Si.

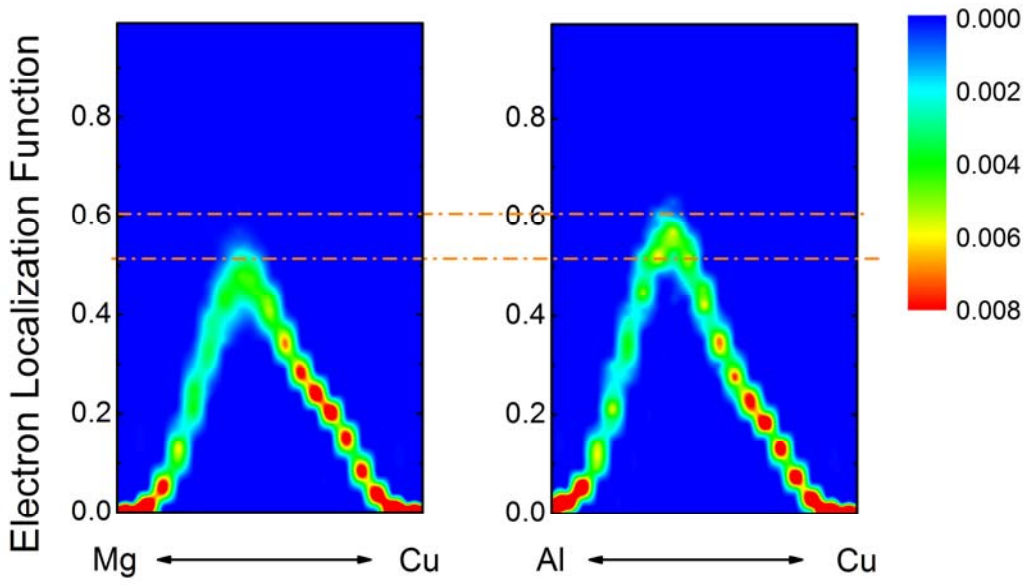

Figure 3-6. ELF contour for Mg-Cu (left panel) bonds in AIMD-derived $Mg_{65}Cu_{25}Y_{10}$ MG, in comparison with (right panel) that for the Al-Cu bond in the $Zr_{47}Cu_{46}Al_7$ MG. (3)

Since Mg-Cu bonds cannot be characterized as partly covalent-like, we next examine the degree of ionicity. We have performed the Bader analysis (227, 228) on the VASP output of the charge distribution in 400-atom $Mg_{65}Cu_{25}Y_{10}$ MG supercell on a 200×200×200 grid. Figure 3-7 shows a charge density distribution map on a cut-plane 1.5 Å from the front. The Bader analysis is based purely on the electronic charge density by locating the zero flux surfaces that divide atoms (227, 228) (a zero flux surface is a 2-D surface on which the charge density is a minimum perpendicular to the surface). The

charge enclosed within the Bader volume can be treated as the total electronic charge of an atom (228). Its difference from the valence electron of an isolated atom is taken as the transferred charge. The inset in Figure 3-7 displays a representative Cu-centered BSAP as an example, as well as the Bader volume of the center Cu atom (the volume enclosed inside the orange meshes).

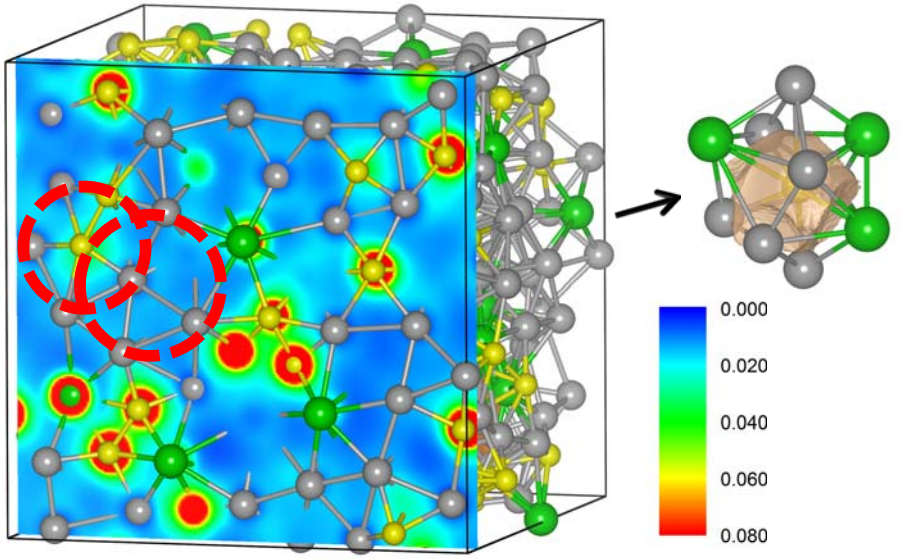

Figure 3-7. Atomic configuration in AIMD-derived $Mg_{65}Cu_{25}Y_{10}$ MG. A cross-sectional plane shows the charge density distribution. (3)

The results of the Bader analysis are shown in Figure 3-8, where positive Bader charges are the number of electrons transferred out. There are noticeable fluctuations; for some of Mg atoms the values are even negative. This is mainly caused by the wide scatter of the short-range configurations around each center Mg atom. On average, every Mg atom gives away ~0.71 electrons and each Y atom donates ~1.1 electrons. On the contrary, every Cu atom receives about 2.2 electrons. Accounting for the overall

composition, the average charge transfer is about 1.1 electron/atom in $Mg_{65}Cu_{25}Y_{10}$ MG at 300K. Although this is not comparable to typical covalent/ionic materials, such as silica glass or amorphous Al_2O_3 where the charge transfer can be expected to be 2.67 to 2.4 electrons/atom, the value of 1.1 electron/atom is on the high side of the charge transfer known to exist in all the metallic alloys (229).

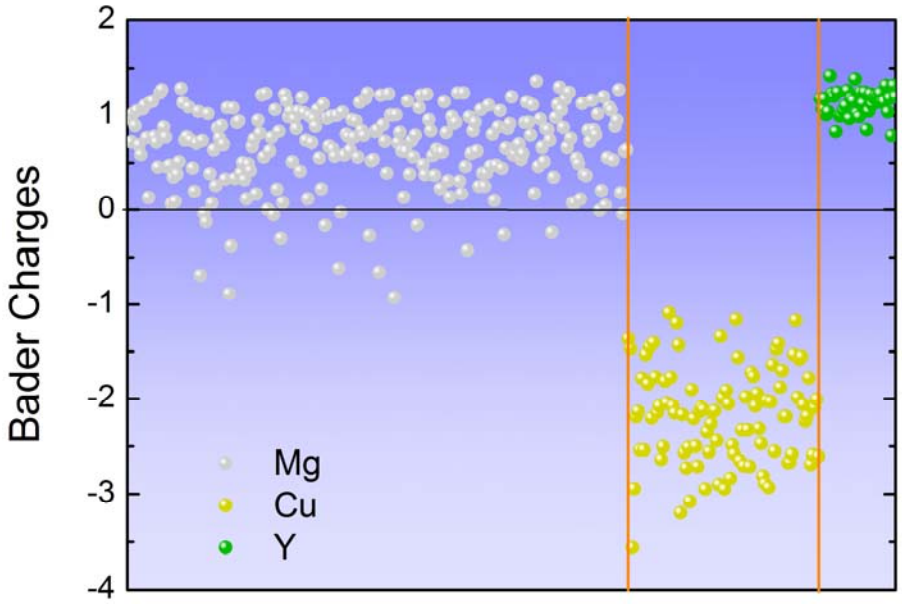

Figure 3-8. Distribution of Bader charges for the 400-atom sample of the AIMD-derived $Mg_{65}Cu_{25}Y_{10}$ MG. A positive value means giving out electrons and vice versa. (3)

As the charge transfer is obvious between Cu and the surrounding (Mg, Y) atoms, the Cu-centered motifs benefit from the enhanced binding due to contributions from the additional ionicity, on top of the negative heat of mixing known for Cu-Mg (or Y) (230). This further justifies our focus on Cu-centered clusters as the most stable and key motifs in this MG. Note that the charge transfer and the bond shortening not only indicate strong

affinity between Cu and neighboring species, but also affect the effective atomic size ratio, both of which favor the TTP and BSAP packing. In other words, the enhanced bonding strength, as well as the preference for efficient packing for the effective atomic size ratio resulting from the actual bond length, stabilizes the particular prism-type motifs (building blocks). While the TTPs and BSAPs in this system are not centered by metalloid solutes as in the TTPs and BSAPs in metal-metalloid systems, the reasons for the emergence of prism-type local order are similar. To reiterate, the chemical affinity between Mg and Cu (and Y) drives the preference for unlike neighbors around Cu, playing the role of covalent-like bonding character around the metalloid atoms. Meanwhile, the bond length changes adjust the effective size ratio towards that in metal-metalloid systems. As a result, like the metal-metalloid case, both the efficient packing based on the atomic size ratio and the chemical bonding determine the formation of the characteristic coordination polyhedra in the Mg-based metallic glass.

It is well known that ionicity strongly correlates with the electronegativity of elements. For the electronegativity on the Pauling scale (231), Mg is 1.31, Cu 1.90 and Y 1.22, where a higher value reflects a stronger tendency of an atom to attract electrons towards itself. This sequence of electronegativity is consistent with the average charge transfer we found for each element, where Cu atoms accept electrons while Y and Mg give out electrons (more from Y than Mg). To recapitulate, similar to the Al-Cu bonds in $Zr_{47}Cu_{46}Al_7$ MG, Mg-Cu and Cu-Y pairs also exhibit significant bond shortening. But different from the Al-Cu bonds with noticeable covalent characters (as measured by the electron localization), the Mg-Cu and Cu-Y bonds appear to have high ionic characters (as measured by the charge transfer). The additional contribution from ionicity (charge

transfer) makes the Cu-centered TTPs and BSAPs even stronger and stiffer, and favors unlike neighbors in the first shell. Similar trends may be expected with simple arguments from the known magnitude of the enthalpy of mixing between species pairs (230), but the electronic structure analysis presented here yields quantitative results on a species-by-species basis and provides more insight into the origin of the attraction between different atoms on the electronic level.

3.2. Local structure of $Pd_{82}Si_{18}$ metallic glasses and supercooled liquids

3.2.1. EAM potential and model systems

To simulate structural changes of metal-metalloid liquids, we developed interatomic potentials for the Pd-Si binary system based on *ab initio* calculations (1, 5). To this end, the embedded-atom-method (EAM) formalism was adopted to represent the empirical interatomic potential, to facilitate large-scale molecular dynamics simulations (see Ref. (1) for details). The as-developed EAM potential for Pd-Si has been validated against a large array of experimental data. The potential is found to be adequate to describe both Pd and Si single elements, such as defects, equations-of-state, elastic constants and mechanical properties. More relevant to the alloys studied in this paper is that the Pd-Si EAM potential is sufficient to describe the energetics of various intermetallic phases formed between Pd and Si. Therefore, atomistic simulation employing the as-developed EAM potential for Pd-Si is believed to be able to shed light on the formation physics of the Pd-Si metallic glass. The Pd-Si EAM potentials can be accessed at: https://sites.google.com/a/gmu.edu/eam-potential-database/Home/PdSi.

To access atomistic details, we use MD simulations of Pd-Si supercooled liquids and metallic glasses (1). It is based on EAM potentials fitted to the Pd-Si system that features solute-solute avoidance and solute-centered trigonal prisms as the local SRO in the amorphous model, typical of metal-metalloid systems (near the 80-20 composition, specifically $Pd_{82}Si_{18}$). While these computer liquid models are expected to have similar local structural motifs when compared with real-world liquids, they are subject to very different spatiotemporal and sample preparation conditions. For the model, a series of 10,000-atom liquid configurations from 2000 K to 300 K (at the interval of 20 K) was obtained via *NPT* quenching (at zero pressure) from the equilibrium melt (2000 K) at the rate of 10^{10} K/s (1). At each temperature in the supercooled regime, the configuration was relaxed for 10 ns ~ 100 ns until the total energy leveled off. The relaxed configurations were run under *NPT* at zero pressure for another 10 ns to produce 200 samples at each temperature, from which an average is obtained for the properties to be evaluated.

3.2.2. Atomic-level structure of $Pd_{82}Si_{18}$ models

$Pd_{82}Si_{18}$ is representative of metal-metalloid systems with solute-lean compositions, such that each solute (Si) atom is surrounded in the nearest-neighbor shell by solvent (Pd) atoms only. In Figure 3-9, the partial pair distribution functions and partial Structural Factor (PSF) for $Pd_{82}Si_{18}$ liquids at 1200K are plotted. No Si-Si bonds have been observed in Figure 3-9a.

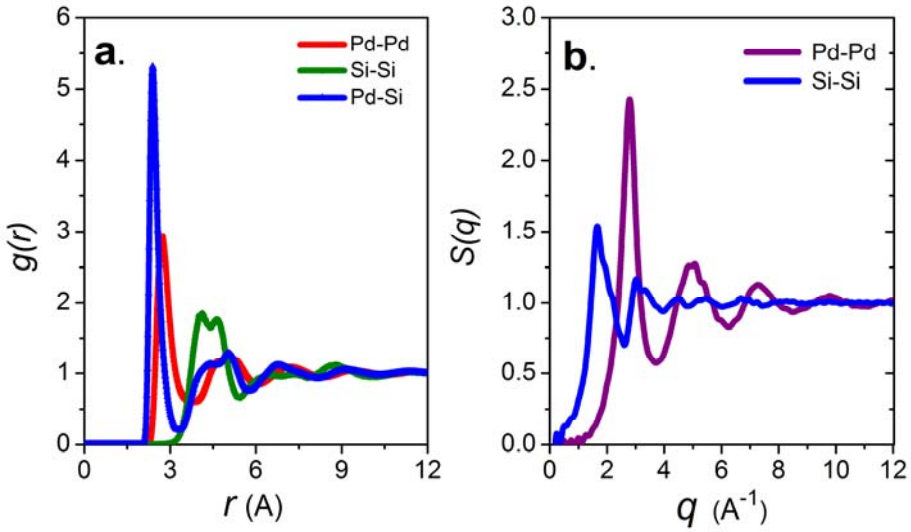

Figure 3-9. (a) Partial pair distribution functions (PPDF) and (b) partial Structural Factor (PSF) for $Pd_{82}Si_{18}$ liquids at 1200K. (1)

For the four most frequent coordination polyhedra in Pd-Si alloy, which are also known to dominate for metal-metalloid amorphous alloys (162, 200)), < 0 3 6 0>, < 0 2 8 0>, < 0 3 6 0>, < 0 4 4 0> as illustrated in Figure 3-10.

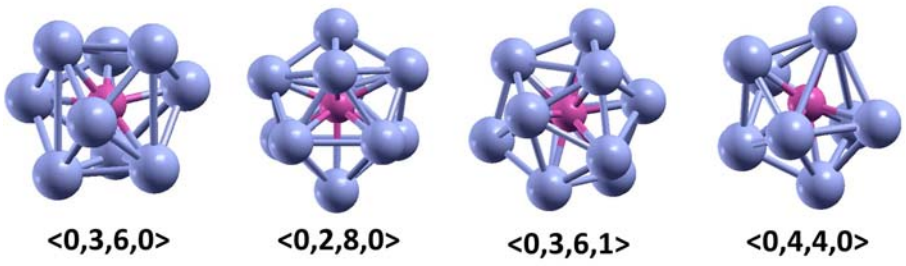

Figure 3-10. Schematic description of four most frequent Si-centered coordination polyhedral in $Pd_{82}Si_{18}$ model glasses.

In Figure 3-11a, the fractions of these most frequent Si-centered local motifs apparently all follow a linear *T* dependence, reminiscent of the *H-T* behavior. With cooling, the atomic packing density increases and the denser polyhedra (CN=9 in this case) become more preferable at the expense of looser ones (e.g., CN=8). But there is no accelerated increase in a particular SRO that preferentially lowers enthalpy as the icosahedra order does in the $Cu_{64}Zr_{36}$ case. Also, there is no improvement in symmetry of the clusters (see the constant BOO in Figure 3-11c), nor additional chemical short-range order (CSRO) (Figure 3-11d) because all of the solute Si center atoms are always surrounded by the solvent Pd as nearest neighbors, as expected for amorphous metal-metalloid alloys near the 80-20 composition (162, 200). The E_{pot} decreases with *T* are all approximately linear with very close slopes, as seen in Figure 3-11b.

The most probable CN thus represents the average structure and the favored SRO in the glass, whereas higher or lower CNs represent inevitable deviations to accommodate the packing frustration (21). The distribution of CNs in Pd-Si MGs is shown in Figure 3-12a. Indeed, for each constituent species there is one (or two) dominant CN, with other (higher/lower) CNs in (much) smaller fractions. One interesting observation is that in each MG the packing around the smaller species (Si) has a narrower distribution of CN and a more dominant characteristic CN, when compared with the case around the larger atoms (Pd). This can be understood from two perspectives. Topologically, smaller atoms tend to have limited possibilities in the CN and SRO, because a missing or extra neighbor corresponds to a larger distortion to the efficient packing scenario (74) and thus higher energy cost. Chemically in $Pd_{82}Si_{18}$ as Si is exclusively surrounded by Pd atoms to form Pd-Si bonds (1, 5). These suggest that Si-

centered ones in Pd-Si, are relatively more ordered and regular. Such dominant and favorable clusters can be treated as respective building blocks (or characteristic local motifs) in this MG.

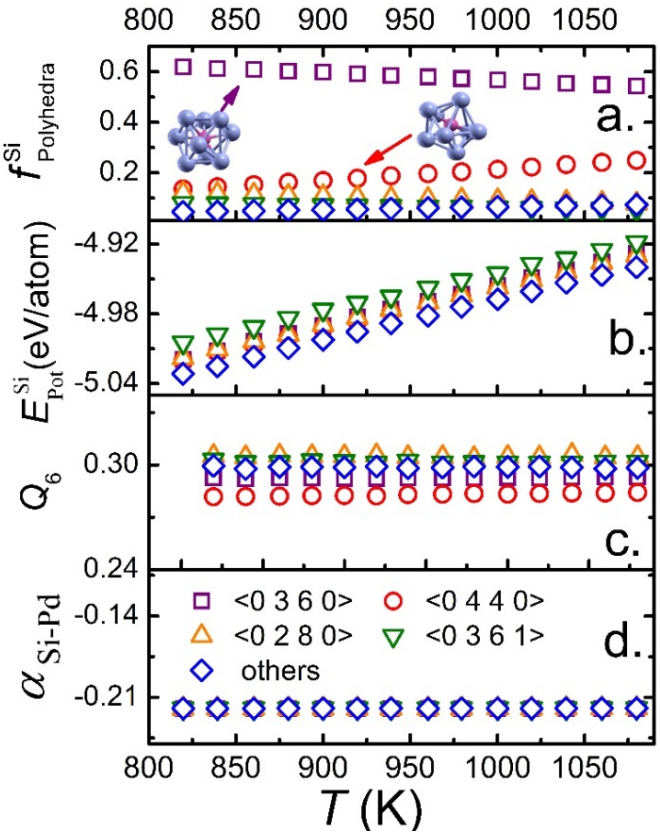

Figure 3-11. (a) Fractions, (b) Potential energy, (c) Q_6, and (d) CSRO of the typical Si-centered polyhedra in $Pd_{82}Si_{18}$. Insets in (a) are two representative Si-centered polyhedra, <0 3 6 0> and <0 4 4 0>. (1)

The next level of detail is the topological arrangement of the CN neighbors surrounding a center atom in the cluster-like motif. One way to describe this is through the Voronoi tessellation analysis, which yields a Voronoi cell and the corresponding

Voronoi index for the atom in question. Figure 3-12b shows the distribution of Voronoi index in our Pd-Si MG (5). Similar to what was found for CN in Figure 3-12a above, the atomic packing around the smaller atoms (Si in Pd-Si) is more regular and dominated by a characteristic type of Kasper polyhedra: the tri-capped trigonal prism <0,3,6,0> for $Pd_{82}Si_{18}$ (a non-icosahedral SRO typical for the solute-lean MGs such as the metal-metalloid systems (1, 5, 162). In general, polytetrahedral packing appears to reign for MGs.

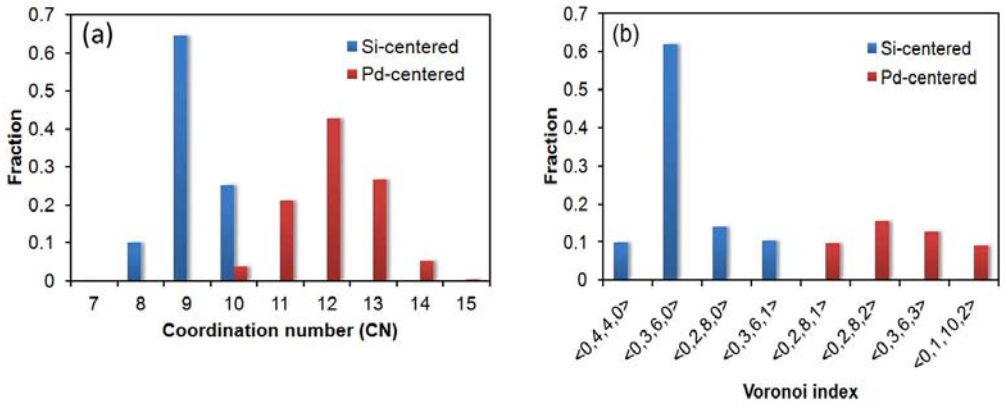

Figure 3-12. (a) Distribution of CNs in $Pd_{82}Si_{18}$ MGs. (b) Distribution of Voronoi indices in $Pd_{82}Si_{18}$ MGs. (5)

Rather than examining the packing topology as outlined above, a different perspective is to focus on the empty space as a structural indicator. This view was inspired by the early models of MG structure, such as the dense random packing of hard spheres. A commonly mentioned parameter is the so-called “free volume”, which is defined as the unoccupied volume in a configuration, in excess of that in the densest packing (232). In more realistic descriptions of metal atoms involving soft spheres or

many-body ion-electron systems, the free volume cannot be unambiguously defined. However, one may still ascribe a volume to each atom to represent the space it occupies, and a convenient way to do this is to use the Voronoi volume determined by the weighted Voronoi tessellation. For a particular atom, a larger (relative to other atoms of the same species) Voronoi volume indicates lower local packing efficiency, and thus the presence of more free volume. Figure 3-13 illustrates the distribution of Voronoi volume in the two MGs (5).

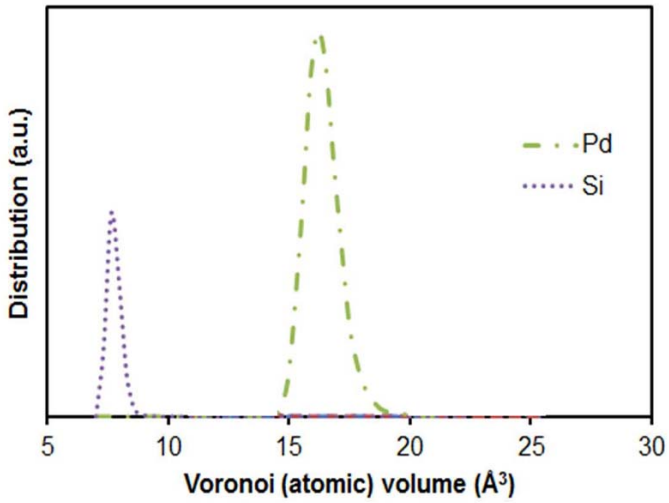

Figure 3-13. Distribution of Voronoi volume in $Pd_{82}Si_{18}$ MGs. (5)

Another parameter that reflects how comfortable an atom is, is the stresses it experiences in the particular local environment. Stress is originally a concept in continuum mechanics, and it is not applicable at atomic level. Egami and collaborators were the first to propose a method to define "atomic-level stresses" (21). The stress on an atom hinges on the energy associated with it, as the thermodynamic stress is expressed as

the first derivative of energy with respect to the strain tensor – the latter can be evaluated by the changes in interatomic distances between the center atom and its neighbors.

Atomic-level stresses in EAM models can be derived following the original work for pair potentials (233). In the current work we will focus on the hydrostatic component, i.e., the atomic-level pressure. Figure 3-14 shows the atomic-level pressure in the Pd-Si MGs. $\sigma\Omega$ can be directly extracted from the MD simulations; to further calculate the stress (pressure in this case) σ, one needs to define the atomic volume, Ω, for each atom, or use the average volume per atom. Since the MG is under zero macroscopic pressure, the average pressure over all atoms is zero. However, the average pressure on a particular constituent element turns out to be non-zero. Si, the smaller species in Pd-Si, is on average under negative pressure (tension), whereas Pd, the larger one, is on average under positive pressure (compression). The reason for this observation is not straightforward, because intuitively, the average pressure felt by any constituent element could be expected to be zero if the structure is fully relaxed. The possible origin could be two-fold, involving both topological and chemical effects. First, since different elements have different atomic sizes, when they are mixed, the average packing scheme, efficiency, and level of frustration around the smaller and larger atoms could be different. If the overall pressure is kept at zero, and it is not possible to satisfy each and every atom (which is the norm in glasses (21)), the smaller and larger atoms may tend to bifurcate in opposite directions and develop non-zero average pressures of opposite signs. Second, different elements have different chemical properties such as the electronegativity. When they are bonded, the chemical interactions such as the charge transfer may also influence the atomic-level stress state (229). As an example, the observation that the larger Zr is

under tension in $Cu_{64}Zr_{36}$ may be counterintuitive at the first glance but can be explained by the chemical effect – the electronegativity of Cu is much higher than Zr, thus there is a strong tendency of charge transfer from Zr to Cu, resulting in an effective compression on the Cu atoms (21). For $Pd_{82}Si_{18}$, it is the larger Pd that has higher electronegativity, so that the tendency of charge transfer is from Si to Pd. Indeed, Pd atoms are on average under compression and Si atoms are almost entirely under tension, and the bifurcation is even more obvious than in $Cu_{64}Zr_{36}$. Compared to the other three indicators discussed earlier, which are all predominantly topological in nature, the atomic-level pressure contains both topological and chemical information. (229, 234)

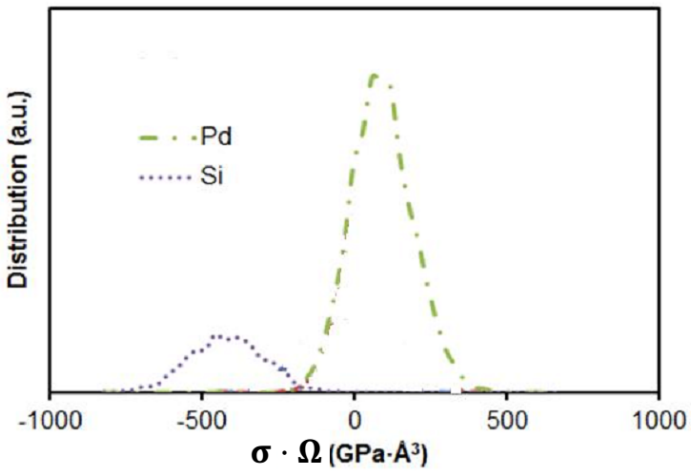

Figure 3-14. Distribution of atomic-level pressure multiplied by atomic volume, in $Pd_{82}Si_{18}$ MGs. (5)

3.3. Conclusions

In summary, we systematically study the structure of two typical MG models, $Mg_{65}Cu_{25}Y_{10}$ and $Pd_{82}Si_{18}$, using the classical and *ab initio* molecular dynamics

simulation. Different from many MGs where the full icosahedral motifs are the key coordination polyhedra, here the featured short-range order (SRO) is dominated by bi-capped square antiprisms (BSAP) or tri-capped trigonal prisms (TTP). In other words, Kasper polyhedra TTPs (and BSAPs) with dense packing are dominant, in lieu of the icosahedral clusters extensively-studied for some MG compositions. In particular, the structure is best perceived in terms of Cu-centered TTPs and BSAPs for $Mg_{65}Cu_{25}Y_{10}$ and for $Pd_{82}Si_{18}$. For Mg-Cu-Y MG model, bond shortening is observed for Mg-Cu and Y-Cu bonds, due to appreciable charge transfer that imparts an ionic character to the bonding. This enhances their chemical affinity, accentuating Cu-centered motifs analogous to solute-centered prisms in metal-metalloid MGs, in this all-metal system. The prism-type SRO is prevalent even at high temperatures in the (supercooled) liquids, as revealed from the inherent structures for both Mg-Cu-Y and Pd-Si. A weak temperature dependence is observed for the degree of characteristic SRO with undercooling, as well as for the development of connections of the motifs in the medium range.

Chapter 4

Local structural signature of excess specific heat and fragility in metallic glass-forming supercooled liquids†

4.1. Introduction of excess specific heat and fragility in supercooled liquids

The specific heat or heat capacity (C_p) is a fundamental property of materials, and especially important for supercooled liquids, from which bulk metallic glasses (BMGs) form via cooling of the melts (8, 10-12, 235, 236). The specific heat C_p of glass-forming supercooled liquids exhibits different temperature (T) dependence: some follow weak T-

†Part of the results has been published in Refs. (1, 3)

dependence in contrast with some others showing rapid development (83-86, 237). C_p shown in Figure 4-1. For these two examples, C_p was directly measured experimentally over a wide range of temperatures in the supercooled liquid. This was possible for the Pd-Ni-Cu-P liquid because of its extraordinary resistance to crystallization (high GFA) (86), and for the marginal BMG former Cu-Zr (238) thanks to the use of an electrostatic levitation technique that allowed large undercooling (171, 239-241). We observe in Figure 4-1 contrasting C_p behavior in terms of the T dependence: Pd-Ni-Cu-P exhibits a shallow C_p curve (weakly T sensitive), whereas that of Cu-Zr shows a very obvious rising trend.

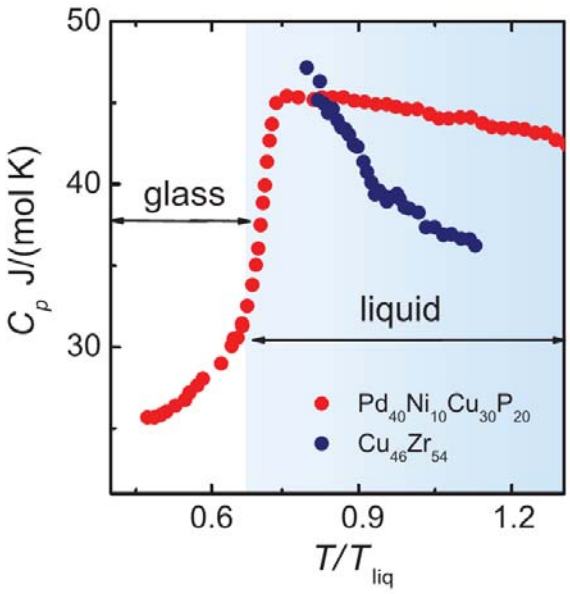

Figure. 4-1. Experimental data of specific heat in the liquid/glassy state for $Cu_{46}Zr_{54}$ and $Pd_{40}Ni_{10}Cu_{30}P_{20}$ MG systems. (1)

Apart from the different evolution of excess specific heat, the different behavior of increasing viscosity on cooling have been extensively observed in supercooled liquids (83-87, 209, 237, 242) (see discussion in Section 1.3.1). Increasing viscosity reflects the decreasing atomic mobility observed in all supercooled liquids. Figure 1-7 shows a "fragility plot" in the form proposed by Angell (83) in which the viscosities of different glass-forming liquids are compared in an Arrhenius plot for which the inverse temperature axis is normalized with respect to glass-transition temperature T_g. The definition of liquid fragility, $m = \left[\frac{d\eta(T_g/T)}{d(T_g/T)}\right]_{T=T_g}$, describes the deviation of the T-dependence of viscosity from the Arrhenius equation. On this normalized scale, the melting point is at ~0.6. All the curves meet at 10^{12} Pa*s, corresponding to the viscosity at T_g. Two extreme cases are distinguished: kinetically "strong" liquids such as SiO_2 show near-Arrhenius behavior (straight line) and have high viscosities (83). On the other hand, kinetically "fragile" liquids such as o-terphenyl exhibit a dramatic temperature-dependence of viscosity just above T_g and viscosities that are up to eight orders of magnitude lower than those of the strongest liquids (86).

Although temperature dependence of specific heat and dynamical viscosity have been extensively studied via experiment and simulation approaches (83-86, 237, 243-245), the underlying structural origin of the very different heat capacity and liquid fragility behaviors remains unclear (241, 246, 247). To tackle this problem, we start molecular dynamics simulations of a relatively fragile $Cu_{64}Zr_{36}$ liquid, in comparison with the "stronger" $Pd_{82}Si_{18}$ and $Mg_{65}Cu_{25}Y_{10}$ metallic liquids (1, 3). While the former system exhibits rapid increase of specific heat in the supercooled liquid region, the latter

two systems show much shallower *T*-dependence. We have demonstrated that the fast rise in excess specific heat can be correlated with increasing structural ordering, and in particular the characteristic SRO as well as the medium-range packing of these local motifs (1, 3). The drop of the enthalpy *H* accelerates with undercooling, as the ordered clusters increase in their number population and improve in their local five-fold symmetry and chemical SRO. The resulting change in the curvature of the *H-T* curve is responsible for the fast rising C_p. Besides, the ordered coordination polyhedra are found to enhance the relaxation time in supercooled liquids. In other words, the supercooled liquid with increasing fraction of ordered cluster exhibit longer bond lifetime and α -relaxation time, as well as increasing viscosity, influencing the liquid fragility.

4.2. Model systems and simulation details

To access atomistic details, we use MD simulations of three different MG-forming model binary alloy supercooled liquids. The first model uses embedded atom method (EAM) interatomic potentials for Cu-Zr, at the composition of $Cu_{64}Zr_{36}$ (1, 6, 174), representing a system that undergoes considerable FISRO in the liquid (6), as discussed in Chapter 2. The second model is based on EAM potentials fitted to the Pd-Si system (see Refs. (1, 5)) that features solute-solute avoidance and solute-centered trigonal prisms as the local SRO in the liquid, typical of metal-metalloid systems (near the 80-20 composition, specifically $Pd_{82}Si_{18}$). The third model focuses on Mg-Cu-Y ($Mg_{65}Cu_{25}Y_{10}$) via EAM empirical potential (Ref. (3) and Section 3.1.1). The latter 2 models have been already described in detail in Chapter 3. While these computer liquid models are expected to have similar local structural motifs when compared with real-world liquids, they are

subject to very different spatiotemporal and sample preparation conditions. As such, they are only meant to show that they can also exhibit the very different heat capacity and fragility trends known for real alloys, but a perfect match with the experimentally measured property values would not be expected.

For the investigated models, a series of liquid configurations (10,000 atoms for Cu-Zr (1) and Pd-Si (1), 54,000 atoms for Mg-Cu-Y (3)) from 2000 K to 300 K were obtained via *NPT* quenching (at zero pressure) from the equilibrium melt (2000 K) at the rate of 10^{10} K/s. At each temperature in the supercooled regime, the configuration was relaxed for 10 ns ~ 100 ns until the total energy leveled off. The relaxed configurations were run under *NPT* at zero pressure for another 10 ns to produce 200 samples at each temperature, from which an average is obtained for the properties to be evaluated. Voronoi tessellation was used to analyze the inherent structure (18, 19).

The enthalpy (*H*) was calculated for zero pressure, including both kinetic and potential energies. The equation we used to fit the *H*-*T* relation is $H = a\ln(T) + bT^2 + cT + d$, where *a*, *b*, *c*, *d* are fitting parameters (1). This equation was chosen because it conforms to the Vogel-Fulcher-Tammann (VFT) (58) description of viscosity $\eta = A\exp\left[\frac{B}{T - T_0}\right]$, and Adam-Gibbs theory (248) $\eta = A\exp\left[\frac{B}{TS_c(T)}\right]$, where $S_c(T)$ is configurational entropy. The above two equations lead to $S_c(T) \sim \left(1 - \frac{T_0}{T}\right)$. Since $\frac{\Delta C_p}{T} = \left(\frac{\partial S_c}{\partial T}\right)_p$, we thus have $\Delta C_p \sim \frac{1}{T}$, where ΔC_p is the difference of heat capacity between the supercooled liquid and the glass at the same temperature. Assuming C_p for

the glass state can be approximated as $c+bT$ in the temperature regime of interest, we have for the liquid $C_p = \frac{dH}{dT} \sim a\frac{1}{T} + bT + c$ and $H = a\ln(T) + bT^2 + cT + d$. (1)

The specific heat C_p can be obtained by two different methods. One is from the fluctuation of enthalpy in liquids, according to $\left\langle \delta(H)^2 \right\rangle_{NPT} = k_B T^2 C_p$, where $\left\langle \delta(H)^2 \right\rangle_{NPT} = \left\langle \delta(U+PV)^2 \right\rangle = \left\langle (U+PV)^2 \right\rangle - \left\langle (U+PV) \right\rangle^2$, and U is the sum of potential and kinetic energy (58). The other method to calculate specific heat of liquids or glasses in MD simulation is based on a large amount of enthalpy data recorded during continuous cooling (240). It is from the definition of heat capacity $C_p = \left(\frac{dQ}{dT}\right)_p = \frac{dH}{dT}$.

For the calculation of shear viscosity for liquids, we used the Green-Kubo equation (58, 249), $\eta = \frac{V}{kT}\int_0^\infty \left\langle P_{\alpha\beta}(0)\cdot P_{\alpha\beta}(t)\right\rangle dt$, Where $P_{\alpha\beta}$ are off-diagonal components of the pressure tensor. In the calculation, we firstly run the equilibrated configurations under NVE ensemble to generate raw data for further calculation. This durations are typically 1000-10000 times the decay time of auto-correlation function *C(t)* for off-diagonal component of pressure: $C(t) = \left\langle P_{\alpha\beta}(0)\cdot P_{\alpha\beta}(t)\right\rangle$.

In computer simulation, α-relaxation time (τ) is usually defined as the time when the self-intermediate scattering function (ISF) has decayed to $e^{-1} \approx 0.3679$ (250, 251). The ISF is expressed as: $F_s^a(q,t) = N_a^{-1}\left(\sum_{k=1}^{N_a} \exp\left\{i\vec{q}\cdot[\vec{r}_k^{\,a}(t) - \vec{r}_k^{\,a}(0)]\right\}\right)$, where a denotes element type, N_a is the number of atoms for element a, $\vec{r}$ and $\vec{q}$ denote position and wave

vector respectively (250, 251). The way that τ is calculated can be illustrated from a specific example in Figure 4-2.

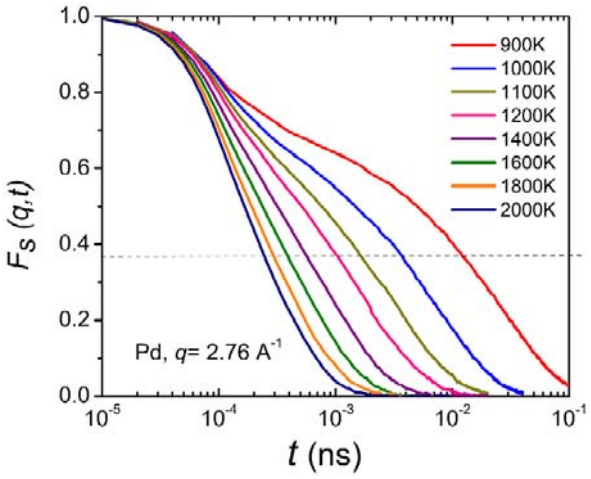

Figure 4-2. Self-Intermediate Scattering Function for Pd in $Pd_{82}Si_{18}$ liquids, with the wave vector q=2.76 A^{-1}. (1)

4.3. Structural signature of excess specific heat of supercooled liquids

The contrasting C_p behaviors suggest that the intrinsic material state (i.e., inherent structure) must evolve with supercooling in different ways and at different rates. This structural origin is expected, because a different T-dependence of the configurational entropy of the liquid, $S_c(T)$, is the root cause of the different C_p behavior, as $\left(\frac{\partial S_c}{\partial T}\right)_p = \frac{\Delta C_p}{T}$, where ΔC_p is the "excess specific heat", i.e., the difference in constant-pressure specific heat between the quasi-equilibrium supercooled liquid and the frozen glass (248). To rephrase this, $\Delta C_p(T)$ is determined by the reduction rate of $S_c(T)$ as the liquid is cooled, such that the underlying structural basis for the different T dependence

of C_p should lie in how and how fast the atoms order themselves to reduce $S_c(T)$. How different this structural evolution would look like, in terms of short-range-ordering (SRO), and how this can lead to the different C_p behavior known for many supercooled liquids that have been experimentally characterized (86), remains largely unknown for realistic alloy liquids and is therefore of general interest (although model Lennard-Jones systems have been studied before (243-245)). This section illustrates this fundamental structural origin by providing a detailed, microscopic picture of the different structural evolution that can be responsible, respectively, for the flat versus fast-ascending C_p curves. This connection is then extended to correlate with and explain the different dynamical properties (relaxation time and viscosity) of our studied alloy liquids.

4.3.1. Comparison between $Cu_{64}Zr_{36}$ and $Pd_{82}Si_{18}$ supercooled liquids

The *H-T* relation of Cu-Zr supercooled liquids in Figure 4-3a exhibits a clear deviation from linearity, and was fit using an equation $H = a\ln(T) + bT^2 + cT + d$, where *a*, *b*, *c, d* are fitting parameters (1), as discussed in Section 4.2. C_p can then be determined by taking the fluctuation of enthalpy (as discussed in Section 4.2); this approach yielded results of C_p in Figure 4-3b. One observes a pronounced C_p rise, showing a trend very similar to the experimental data measured for a similar binary $Cu_{46}Zr_{54}$ MG-forming supercooled liquid (240) (see Figure 4-1, and many other MG-forming liquids (86)). We also calculated the enthalpy data of the solid $Cu_{64}Zr_{36}$ MG configurations between 500 K and 600 K and derived their C_p. ΔC_p at T_g can be estimated to be about 14 J/(mol·K), in reasonable agreement with known experimental data for a number of BMGs (252).

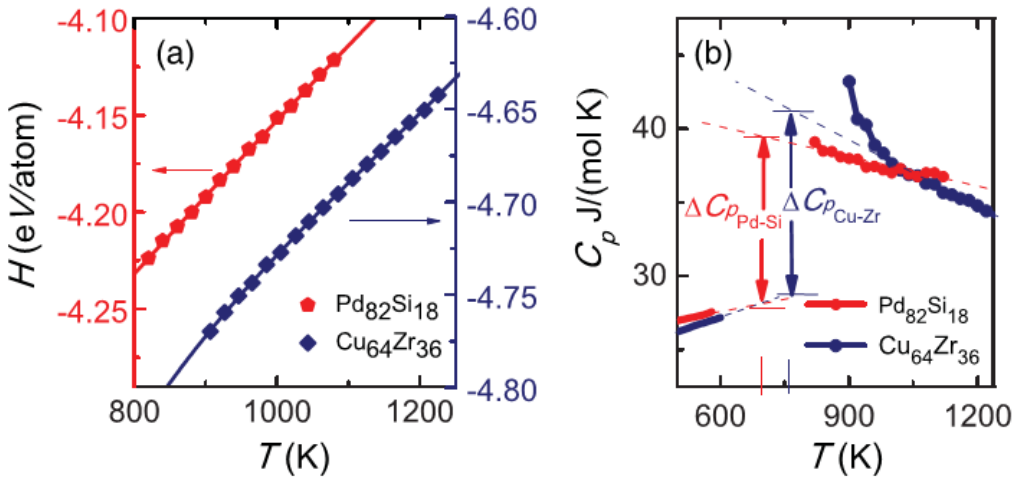

Figure 4-3 (a) The calculated enthalpy (symbols) of the supercooled liquids for $Cu_{64}Zr_{36}$ and $Pd_{82}Si_{18}$ in computer simulation. The lines are the fitted *H-T* curves (1). (b) Specific heat (C_p) calculated using the fluctuation method for Cu-Zr and Pd-Si. (1)

The behavior of the $Pd_{82}Si_{18}$model supercooled liquid is also shown in Figure 4-3. The *H-T* relation of $Pd_{82}Si_{18}$ is quite different from that of $Cu_{64}Zr_{36}$ with much less curvature, as shown in Figure 4-3a. The $C_p(T)$ curve in Figure 4-3b calculated using the fluctuation method (and the derivative approach as well in Figure 4-4) is rather flat, much less *T*-dependent than the Cu-Zr case. This resembles some MG-forming liquids, including some of the metal-metalloid systems such as the one in Figure 4-1. Meanwhile, Figure 4-4 exhibits the heat capacity of Cu-Zr and Pd-Si model systems from definition of $C_p = \left(\frac{dQ}{dT}\right)_p = \frac{dH}{dT}$. The advantages for this method are easy computation and span over a large temperature range. But due to the very high cooling rate ($\geq 10^9 K/s$) in

computer simulation, most of enthalpy data in liquids, especially supercooled liquids, are not from quasi-equilibrium configurations. We can see that the C_p at high temperatures are very similar to our results in the Figure 4-3. Having obtained the contrasting ΔC_p behavior in our two model liquids, the next step is to analyze the structural origin responsible, which may shed light on the different ΔC_p behavior in real-world MG-forming supercooled liquids.

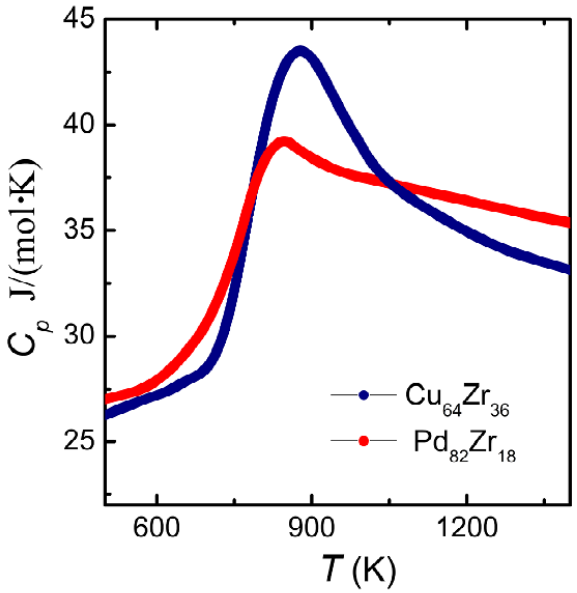

Figure 4-4. Specific heat of $Cu_{64}Zr_{36}$ and $Pd_{82}Si_{18}$ calculated from continuous MD cooling (1).

Before analyzing the role of structural evolution during cooling in controlling C_p, we note that for $Cu_{64}Zr_{36}$ at all temperatures the enthalpy of all the Cu atoms is an almost fixed fraction, 0.480±0.002, of the total system H. Taking them to be representative of

the whole system, in the following we will therefore examine the energies of Cu atoms and will focus on all the Cu-centered coordination polyhedra, to uncover the structural evolution responsible for the *H* change. A similar scaling is also found for $Pd_{82}Si_{18}$: the contribution of the minority (solute Si) atoms to the system *H* is also a constant fraction of 0.2086±0.0004 at all temperatures.

We now monitor the structural features throughout the supercooled liquid regime. For $Cu_{64}Zr_{36}$, the five most frequent Voronoi indices are <0 0 12 0>, <0 2 8 2>, <0 2 8 1>, <0 2 8 0>, <0 3 6 3>, for the Cu-centered polyhedral (1, 6), see their evolution in Figure 4-5a. To find out how each one contributes to the bending of the *H*-*T* in Figure 4-3a, we separate and plot in Figure 4-5 their individual contributions. Because the total kinetic energy of the Cu atoms in the centers of the polyhedra shows a linear relation with *T*, contributing only a constant value to C_p, we can just focus on the potential energy (E_{pot}) change of Cu-centers and relate their contribution to their structural ordering. Figure 4-5b plots the change of E_{pot}, on a per atom basis and relative to the value at 1220 K, for Cu center atoms in polyhedra of different indices. It is obvious that the average E_{pot} of Cu-centers inside full icosahedra (FI), with Voronoi index <0 0 12 0>, have dropped nonlinearly with decreasing *T* much faster than all the others. A similar trend is observed, but to a lower degree, for the other polyhedra with a coordination number (CN) of 12, such as <0 2 8 2>, which can be viewed as more distorted icosahedra. In comparison, Cu centers in <0 2 8 0> polydedra displayed a nearly linear relation. Moreover, we see in Figure 4-5a that the fraction of Cu-centered FI (<0 0 12 0>), which has lower E_{pot} relative to others (Figure 4-5b), rises significantly upon cooling towards T_g at the expense of other polyhedra (the fraction of FI reaches ~0.21, much greater than a previous

simulation at the same temperature (181), because of the prolonged MD relaxation to reach quasi-equilibrium supercooled liquid state in this study). The above results suggest that the excess specific heat, i.e., the fast rise of ΔC_p with decreasing T in the supercooled liquid region, is due to the extraordinary enthalpy reduction associated with icosahedral ordering.

The nonlinear reduction of average E_{pot} with decreasing T for Cu atoms embedded in FI can be attributed to the improved icosahedral symmetry, as revealed by the bond orientational order parameter (BOO), as discussed in Section 1.2.2.5 (81, 82). Specifically, the BOO of neighboring atoms surrounding the center atom can be quantified using a set of spherical harmonics, so that different types of local order often yield different values. For example, $\overline{Q_6}$, which is an effective indicator of icosahedral order (81, 82), increases at lower temperatures, particularly strongly in FI. This improvement in symmetry renders the atoms more favored, lowering their energy and configurational entropy. In contrast with this trend of improved topological order in icosahedra and distorted icosahedra (see the relative change of BOO in Figure 4-5c), the <0 2 8 0> polyhedra exhibit almost constant $\overline{Q_6}$ across the entire T range. The dramatic increase of FI fraction, which is another aspect of the growing icosahedral order as discussed in the last paragraph, compounding the symmetry improvement of the average FI to reduce the enthalpy, constitutes the topological signature underlying the fast-ascending ΔC_p.

As for chemical short-range order (CSRO), the Warren-Cowley parameter (α_{AB}) was used to characterize the chemical make-up of the nearest-neighbor pairs (40, 253).

Figure 4-5d demonstrates a more negative CSRO in the polyhedra with undercooling, indicating the increasing preference for more unlike (Cu-Zr) bonds that reduce energy. Note that the CSRO is not independent of topological order and goes hand in hand with icosahedral ordering (18, 174), facilitating the latter. The simulation results above are consistent with the experimental trend found by Wessels *et al* (240).

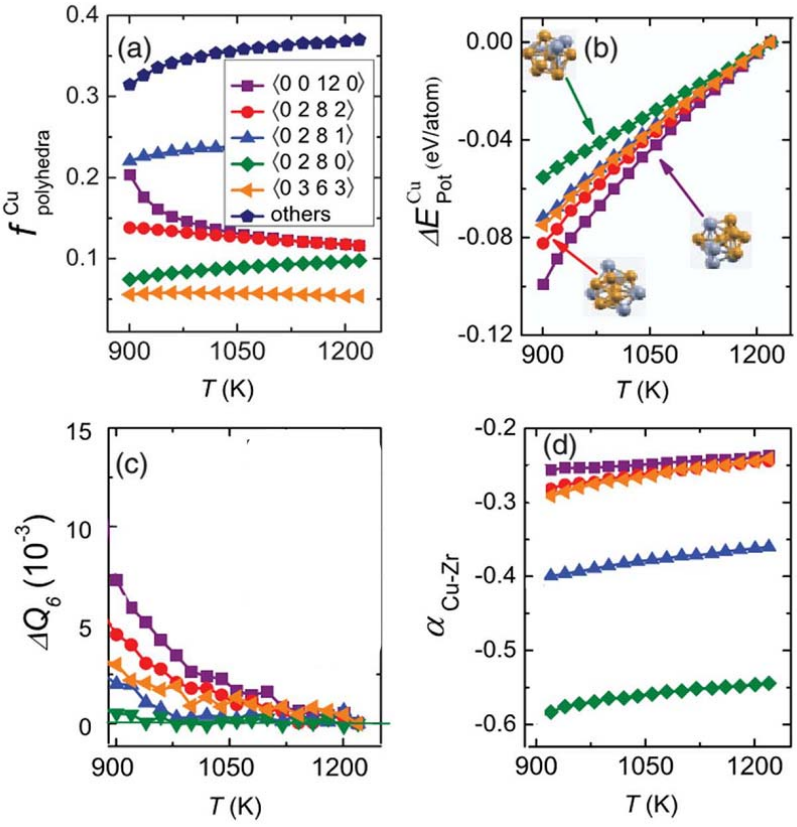

Figure 4-5. SRO analysis of $Cu_{64}Zr_{36}$ supercooled liquid: (a) Fractions of the most frequent Cu-centered polyhedra. (b) Potential energy difference of Cu atoms in several key polyhedra, relative to the reference state at 1220 K. Insets show three representatives: <0 0 12 0>, <0 2 8 2>, <0 2 8 0>. (c) ΔQ_6 (change of Q_6 with reference state at 1220 K). (d) the Warren-Cowley parameter (α_{Cu-Zr}). (1)

We next demonstrate that in the absence of such structural ordering through the supercooled liquid region, C_p stays rather flat as opposed to fast-rising. We illustrate this using the Model II liquid, $Pd_{82}Si_{18}$. For the four most frequent polyhedra in this alloy (Figure 3-10 and Figure 3-11 in Chapter 3), which are also known to dominate for metal-metalloid amorphous alloys (18)), < 0 3 6 0>, < 0 4 4 0>, < 0 2 8 0>, < 0 3 6 1>, the E_{pot} decreases with T are all approximately linear with very close slopes, as seen in Figure 3-11b, contributing a constant to C_p. The fractions of these local motifs apparently all follow a linear T dependence, reminiscent of the H-T behavior in Figure 4-3a. With cooling, the atomic packing density increases and the denser polyhedra (CN=9 in this case) become more preferable at the expense of looser ones (e.g., CN=8). But there is no accelerated increase in a particular SRO that preferentially lowers enthalpy as the icosahedra order does in the $Cu_{64}Zr_{36}$ case. Also, there is no improvement in symmetry of the clusters (see the constant BOO

in Figure 3-11c), nor additional CSRO (Figure 3-11d) because all of the solute Si center atoms are always surrounded by the solvent Pd as nearest neighbors, as expected for amorphous metal-metalloid alloys near the 80-20 composition (18, 19, 162). The result is a rather flat C_p.

4.3.2. Comparison between $Cu_{64}Zr_{36}$ and $Mg_{65}Cu_{25}Y_{10}$ supercooled liquids

Armed with knowledge about the atomic and electronic structures developed in the amorphous $Mg_{65}Cu_{25}Y_{10}$ alloy (see details in Section 3.1), we are now in the position to explain its macroscopic properties during supercooling of the liquid to form the MG. The C_p for the EAM-MD-derived $Mg_{65}Cu_{25}Y_{10}$ is plotted in Figure 4-6a. The magnitude of

the C_p, as well as the shallow C_p curve (*i.e.,* the weak temperature dependence), is also consistent with the experimentally measured C_p for $Mg_{65}Cu_{25}Y_{10}$ (with only minor deviation (87)) cited in Figure 4-6(a). The excess specific heat at experimental T_g, ΔC_p, is estimated to be 13.5 J/(mol·K), which is consistent with previous measurements in both experiments and simulations for various BMG-forming alloys (252). The corresponding quickly rising C_p has been reported in Ref. (1) and the experimentally measured C_p for $Zr_{54}Cu_{46}$ (240) is included in Figure 4-6 (b), to contrast with the behavior of $Mg_{65}Cu_{25}Y_{10}$.

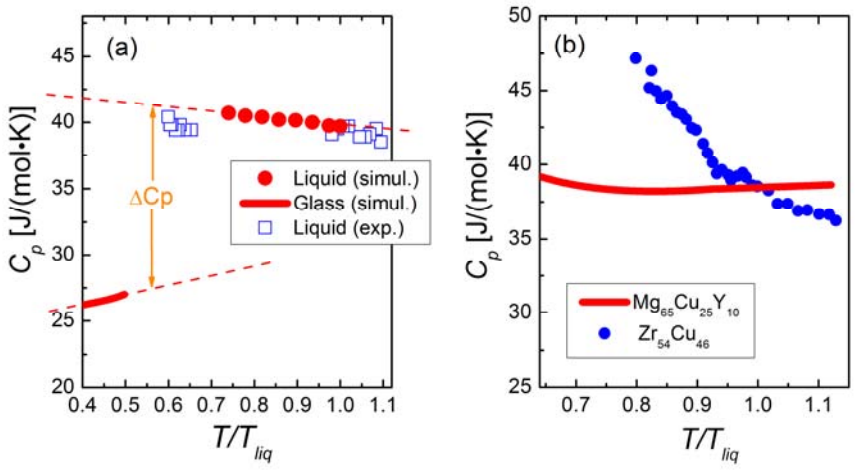

Figure 4-6. (a) Specific heat of EAM MD-derived $Mg_{65}Cu_{25}Y_{10}$, compared with experiment data (87). (b) Fitting of experimental data of specific heat for the $Mg_{65}Cu_{25}Y_{10}$ liquid (87); also included for comparison is the experimentally measured C_p of $Zr_{54}Cu_{46}$ liquid. (3)

The rather flat C_p curves seen in Figure 4-6a can now be explained by the temperature dependence of the structural evolution (Figure 4-7 as well as Figure 3-4) from the ordering perspective. Figure 4-7 plots the fraction of TTPs and BSAPs as a function of temperature within the $Mg_{65}Cu_{25}Y_{10}$ supercooled liquid regime, adopted from

Figure 3-4. These SROs developed around Cu atoms increase only moderately and gradually with decreasing temperature. A salient feature there is that the characteristic SRO (TTP and BSAP) is very pronounced rather early, even at high temperatures near the liquidus temperature (T_l) in the equilibrium liquid. This implies a relatively low configurational entropy in the liquid already at temperatures around T_l. The strong ordering tendency in this alloy is boosted by the large electronegativity difference and the obvious charge transfer we discussed in Section 3.1.4. Macroscopically one can also cite the large negative heat of mixing between Cu and Y (ΔH^{mix} = -22 kJ/mol) (230) to argue for the strong CSRO. Therefore, there is a high driving force for intimate atomic-level mixing of the elements, with Cu surrounded by unlike neighbors, even in liquid at elevated temperatures.

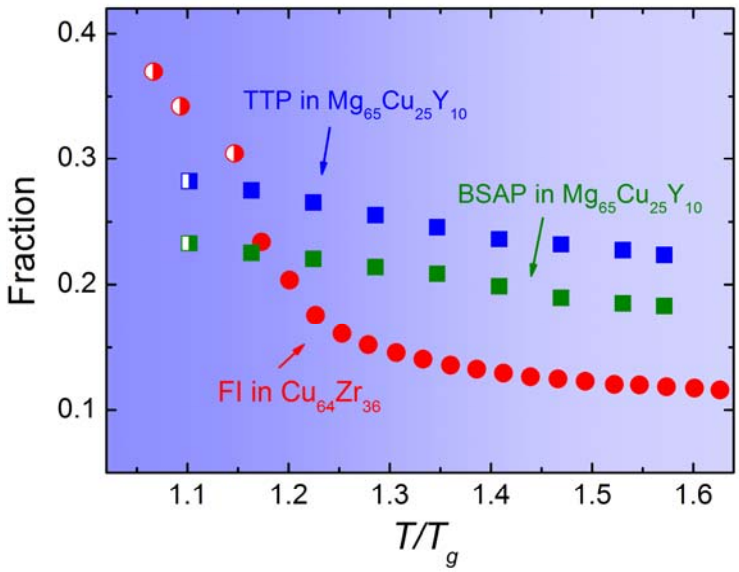

Figure 4-7. Fraction of Cu-centered TTPs and BSAPs as a function of temperature of the $Mg_{65}Cu_{25}Y_{10}$ supercooled liquid. For comparison, the fraction of FI in $Cu_{64}Zr_{36}$is also included. (3)

Figure 4-7 indicates that the fractions of TTPs and BSAPs increase only gradually and slightly within the supercooled liquid. The additional ordering upon continued supercooling in the liquid is moderate (in contrast to the dramatic rise in ordering in Cu-Zr liquid, also included in Figure 4-7, adopted from Ref.(1) and Figure 4-5). Also, as shown in Figure 3-5 (see Chapter 3), the medium-range ordering in Mg-Cu-Y is also only weakly temperature dependent, which is quite different from behavior of Cu-Zr supercooled liquid in Figure 2-7a. That correlation between structural evolution and temperature dependence of specific heat is expected because the different T-dependence of the configurational entropy of the liquid, $S_c(T)$, is the root cause of the different C_p behavior, as $\left(\frac{\partial S_c}{\partial T}\right)_p = \frac{\Delta C_p}{T}$ (248), as previously discussed in Section 1.3.1. To rephrase this, $\Delta C_p(T)$ is determined by the rate of reduction of $S_c(T)$ as the liquid is cooled. Therefore, the underlying structural basis for the different T dependence of C_p should lie in how and how fast the atoms order themselves to reduce the configurational entropy $S_c(T)$. Consequently, the $S_c(T)$ is rather flat with temperature and the enthalpy of the alloy does not decrease rapidly with a fast-increasing slope (C_p). The C_p (T) curve is then expected to be relatively shallow. This behavior is indeed what is observed in the simulation data in Figure 4-6a, and in the flat C_p curve experimentally measured (see Figure 4-6a and 4-6b). In contrast, a more fragile system such as the $Cu_{64}Zr_{36}$ supercooled liquid (1) starts out with a much lower degree of SRO at T_l, but undergoes rapid SRO development in the supercooled liquid, see the steep rise in FI ordering in Figure 4-7 (the

medium-range connection of FI also shows a fast ascending trend in this same temperature range, Fig. 2-7a).

4.4. Structural origin underling dynamical slowdown in supercooled liquids

It is well known that the relaxation dynamics of the supercooled liquid (as measured by viscosity η or relaxation time τ) can be connected with thermodynamic properties via the Adam-Gibbs equation (248),

$$\eta = A\exp\left(\frac{B}{TS_c(T)}\right). \quad (4\text{-}1)$$

Here A and B are constants, and $S_c(T)$ is again the configurational entropy of the liquid. If S_c is T-independent, the viscosity should follow Arrhenius behavior, as demonstrated by the linear relationship in the $\log(\eta)\sim (T_g/T)$, or the Angell plot (83). However, in most liquids $S_c(T)$ decreases with decreasing T, such that the $\log(\eta)\sim\log(T_g/T)$ curve bends upward. As discussed before, the fragility of the liquid correlates strongly with how C_p (1, 86), and structural ordering (1), evolves with temperature (T) during undercooling.

Figure 4-8 compares the α-relaxation time (τ) for all species in both $Cu_{64}Zr_{36}$ and $Pd_{82}Si_{18}$ liquids (see Ref. (1)). The solid lines are VFT (58) fittings for the Si and Zr data. In each liquid the absolute τ value may vary with different species (dashed line vs. solid line), but the trend is almost identical. Figure 4-8 demonstrates that $Cu_{64}Zr_{36}$ liquid is more fragile than $Pd_{82}Si_{18}$. In the inset we also present viscosity (η) data (calculated via

Green-Kubo equation (58)) and VFT fitting for the two liquids. Vogel-Fulcher-Tammnn (VFT) equation (58),

$$\tau = A\exp\left[\frac{B}{T - T_0}\right], \tag{4-2}$$

where A, B, and T_0 are fitting parameters. Although it is difficult for computer simulation to assess viscosity at low temperatures, the trend seen here is consistent with the assessment of fragility difference given by the τ data. The observed difference in the T-dependence of τ or η is not surprising, as we have shown earlier that $Cu_{64}Zr_{36}$ undergoes more dramatic local structural ordering than $Pd_{82}Si_{18}$, and hence a steeper rise of configurational entropy, with T decreasing towards T_g. In other words, the ascending C_p-T curve and higher fragility, i.e., the two key thermodynamic and kinetic properties, correlate with one another (31) and have common origin in the atomic-level structural evolution.

Figure 4-9 compares α-relaxation time of Cu in $Cu_{64}Zr_{36}$ and $Mg_{65}Cu_{25}Y_{10}$ liquids as a function of temperature (3). Specifically, the shallow $C_p(T)$ curve of the $Mg_{65}Cu_{25}Y_{10}$ liquid suggests that its viscosity should deviate from Arrhenius behavior less significantly than the one with a steep $C_p(T)$ curve. Structurally, the $S_c(T)$ of $Mg_{65}Cu_{25}Y_{10}$ liquid displays a much weaker temperature dependence than that of Zr-Cu liquid. In other words, the $Mg_{65}Cu_{25}Y_{10}$ liquid should appear stronger than the Zr-Cu one, on the basis of the Gibbs-Adam equation mentioned above. To demonstrate this comparison, the α-relaxation time, which is correlated with the viscosity of liquids, is shown in Figure 4-9.

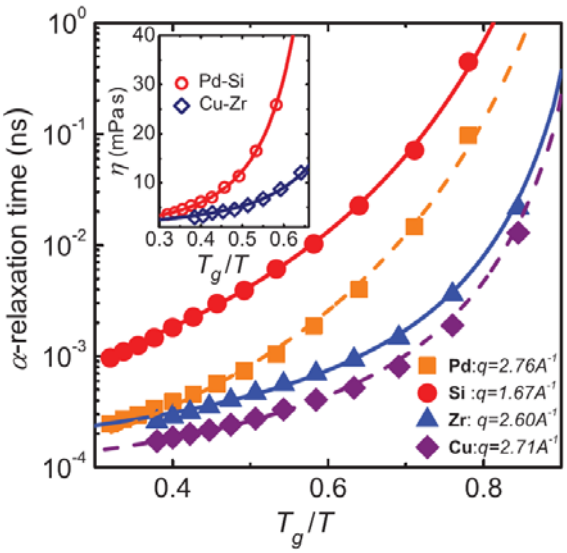

Figure.4-8. α-relaxation time (symbols) for each species in $Cu_{64}Zr_{36}$ and $Pd_{82}Si_{18}$ liquids. The data can be well represented by VFT fitting. The inset shows viscosity data for $Cu_{64}Zr_{36}$ and $Pd_{82}Si_{18}$ liquids and their VFT fitting. (1)

Figure 4-9 indicates that $Mg_{65}Cu_{25}Y_{10}$ is indeed a stronger liquid relative to the more fragile binary Zr-Cu. A stronger liquid is projected to favor a higher GFA, because the rising viscosity with undercooling tends to retard crystal nucleation and especially growth kinetics (86). For the more fragile liquid, the viscosity rise is delayed to the temperature region close to T_g, leaving a wider temperature window in the undercooled liquid that may facilitate crystallization, leading hence to lower GFA.

Also, Figure 4-10 plots the bond-breaking time or bond lifetime (183, 254) of $Cu_{64}Zr_{36}$ and $Mg_{65}Cu_{25}Y_{10}$ supercooled liquids with temperature. The behaviors of bond-breaking time for those two liquids are very similar with their α-relaxation time presented

in Figure 4-9: Mg-Cu-Y is indeed a stronger liquid relative to the more fragile binary Zr-Cu.

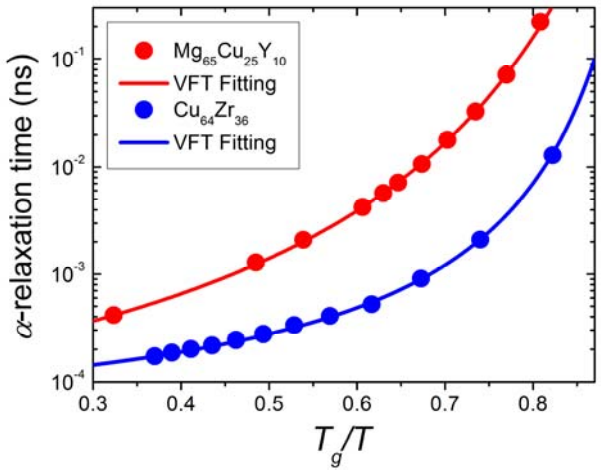

Figure 4-9. α-relaxation time as a function of temperature (in the format of Angell plot (83)). The solid lines are the fitting curves using the VFT equation. (3)

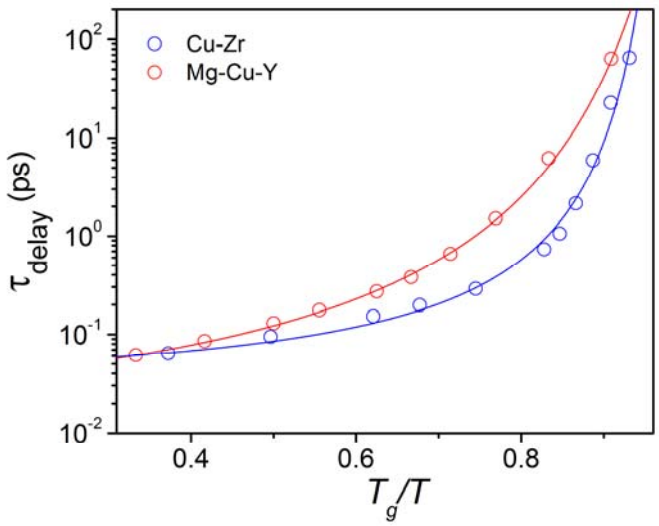

Figure 4-10. Bond-breaking time of $Cu_{64}Zr_{36}$ and $Mg_{65}Cu_{25}Y_{10}$ supercooled liquids as a function of temperature. The solid lines are the fitting curves using the VFT equation.

As discussed in Figure 4-7, the SRO evolve during cooling in $Cu_{64}Zr_{36}$ and $Mg_{65}Cu_{25}Y_{10}$ supercooled liquids, which are consistent with behavior of liquid relaxations as illustrated in Figure 4-9 and Figure 4-10. The direct link between local structure and dynamics relaxations can be observed in Fig. 4-11, where bond-breaking time for Cu-centered coordination polyhedra in $Cu_{64}Zr_{36}$ (800K) and $Mg_{65}Cu_{25}Y_{10}$ (600K) supercooled liquids are plotted. Especially, Cu-centered <0,0,12,0> (FI) in $Cu_{64}Zr_{36}$ and <0, 2, 8, 0> (BSAP) (as well as <0, 3, 6, 0>, TTP) in $Mg_{65}Cu_{25}Y_{10}$ model systems exhibit much longer bond-breaking time than atoms centered in other coordination polyhedra. The role of Cu-centered <0, 0, 12, 0> in $Cu_{64}Zr_{36}$ as enhancement of dynamical slowdown is consistent as discussion in Section 2.3.2.

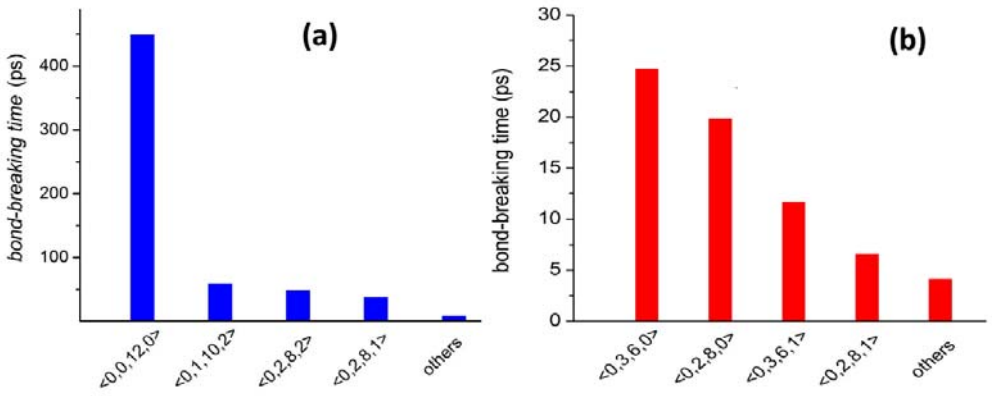

Figure 4-11. Bond-breaking time for (a) Cu-centered coordination polyhedra in $Cu_{64}Zr_{36}$ supercooled liquids at 800K and (b) Cu-centered coordination polyhedra in $Mg_{65}Cu_{25}Y_{10}$ supercooled liquids at 600K.

4.5. Conclusion

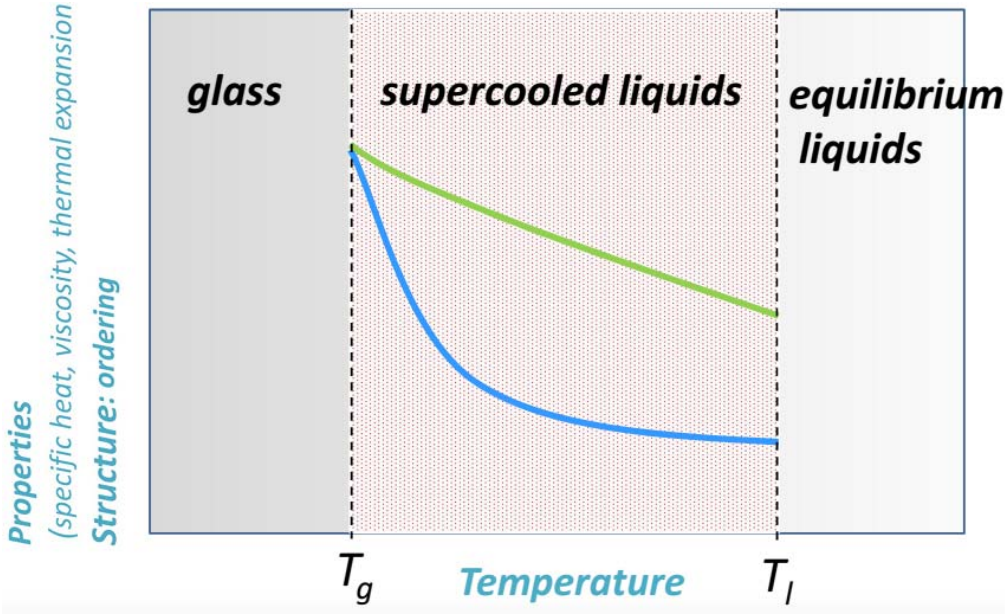

Figure 4-12. Schematic description of evolution of local structure and properties upon undercooling toward glass transition within supercooled liquids: gradual (green line) vs sharp changes (blue line).

In conclusion, we have demonstrated that the rise in excess specific heat and dynamical slowdown in supercooled liquids can arise from the increasing development of structural ordering, and in particular the SRO and MRO (via cluster connection schemes). Three different model systems have been investigated using molecular dynamics simulation: more fragile liquid of $Cu_{64}Zr_{36}$ and relatively stronger liquids of $Pd_{82}Si_{18}$ and $Mg_{65}Cu_{25}Y_{10}$. The schematic description of structure and properties evolution are plotted in Figure 4-12, where two contrasting behavior with temperature can be observed during

undercooling. One is gradual change upon undercooling, such as structural ordering, excess specific heat, dynamical slowdown (as illustrated in this chapter between Cu-Zr and Mg-Cu-Y/Pd-Si supercooled liquids). The other is slow change from liquidus temperature, but rapid variation towards glass transition, as seen in Cu-Zr model supercooled liquids. Other consistent findings on thermal expansion of supercooled liquids can be found in Ref. (241).

Chapter 5

Structural signature of elastic heterogeneity in metallic glasses[†]

Mechanical behaviors of metallic glasses are quite distinct and intriguing (97, 98, 117, 118, 210, 255, 256), compared to their alloy crystalline counterpart, as discussed in Section 1.3.2. One aspect is the elastic heterogeneity (112, 115, 116) and in this chapter, we study the structural origin underlying this character in metallic glasses via molecular dynamics simulation (2, 4). Three aspects of structural origin of heterogeneous elasticity

[†]Part of the results has been published in Refs. (2, 4, 6)

will be discussed. One is about how the degree of elastic deformation correlates with the internal structure on the atomic level. The second one is to quantitatively evaluate the local solidity/liquidity in metallic glasses (i.e., how solid-like/liquid-like a local region/configuration is), as well as to establish a correlation between the solidity/liquidity and the local topology and order, across the whole range of atomic configurations. And the third one shows the role the extended icosahedral ordering plays in constituting a stiff backbone and elevating the shear modulus of the glass (6).

5.1. Correlating local structure with inhomogeneous atomic strain in $Cu_{64}Zr_{36}$ metallic glass

In this Section, we use MD simulations to correlate the elastic heterogeneity with local disorder in a model $Cu_{64}Zr_{36}$ MG (2). We quantify the wide distribution of the atomic strain and non-affine deformation within apparently elastic regime, and demonstrate that the inhomogeneous deformation can be well correlated with local structure: for our model Cu-rich MG, we can observe a clear difference between the response of Cu atoms in Cu-centered full-icosahedra (Cu-FI, Voronoi index <0, 0, 12, 0> (2, 4, 6, 18)) clusters and those that do not have full-icosahedral surroundings (noted as Cu-non-FI). We also discuss the influence of local structure on non-affine displacement of atoms at the MD time scale during elastic deformation.

5.1.1. Model systems

The sample of $Cu_{64}Zr_{36}$ with 1.25 million atoms was equilibrated at 2500 K for 500 ps and then quenched to 10 K with a cooling rate of 10^{12} K/s under Nose-Hoover thermostat (the external pressure was barostated at zero) (2, 58, 59). The periodic boundary condition is applied in all three directions. The Cu-Zr EAM potential, optimized for this binary glassy system, was adapted from Ref. (174). At 10 K, the dimension of the Cu-Zr MG is 27.05 nm × 27.05 nm × 27.05 nm. In order to minimize the effect of thermal fluctuation, the compression of the sample was done at 10K, with the strain rate of 10^{-4}/ps in the x-direction as shown in Figure 5-1, with zero pressure kept in both y and z directions. The imposed strain tensor for the uniaxial compression is $\varepsilon = \begin{pmatrix} \varepsilon_x & 0 & 0 \\ 0 & \varepsilon_y & 0 \\ 0 & 0 & \varepsilon_z \end{pmatrix}$, where $\varepsilon_y = \varepsilon_z$. The Voronoi tessellation analysis (18) (as discussed in Section 1.2.2.4) shows that 16% of Cu atoms are centers of full icosahedra (FI) in this sample. Note that the software of *VORO++* (257, 258) was employed to carry out Voronoi tessellation in Section 5.1 and 5.2 in order to perform the analysis efficiently among ~million atoms sample. The obtained results, such as fraction of icosahedra exhibit a bit difference from the measurement in the smaller samples of this thesis because of different criterion to dump trivial constructed faces. The cooling rate has an effect on the resulting structure, as revealed previous discussion in Chapter 2. In laboratory MG samples, where the cooling rate is several orders of magnitude lower (10-12, 86, 235), this fraction is expected to be even higher. The compressive stress-strain curve of this MG is displayed in Figure 5-1. The yield stress is ~2.7 GPa, at the strain of about 5%. Since this study focuses on the regime of apparently elastic deformation, the

following analysis will be conducted at below ~4% strain, where the stress-strain curve is almost linear.

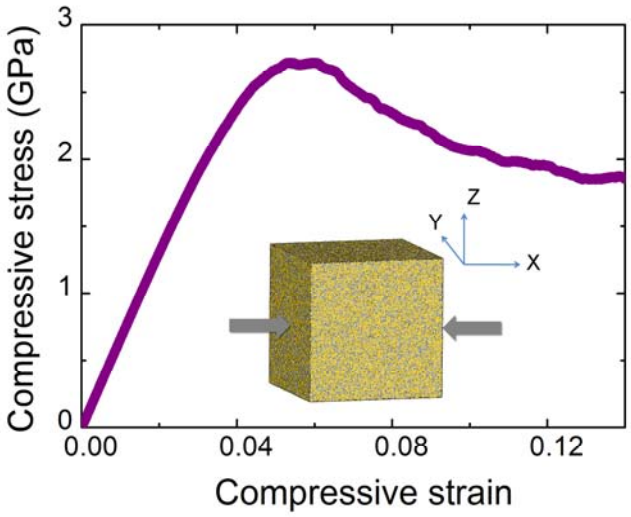

Figure 5-1. Strain-stress curve of the simulated $Cu_{64}Zr_{36}$ MG under compression. Inset shows the schematic of the sample under compression in the x-direction. Yellow spheres represent Cu atoms and grey ones for Zr atoms. (2)

5.1.2. Short-range order correlated local strain in $Cu_{64}Zr_{36}$ metallic glass

In order to define the atomic strain, we employed the definition of locally affine transformation matrix, J_i (259), that best maps: $\{d_{ji}^0\} \rightarrow \{d_{ji}\}, \forall j \in N_i$, where N_i are the nearest neighbors of the ith atoms, and d_{ji}^0 and d_{ji} are bond vectors for old and current configurations between jth and ith (central) atoms. Then the Lagrangian strain matrix is

$$\eta_i = \frac{1}{2}(J_i J_i^T - I) \tag{5-1}$$

and the locally non-affine displacement of the central atom *i* relative to its nearest neighbor atoms *j,* is defined as (260):

$$D^2_{\min,i} = \frac{1}{N}\sum_j \left[\vec{r}_j(t) - \vec{r}_i(t) - J_i\left(\vec{r}_j(t-\Delta t) - \vec{r}_i(t-\Delta t)\right)\right]^2. \tag{5-2}$$

Here we analyze the atomic strain, defined in terms of Eq. (5-1) above, in the loading direction (η_i^{xx}) and two transverse directions (η_i^{yy} and η_i^{zz}). The distribution of η_i^{xx} is shown in Figure 5-2a, at the imposed global strain of -2% (well within the elastic region, see Figure 5-1; negative value means compression). The areas under the curves for Cu-FI and Cu-non-FI are normalized to unity. Note that for individual atoms the atomic strain spans a range of -6% to 2%, which can be as large as 2 to 3 times the imposed global strain. The fairly wide distribution is very different from the scenario of homogeneous deformation, which is represented by the yellow spike in Figure 5-2a at the imposed strain. Clearly, the atomic strain during apparently elastic regime in the MG is highly inhomogeneous (261).

We next examine if the different local structure can be correlated with the propensity for elastic deformation. In Figure 5-2a, the atomic strains of Cu-FI atoms exhibit a narrower distribution than the Cu-non-FI ones, while the total average is close to the imposed -2%. Also, the average value of the Cu-FI spectrum is lower than that of Cu-non-FI. Apparently, Cu atoms in the FI clusters, which are the local motifs believed to be of more efficient packing for this composition, lower energy and hence higher stability (6, 18, 179, 181, 188), behave stiffer and more homogeneous than the other ones.

Figure 5-2b illustrates the difference between the atomic strain and the imposed global strain, showing their evolution with loading time in both the loading and transverse directions. It can be observed that below 2.3% the atomic strain averaged over all the Cu atoms is almost overlapped with the imposed strain (black lines; we see that the atomic strain averaged over Cu-FI atoms is about 16% lower than that for the rest Cu atoms (Cu-non-FI). This is consistent with the indication in the case of 2% imposed compressive strain shown in Figure 5-2a: the imposed strains are carried for the most part by the Cu-non-FI atoms.

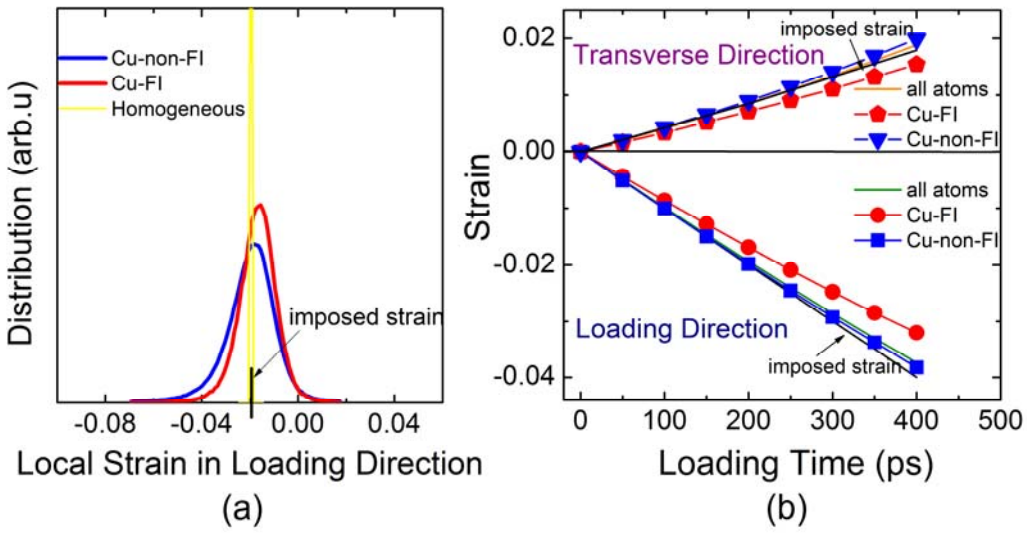

Figure 5-2. (a) Distribution of atomic strains at 2% imposed compressive strain. The blue and red curves have been normalized to unity. (b) Comparison between average atomic strain and imposed strain in the loading and transverse directions, along with the loading time. (2)

In Figure 5-3a, we show how D^2_{min} evolves with increasing compressive strain. Apparently, the average D^2_{min} for Cu-FI atoms is only about one half of that for Cu-non-FI atoms, indicating that more relaxation (in the form of non-affine displacement) happened for the latter kind. Figure 5-3b shows the distribution of D^2_{min} for both the Cu-FI and Cu-non-FI atoms at the compressive strain of 2% (normalized to unity). It is observed that D^2_{min} for Cu-FI exhibits a narrower distribution and smaller mean value, consistent with the results in Figure 5-3a. Thus we can conclude that the Cu-FI atoms deform in a more locally affine manner with less atomic relaxation.

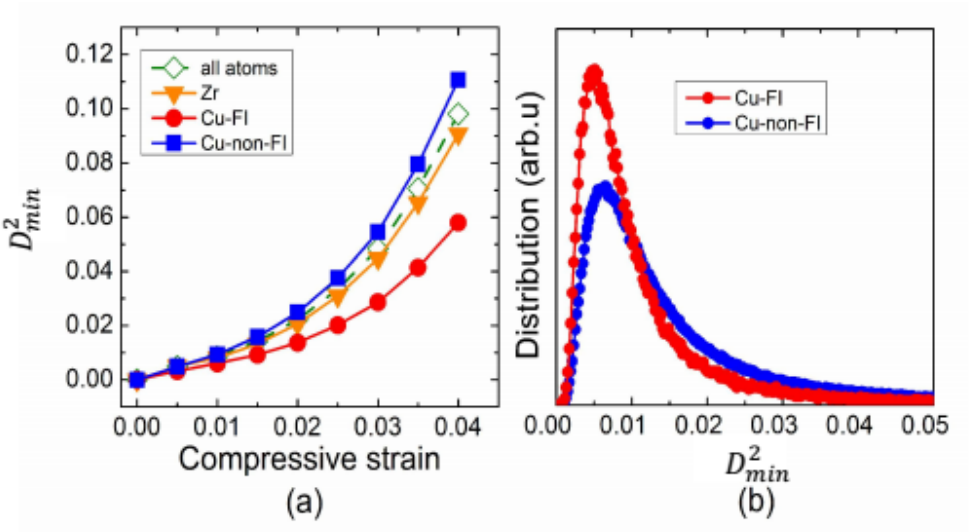

Figure 5-3 (a) Correlation of average non-affine displacement with compressive strain; (b) distribution of non-affine displacement at the imposed compressive strain of 2%. (2)

In order to further investigate the non-affine (heterogeneous) nature of elastic deformation for metallic glasses, here we study the non-affine displacement defined in

Ref (262) that characterize the deviation from affine mapping at current configurations with the reference from initial state. Figure 5-4a presents a vector field of the thin slice at the strain of 2% to show that non-affine displacement of all atoms. The vectors of blue, red and green color represent the atoms of Zr, non-icosahderal Cu and icosahedral Cu, respectively. Even though the amount of those three kinds need to be considered, it can be qualitatively observed that the Cu atoms centered within FI clusters are incline to avoid participation in those "hot" sites. To quantitatively compare those Cu atoms with different local structure, their distribution of non-affine displacement at imposed strain of 2% are normalized and presented in Figure 5-4b. Obviously, it is consistent of our previous observation in Figure 5-4a that the non-affine displacements of FI-centered Cu atoms have smaller mean value and narrower distribution.

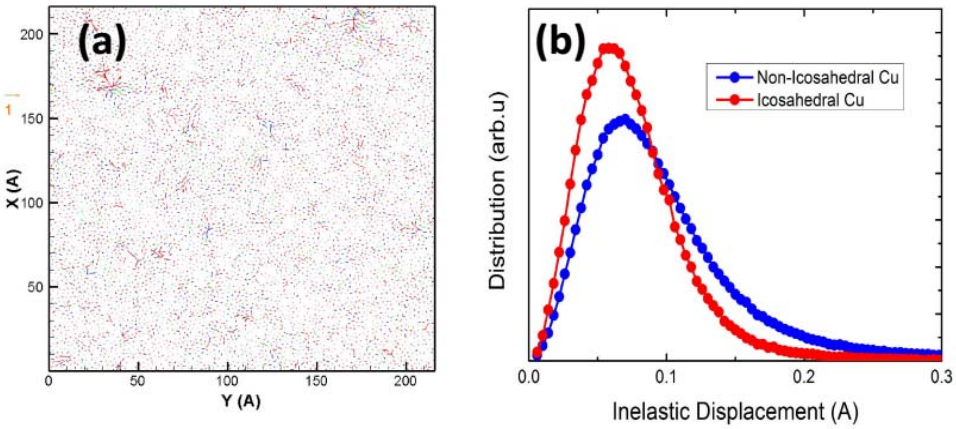

Figure 5-4. (a) A slice of non-affine displacement at the strain of 2% with the thickness of 2.7 Å. Blue vectors represent the ones of Zr atoms, red vectors for that of non-FI Cu atoms and green vectors for FI (<0 0 12 0>) Cu atoms. (b) Distribution of non-affine displacement for FI-centered Cu atoms and non-FI centered Cu atoms at the strain of 2%.

Non-hydrostatic deformation induces structural anisotropy in the MG (4, 78, 100, 112, 263-268), and the dependence of such anisotropy on local environment may provide additional information on how local structure influences its response to applied stresses. Expanding the pair distribution function (PDF) (see Section 1.2.2.1) with spherical harmonics, $g(r) = \sum_{l,m} g_l^m(r) Y_l^m(\hat{r})$ where $\hat{r} = r / \vec{r}$, the anisotropic pair distribution function (78, 263) can be obtained. The anisotropy terms higher than *l*=2 can be neglected. For the *l*=0 case, the structure factor and PDF are for the isotropic state. Thus the anisotropy term is only for *l*=2 and *m*=0 in our loading condition (see Ref. (78) for more details).

Figure 5-5 plots the isotropic and anisotropic PDF for Cu atoms at the compressive strain of 2%. Due to this small applied strain (2%), the isotropic PDF $g_0^0(r)$ of the current configuration in Figure 5-5a only deviates slightly from that of the zero-strain sample. In experiment, the shift of the first peak in isotropic PDF can be used to measure elastic strain (108-110). For $g_0^0(r)$ of Cu atoms, we compare it with $g_0^0(r)$ of Cu-FI and Cu-non-FI. The first peak is split, corresponding to Cu-Cu and Cu-Zr, respectively (the distributions of Cu-Cu and Cu-Zr are so narrow at the simulation temperature of 10 K that this splitting becomes apparent). For the icosahedral Cu atoms, its first peak is sharper and higher, while its first minimum almost reaches zero. This means that the first shell of Cu-FI is well defined and relatively ordered. The second peak and second minimum in isotropic PDF for Cu-FI are also clearer than those for Cu-non-FI. In a previous study (269, 270), the second peak in PDF is regarded as an indication

how the SRO clusters interact with each other. Thus the medium-range structure around the Cu-FI is also expected to be more clearly defined.

For the anisotropic PDF, $g_2^0(r)$ of Cu-FI and Cu-non-FI is presented in Figure 5-5b with reference to the affine (homogeneous) deformation. All of them match very well beyond the distance of 6.5 Å, while there is clear difference between those two curves at below 6.5 Å. As discussed by Dmowski *et al*. (112), this deviation could be attributed to anelastic deformation. In our simulation, it can be clearly observed that $g_2^0(r)$ of Cu-FI is very close to that of homogeneous deformation below the distance of 6.5 Å, while $g_2^0(r)$ of Cu-non-FI suggests significant anelastic deformation. Thus we can conclude that the Cu-FI act more solid-like while the Cu-non-FI are more liquid-like; the latter experiences more atomic relaxation on the timescale of our simulation.

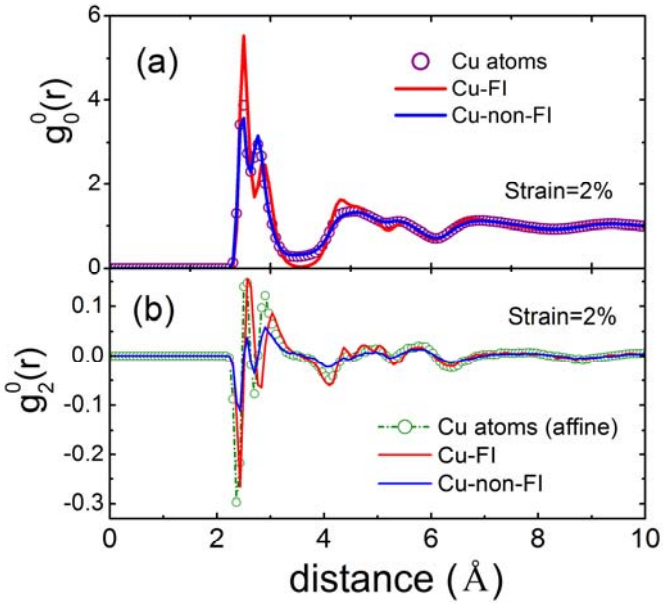

Figure 5-5. Isotropic and anisotropic pair distribution functions of Cu atoms (all Cu, Cu-FI, and Cu-non-FI), at an imposed compressive strain of 2%. (2)

Of course, anelasticity seen in MD would not be exactly the same as that in laboratory experiments, considering the vastly different time scales in sample preparation and deformation. However, the general conclusions of this work, i.e., the correlations found here between deformation-induced anisotropy (271) and local structural order, as well as the roles of the solid-like (FI) and relatively more liquid-like (non-FI) in the anelastic deformation, are insights that shed light on the underlying mechanism of the elastic heterogeneity in laboratory-made MGs. Previous investigations (272) at large strains in plastic deformation have concluded that unstable local structures with large free-volume and more liquid-like sites have higher tendency for shear transformations, whereas the solid-like icosahedral environments are more resistant to plastic flow. Here we see that the same trend is true for deformation in the elastic regime. Also, the composition-dependence of the MD-simulated and experimentally measured elastic constants of CuZr glasses was correlated earlier with the composition-dependence of the fraction of icosahedral clusters. The focus here, instead, is to demonstrate directly and at atomic level that the atomic strain obtained in the elastic regime (assumed to be mostly elastic strains) correlates with the local topology, using a methodical analysis including the isotropic and anisotropic PDFs.

We also caution that in many MGs full icosahedra would not be the dominant and property-controlling SRO as in this Cu-rich MG (6, 18). In those cases additional work would be needed to correlate the relevant local structural features with the elastic heterogeneity. We finally note that elasticity in MGs is not controlled by short-range structures alone; correlations extending to larger length scales also make a difference, as

the applied stress creates a long-range strain field. In the above we have linked the elasticity with only the short-range atomic packing topology. But this correlation is augmented by the known structural developments at longer lengths: for example (6, 175, 184, 185), in a Cu-Zr MG more populous icosahedral SRO clusters would tend to interconnect to form strings (and branches or patches) with medium-range (or even longer range) correlations. Also, the structure-deformation relationship discussed here is only meaningful statistically, and not meant to be an everywhere-valid one-to-one correspondence between a particular type of local environment and elastic response.

5.2. Quantitative measure of local solidity/liquidity in metallic glasses

We first note that when a local region in a metallic glass is deformed, the total strain can be decomposed into an elastic component and a plastic component (2, 4). Upon loading to a constant total strain, the smaller the plastic component, and the larger the elastic component, the more solid-like the local region is. Therefore, the residual elastic strain normalized by the total strain can be regarded as an indicator of solidity. The methodology presented in this work analyzes the degree of solidity/liquidity from this perspective.

In this section, we will propose a method based on bond orientation and cluster anisotropy (4, 128, 266). We will demonstrate our method using MD simulations of a series of binary Cu-Zr MGs. Our quantitative analysis has produced several interesting results. i) The stress sustained by the metallic glass increases linearly with the overall

anisotropy. ii) The capacity to sustain applied shear stress relative to an "ideal elasticity" without relaxations thus offers a useful measure of the degree of “solid-like” behavior. iii) This relative stress-carrying capability is then quantified as the solidity index, and this coefficient decreases for less relaxed states, higher temperatures and shear softening. iv) The spectrum of local solidity index correlates with different local structural environments in a metallic glass.

5.2.1. Calculation of structural anisotropy and solidity/liquidity in metallic glasses

Structural anisotropy of a metallic glass, detected by X-ray diffraction, can be described as bond orientational anisotropy (BOA) (78, 100, 112, 263). However, the BOA, a function of distance, is intrinsically correlated with the gradient of radial distribution ($d[g(r)]/dr$) and thus difficult to be utilized as a universal parameter to characterize various materials. Another candidate, structural anisotropy index, α, which stems from fabric tensor that characterizes an anisotropic texture of the medium, was originally introduced to study the plasticity-induced structural anisotropy in silica glass (266) and then applied to Cu-Zr metallic glasses (4, 128, 268). It worked very well in silica glass because of the well-defined nearest neighbors, but for metallic glasses the scenario is more complicated. Specifically, in an isotropic metallic glass, the distance cutoff in the pair distribution function (PDF), usually taken as the minimum after the first peak (18), and the Voronoi tessellation (18) (see discussion in Section 1.2.2.4), are the criteria often employed to define "nearest neighbors" (atomic bonds). But these two

methods based on isotropic assumption cannot be directly applied to a strained metallic glass when it is deformed and becomes anisotropic.

To overcome this problem, in a deformed metallic glass we define the nearest neighbors by finding the zero flux surfaces in the three-dimensional (3D) bond-density distribution calculated on a fine grid with mesh size $\leq$ 0.1 Å (transformed from Gaussian smearing). In other words, atoms within the volume enclosed by the zero flux surface are considered nearest neighbors (4, 128) (similar to the Bader method used to analyze electron density distribution (227, 228)). Figure 5-6 schematically explains the procedure to construct the anisotropic nearest neighbors, using a glass sample under simple shear in y-z direction at the shear strain of 3%: i) A 2D slice with distribution of bond density is displayed in Figure 5-6a, with the dashed circle marking the zero-flux surface between the first and second shells. ii) To extend this construction into 3D space, the volume enclosed within that zero-flux surface is shown in Figure 5-6b. After finding the nearest neighbors, the anisotropic index α can then be calculated to evaluate the extent of bond orientation (or structural anisotropy). Taking the definition in Ref. (266), the fabric tensor $F = \langle n \otimes n \rangle$ has three eigenvalues, λ_i (1<i<3), then $\alpha = \frac{3}{\sqrt{6}} \sqrt{\sum_{i=1}^{3} (\lambda_i - \frac{1}{3})^2}$. For the isotropic case, α =0, while full anisotropy corresponds to α =1. This parameter can characterize the structural anisotropy quantitatively, with higher value indicating greater anisotropy. We then define the solidity index as

$$\Phi = \frac{\alpha(\gamma)}{\alpha_{affine}(\bar{\gamma})}, \tag{5-3}$$

where $\alpha_{affine}(\bar{\gamma})$ is the anisotropic index for affine deformation at the atomic strain of $\bar{\gamma}$, and it has been calculated below for small strains under simple shear.

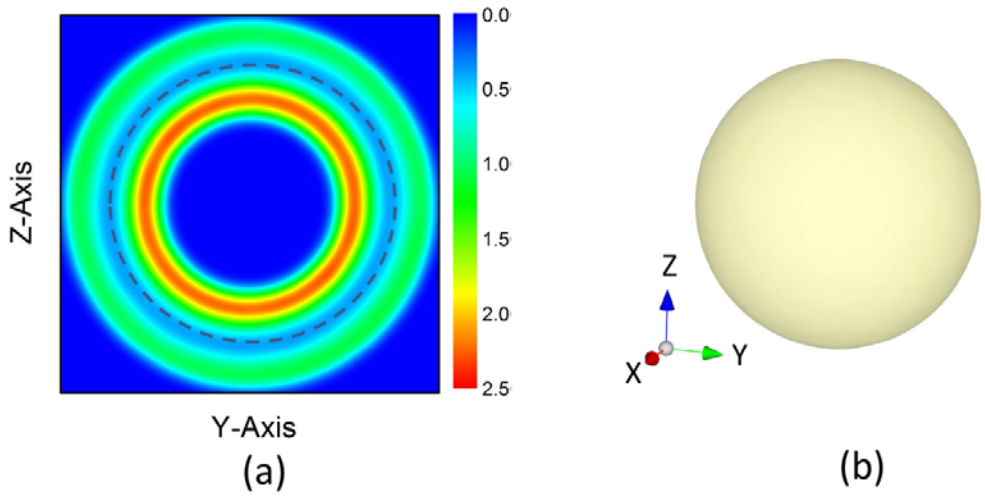

Figure 5-6. At the shear strain of 3% in yz direction, (a) 2-D slice of bond density around all atoms at X=0. The dashed circle marks the iso-surface with minimum density. (b) Bond density in 3-D space enclosed by the zero-flux surfaces between the first and second shells. (4)

When a bond represented by a vector $\vec{n} = \begin{pmatrix} r\sin\phi\cos\theta \\ r\sin\phi\sin\theta \\ r\cos\phi \end{pmatrix}$ (r, ϕ, θ are the radial distance, polar angle and azimuthal angle in spherical coordinate system, respectively) is under simple shear with shear strain γ in *yz* direction (i.e., the transformation matrix is $\begin{pmatrix} 1 & 0 & 0 \\ 0 & 1 & \gamma \\ 0 & 0 & 1 \end{pmatrix}$), the vector after transformation can be expressed as:

$$\vec{n}^* = \begin{pmatrix} 1 & 0 & 0 \\ 0 & 1 & \gamma \\ 0 & 0 & 1 \end{pmatrix} \begin{pmatrix} r\sin\phi\cos\theta \\ r\sin\phi\sin\theta \\ r\cos\phi \end{pmatrix} = r \begin{pmatrix} \sin\phi\cos\theta \\ \sin\phi\sin\theta + \gamma\cos\phi \\ \cos\phi \end{pmatrix} . \tag{5-4}$$

Upon normalization the vector has the form:

$$\vec{n}_u{}^* = \begin{pmatrix} n_x^* \\ n_y^* \\ n_z^* \end{pmatrix} = \frac{r}{\bar{R}} \begin{pmatrix} \sin\phi\cos\theta \\ \sin\phi\sin\theta + \gamma\cos\phi \\ \cos\phi \end{pmatrix} , \tag{5-5}$$

$$\bar{R} = r \bullet \sqrt{\left[(\sin\phi\cos\theta)^2 + \left(\sin\phi\sin\theta + \gamma\cos\phi\right)^2 + (\cos\phi)^2 \right]} .$$

In order to calculate the anisotropy index due to this simple shear strain, we set the initial configuration as a unit sphere which is perfectly isotropic in Figure 5-7a. After the simple shear strain, the fabric tensor can be obtained, i.e., $F = \left\langle \vec{n}_u^* \otimes \vec{n}_u^* \right\rangle$, where < > represents the spatial average, and $\vec{n}_u^*$ is any unit vector on the sphere after the strain transformation (Eq. 5-5). *F* can be calculated as:

$$F = \begin{pmatrix} F_{xx} & F_{xy} & F_{xz} \\ F_{yx} & F_{yy} & F_{yz} \\ F_{zx} & F_{zy} & F_{zz} \end{pmatrix} , \tag{5-6}$$

where $F_{mn} = \frac{1}{4\pi} \int_{\phi=0}^{\pi} \int_{\theta=0}^{2\pi} (n_m^* \cdot n_n^* \cdot \sin\phi) d\phi d\theta$; $(m,n \in [x,y,z])$. (5-7)

The fabric tensor *F* is a function of the shear strain γ , and *F* can be solved numerically by randomly selecting unit vectors on the sphere following uniform distribution, using the algorithm developed by Marsaglia (273). Specifically, x_1 and x_2 are

first selected following uniform distribution on [-1,1], and combinations with $x_1^2 + x_2^2 > 1$ are rejected. From the accepted points,

$$x = 2x_1\sqrt{1 - x_1^2 - x_2^2}$$

$$y = 2x_2\sqrt{1 - x_1^2 - x_2^2} \tag{5-8}$$

$$z = 1 - 2(x_1^2 + x_2^2)$$

would have a uniform distribution on the surface of a unit sphere. Then the fabric tensor can be expressed as:

$$F = \left\langle \vec{n}^*_{unit} \otimes \vec{n}^*_{unit} \right\rangle = \frac{1}{N} \sum_i (\vec{n}^*_{i,u} \otimes \vec{n}^*_{i,u}), \tag{5-9}$$

where *i* is the *i*th bond and *N* is the total number of bonds. Then the anisotropic index can be calculated numerically following the definition in Ref. (266). The *N* in our calculation is chosen to be 10^9 in order to obtain converged and accurate results, and the solved $\alpha - \gamma$ relationship is shown in Figure 5-7b. Linear fitting yields $\alpha \approx 0.346\gamma$. Their correlations for other deformation modes, such as uni-axial tension/compression, bending, etc., can also be obtained using similar derivations.

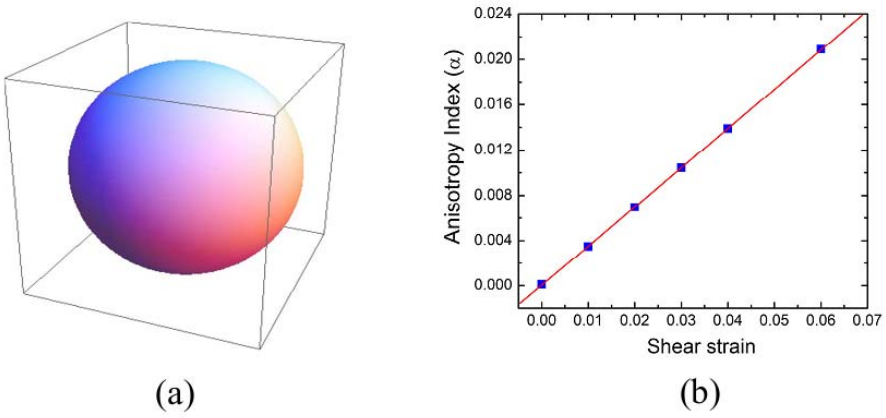

(a) (b)

Figure 5-7 (a). Schematic plot of the surface of a unit sphere. (b) The calculated anisotropic index under simple shear strain for a unit sphere (average of 10^9 points on the sphere) (4)

5.2.2. Model systems

To illustrate how this method works, here we present a case study using MD simulation of a $Cu_{64}Zr_{36}$ metallic glass model containing 1.25 million atoms (with the interatomic interaction described by optimized EAM potentials (6, 174)). Sample 1 (S1) and Sample 2 (S2) were equilibrated for 100 ps at 2500K, followed by quenching to 100 K at 10^{11} K/s and 10^{13} K/s, respectively. The size for S1 at 300K is about 27.1 nm × 27.1 nm × 27.1 nm. For S1, several cases under different conditions were studied, including adiabatic quasi-static shear (AQS) (274) and simple shear at 100 K, shear at 300 K and 500 K with a strain rate of 10^8 /s, and simple shear at a higher strain rate (10^{10} /s) at 300 K. For S2, only AQS was applied.

5.2.3. Correlation of sustained shear stress with anisotropy index

The crucial step to calculate anisotropy index (α) in metallic glasses is to define the bonds (nearest neighbor atoms) in an anisotropic sample. We have introduced a new method and its results for affine deformation are shown in Figure 5-8, where the data fit very well with theoretical prediction $\alpha \approx 0.346\gamma$. To highlight the advantage of our method, here we also compare it with those from two other commonly-used means that define nearest neighbors in metallic glasses: Voronoi tessellation (with VORO++(257, 258)) and distance cutoff (usually located at the first minimum in the PDF). The results based on those three different schemes for the affine deformation under simple shear are shown in Figure 5-8. Under affine deformation, the anisotropy index for each group is expected to follow $\alpha \approx 0.346\gamma$, which has been derived above in Section 5.2.2. However, in Figure 5-8, only the anisotropy indices by our newly introduced method are all consistent with the theoretical prediction, while the results from the other two methods exhibit a wide range of deviation (only the α of Cu-centered full icosahedra (Cu-FI) via those two methods falls on the linear scaling relationship $\alpha \approx 0.346\gamma$). This result confirms the validity and advantage of our method by introducing the zero-flux surface to define "bonding" or nearest neighbors in anisotropic metallic glasses. For the other two methods (Voronoi tessellation and distance cutoff), while they are in general not suitable to define α, it appears that the α of Cu-FI derived from those two methods is consistent with the theoretical prediction. This is presumably because the atomic volume of Cu-FI usually lies in the middle of atomic volume distribution of all Cu atoms (5) and thus approximately represents the average atomic volume.

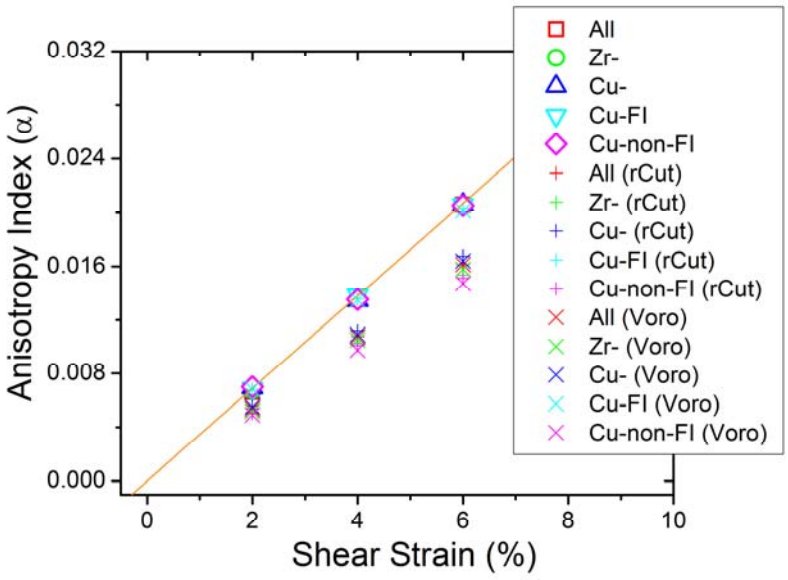

Figure 5-8. Anisotropic index for the affine deformation under simple shear via three different calculation schemes: zero-flux surface, Voronoi tessellation and distance cutoff. (4)

The stress-strain curves of the sheared models are presented in Figure 5-9a, in comparison with the affine deformation of sample S1 at 0 K (i.e., without relaxation). For those different loading conditions, either localized shear banding (for example in S1 at the AQS limit, as shown in the inset of Figure 5-9a) or distributed deformation (e.g., in S1 at 500K) were observed. The stress-strain curves in Figure 5-9a confirm that lower temperature and higher strain rate lead to higher stress, and vice versa. This is consistent with the typical behavior of viscoelastic materials.

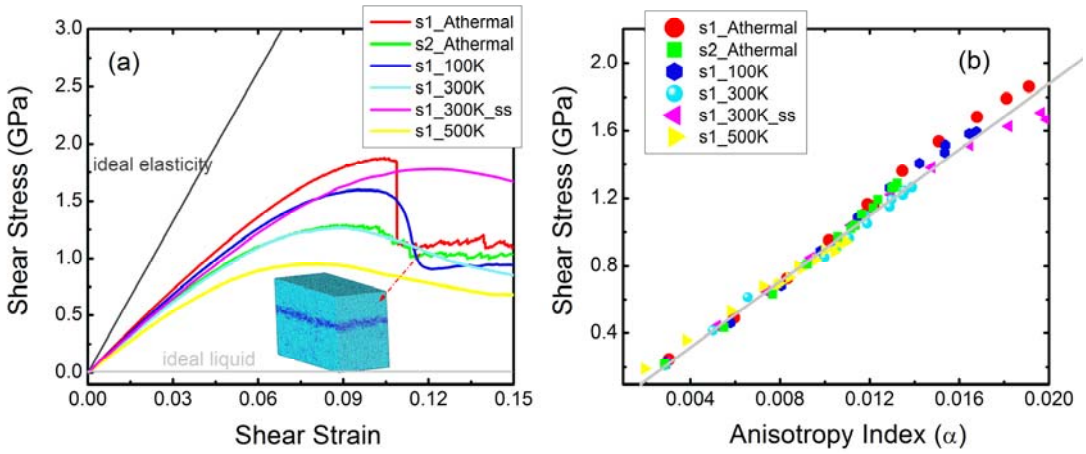

Figure 5-9. (a) Stress-strain curves of $Cu_{64}Zr_{36}$ metallic glasses under AQS, 100 K, 300 K and 500 K, respectively, with the strain rate of 10^8 /s and 10^{10} /s (marked as *ss*). Inset shows Sample 1 at the strain of 10% at the AQS limit, following the color scheme of local shear invariants (259). (b) Correlation of shear stress with anisotropy index for different loading conditions. (4)

To study the correlation between α and stress, we calculate the anisotropy index at various strains for each of the samples (from 1% to 15%, with a strain step of 1%), and plot α as a function of the corresponding shear stress in Figure 5-9b. All those anisotropic indices were obtained on a 3D grid with a mesh size of 0.1 Å. The results in Figure 5-9b clearly demonstrate an almost linear relationship between α and the shear stress τ, with the expression of $\tau \approx 92.5\alpha$, which explains the resemblance between the curves of α and shear stress as a function of strain (see Figure 5-11 below; also observed in deformation of silica glass (266)). This confirms that the shear stress on

materials linearly scales with the bond orientation anisotropy, regardless of the structural state and loading conditions. In fact, this anisotropy is the atomic-level origin of the shear stress. For ideal liquids, the structure is always isotropic due to the full relaxation, thus they cannot sustain shear stress (i.e., they have no shear resistance). In contrast, the ideal elastic solids exhibit the highest anisotropy upon deformation (with no relaxation), meaning that each and every part of the material responds fully elastically. Viscoelastic materials, such as metallic glasses, lie in between ideal elastic solids and ideal liquids (Figure 5-9a), with solid-like local regions contributing more to the shear stress (serving as the elastic backbone), and liquid-like local regions preferentially yielding and relaxing (serving as the carriers of the anelastic deformation). This is consistent with our idea that the bond orientation anisotropy can be used as a tell-tale indicator for the solidity/liquidity (see quantitative discussions in Section 5.2.4).

5.2.4. Averaged and local solidity/liquidity: quantitative trends

For an ideal liquid with vanishing viscosity, the structure can always relax to the stress-free isotropic state at an infinitely fast rate, thus its solidity index (Φ in Eq. (5-3)) is zero, whereas for ideal elasticity without relaxation, Φ would be 1. Since metallic glasses are viscoelastic in nature, consisting of solid-like and liquid-like regions, the Φ of these local regions would be between 0 and 1.

The evolution of Φ with shear strain for various samples is shown in Figure 5-10, and the solidity for as-quenched sample can be estimated by extrapolation. The maximum shear strain of 8% in Figure 5-10 is below the yielding strain of the simulated samples, before the onset of plastic flow of the overall sample. For the sample with slower

quenching rate, its solidity index can be as high as 0.9 in the AQS limit. However, Φis as low as 0.4 in S1 loaded at 500K. With increasing shear strain, the Φ decreases monotonically. This can be explained by the anelastic deformation that is increasingly activated at higher and higher stresses, even though our samples are in the nominally elastic regime (112). Specifically, the localized shear transformation contributing to the anelastic deformation is responsible for the structural relaxation (275), as well as for the reduced shear stress and anisotropy. This connection of bond orientation and stress, specifically the shear-induced softening, is consistent with the correlation illustrated in Figure 5-10.

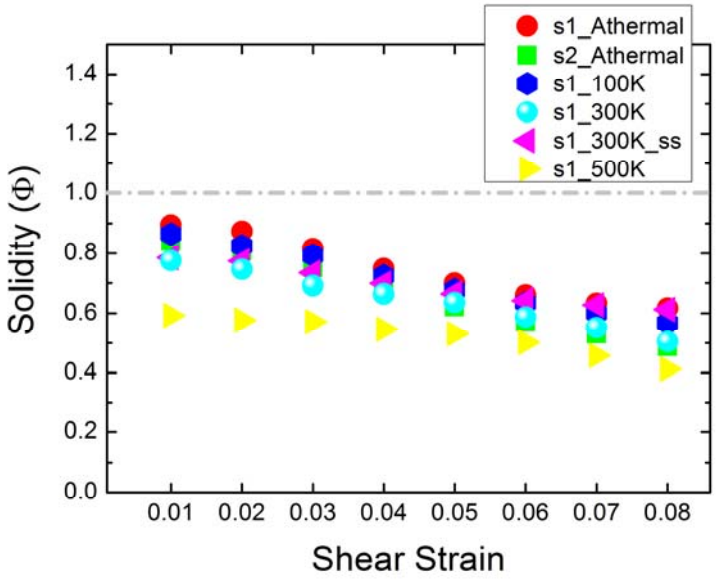

Figure 5-10. Solidity coefficient versus shear strain under different sample/loading conditions. (4)

After comparing the solidity/liquidity averaged over all atoms, we now analyze the correlation between local structure and local solidity/liquidity. As studied in Ref. (2), the

atomic strain in metallic glasses is inhomogeneous, and depends on the local structure; thus for each type of local structural configuration/motif, we will use its average strain for normalization. In Figure 5-11a the anisotropy index (α) for Zr atoms, Cu atoms in the center of Cu-FI, and Cu atoms in the center of non-icosahedral clusters (Cu-non-FI) are displayed for the S1 sample (sheared at 300K with the strain rate of 10^8 /s), in comparison with the value for affine deformation. Not surprisingly, the α for affine deformation almost overlaps with the fitting of $\alpha_{affine}(\gamma) \approx 0.346\gamma$. This result differs from that given by structural anisotropy analysis based on distance cutoff or Voronoi tessellation, which have been compared in Section 5.2.1. This illustrates that our method is advantageous over previous ones. Comparing the α of Cu-FI and Cu-non-FI, the former has higher bond orientation anisotropy than the latter, not only in the elastic regime but also during plastic flow.

In addition to the bond orientation, we can also calculate and compare $\sigma_{ij}\times\Omega_m$ (60) for each atom, where σ_{ij} is defined as the stress on this atom, and Ω_m is the atomic volume. Since Ω_m is not unambiguously defined in metallic glasses, we decide to use $\sigma_{ij}\times\Omega_m$ to represent the atomic stress in our analysis below. In Figure 5-11b, we plot the $\sigma_{yz}\times\Omega_m$ averaged over all atoms, Zr, Cu-FI and Cu-non-FI, respectively. We observe that $\sigma_{yz}\times\Omega_m$ for Cu-FI is about 1.8 times that for Cu-non-FI. Such a sizable gap leads to the conclusion that the Cu-centered FIs are under much higher stress than the other Cu atoms, and hence confirms the role of FI as the local topology with the highest solidity in Cu-Zr metallic glasses.

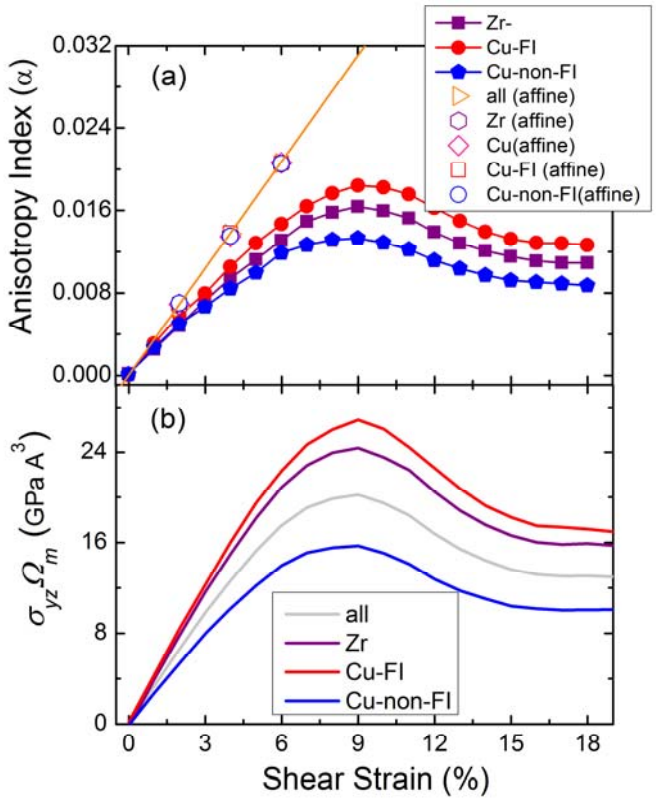

Figure 5-11. Cu_{64} Zr_{36} metallic glasses (S1) with the shear strain rate of 10^8 /s at 300K (a) Evolution of structural anisotropy index with increasing strain. (b) Plot of $\sigma_{ij}\times\Omega_m$ vs shear strain. (4)

For more detailed analysis, a finer grid with mesh size 0.052 Å is used in order to obtain higher accuracy. For the S1 sample under the shear strain rate of 10^8 /s at 300K, their solidity spectra in terms of different Voronoi polyhedra types are shown in Figure 5-12a at the shear strain of 6%. For Cu atoms, the five most populous polyhedra have Voronoi indices <0,0,12,0>, <0,2,8,2>, <0,2,8,1>, < 0,2,8,0>, and <0,3,6,3>. The rest Cu-centered polyhdera are grouped together as "others". As discussed before (6, 18), Zr-centered clusters are more diverse in terms of Voronoi index and the five most populous

popolyhedra are <0,0,12,4>, <0,0,12,3>, <0,1,10,5>, <0,1,10,4>, and <0,2,8,6>. All the polyhedra listed above for Cu and Zr are Kasper polyhdedra and distorted ones (18). For Cu, solidity is obviously different for different types of clusters: full icosahedra are the most solid-like and their average solidity index is about 1.6 times that for the “others”. As an example, at the shear strain of 1%, the calculated Φ for <0, 0, 12, 0> is 0.88 and that for the "others" is about 0.66. These values are both greater than those at the shear strain of 6%, but upon the increase of shear strain the former for <0, 0, 12, 0> drops much less than the latter for the “others”. In comparison, there are no dominant Zr-centered polyhedra in terms of the solidity index or the Voronoi index (Zr-centered Z-16 Kasper polyhedra becomes pronounced. It is worth noting that the larger Zr atoms deform in a more solid-like manner than most Cu atoms except for the full icosahedral ones. Besides, the solidity index values for each group via *affine* deformation (without relaxation) are also marked in Figure 5-12a. As expected, they are all close to unity with a standard deviation of 0.0054, confirming that the reduced solidity (to different extent) are due to the different degree of relaxation in different types of clusters. The small standard deviation also reflects the accuracy (error bar) of our calculation.

Figure 5-12b presents the spectra of solidity index based on atomic volume (Voronoi cell volume). For Cu atoms, the first and last columns represent the Cu-centered polyhedra with the volume below 11.95 $Å^3$ and above 13.35 $Å^3$, respectively, and the rest seven lie between them uniformly. For the atomic volume of Zr atoms, the two ends are 21.1 $Å^3$ and 22.9 $Å^3$. For the spectra of solidity index versus atomic volume (Voronoi cell volume), there appears to be a clear trend of reducing solidity with increasing atomic volume for Cu atoms, while there is no such obvious trend in the case of Zr atoms. This

observation is consistent with previous analysis (18) that the dependence on cooling rate for local structure around Zr atoms, such as coordination polyhedra, is weaker than that for Cu atoms.

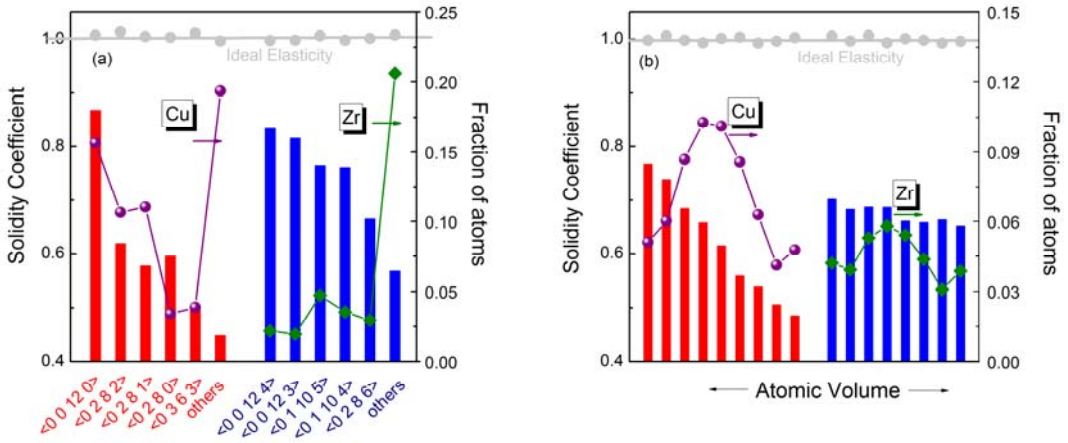

Figure 5-12. Spectra of solidity coefficient based on (a) Voronoi polyhedra and (b) atomic volume (Voronoi cell volume) for both Cu and Zr atoms, at the shear strain of 6%. (4)

We note that a macroscopic solidity index (S) was previously defined as **S** = μ/B, where μ and B are the shear and bulk modulus, respectively (276). Our microscopic index defined here, when averaged throughout the sample, yields consistent results. Specifically, the sample obtained by slower cooling rate has higher average solidity as calculated by the normalized bond orientation anisotropy. As illustrated in Ref. (30, 33, 277), slower cooling rate would increase shear modulus but have negligible effect on bulk modulus, hence a higher **S** is also expected.

The quantitative measure of solidity/liquidity, through Φ, allows one to monitor the evolution of ”solid-like” and “liquid-like” behaviors, from as-prepared glass to partly

rejuvenated amorphous structure. For example, a decreasing trend of solidity with the strain experienced by the glass has been demonstrated. Also, it is known before that non-affine displacements are responsible of overall shear and bulk modulus reductions respective to the values expected for a pure affine deformation (30). The reduced anisotropy in "liquid-like" regions is another way of quantifying the presence of non-affine relaxations in glasses. Moreover, we have dissected the spectrum of solidity as a function of local atomic structure (on average, each type of local motif presents a different local solidity/liquidity index), across the spectrum of various types of motifs (with different topology and atomic volume) present in the glass. The Φ (or α) may also serve as a bridge to connect shear flow in liquid with shear banding in an amorphous solid (128).

5.3. Percolation of ICOI networks: Effects on shear modulus

We now proceed to examine the connection of Cu-FI over further extended ranges. Now we move on to the MGs, where the accumulating FI and their interpenetrating connection form networks (184, 185). The growing ICOI over longer and longer range is likely to establish the backbone (solid-like) structure of an MG. In the following we show that this elevates the shear modulus of the glass, *G*, as a result. We also show that the percolation of such networks marks a turning point in the escalating *G*. This is analogous to the previous observation that the percolation of icosahedra (or quasi-crystal-like) SRO correlates with the plastic localization in a model MG (106, 278).

Isothermal stiffness coefficients (C) at room temperature were evaluated using the fluctuation method (30, 33, 277, 279). For a canonical (NVT) ensemble, C can be calculated as the sum of three contributions (30):

$$C_{ijkl}^{T} = C_{ijkl}^{I} + C_{ijkl}^{II} + C_{ijkl}^{III} \tag{5-10}$$

where the superscript *I, II* and *III* represents the fluctuation, kinetic contribution and the Born term, respectively (see Ref. (30) for more details). To reduce the statistical error in our simulated samples, the average shear modulus (G) was evaluated as

$$G = \frac{C_{44} + C_{55} + C_{66}}{3} . \tag{5-11}$$

G can also be decomposed into three terms corresponding to those in Eq. (2-1). For instance,

$$G^{I} = \frac{C_{44}^{I} + C_{55}^{I} + C_{66}^{I}}{3} . \tag{5-12}$$

To evaluate local elasticity, the simulation box is subdivided into a grid of 90×90×90 following Ref. (277, 280, 281) and the local elastic moduli tensor, C_{ijkl}^{ξ}, at the center of each subcell ξ is computed at the coarse-grained (281) scale using Gaussian with FWHM (full width at half maximum) of 8 Angstroms. The average local elastic modulus tensor would be equal to global elastic tensor (277). Using this approach, the local shear modulus, C_{44}^{ξ}, can be plotted with adequate spatial resolution to reflect its heterogeneous distribution.

The strong configurational dependence of G in MGs has been discussed before (30, 33, 277). MGs produced with slower cooling rate (termed “older” glasses (30) exhibit

higher G than those obtained with faster cooling rate (termed "younger" glasses (30)). Our observation in Figure 5-13 confirms this conclusion, showing that G increases markedly with decreasing cooling rate. The three decomposed components of G are also consistent with previous findings: the Born terms (G^{III}) and kinetic contribution (G^{II}) are almost independent of configurations obtained via different quench rates (only slight changes for G^{III} due to the different densities from the Debye-Grüneisen effect of thermal expansion for an isolated configuration state (32, 33)). On the contrary, the fluctuation term G^{I} is very sensitive to the state of the glass (younger and older) and constitutes almost all of the cooling rate dependence of the total G (30, 277). As discussed in the PEL picture in Ref. (30), while the Born term measures the average of the instantaneous curvature of the PEL basin, the majority of the configurational dependence comes from G^{I}, which is the fluctuation of instantaneous slope of the potential energy surface being sampled.

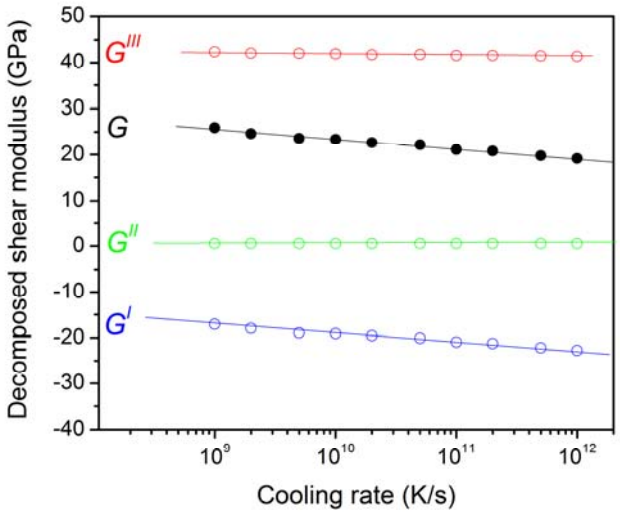

Figure 5-13. The shear modulus (G) and the decomposed components (G^{I}, G^{II} and G^{III}), for $Cu_{64}Zr_{36}$ metallic glasses prepared using different cooling rates. (6)

Figure 5-14 maps out the local shear modulus for a typical slice of the $Cu_{64}Zr_{36}$ MG (cooling rate of 10^9 K/s, thickness of average atomic spacing ~2.5 Å). Apparently, the local shear modulus at our coarse-grained scale is spatially inhomogeneous, and certain regions can be relatively unstable, which is consistent with previous observations (277, 281). The system average is G=25.8 GPa, as indicated by the arrow in the scale bar. Meanwhile, in Figure 5-14, the distribution of ICOI networks (only Cu atoms in the center of icosahedra are displayed) is superimposed onto this map. In general, the local G of the cells where ICOI networks reside is well above the bulk-average. The ICOI networks can therefore be regarded as an indicator of the most solid-like backbone in the glass structure.

To reveal how ICOI networks develop, Figure 5-15 correlates the largest size of the ICOI networks (represented by the number of the center Cu atoms within the FIs in the network), with the fraction of Cu-FIs present in the glass. The data points from left to right correspond to samples produced with faster to slower cooling rate: the "younger" glass contains less FIs and vice versa. The two insets in the figure illustrate the typical ICOI networks in the two corresponding states: the left one shows the four largest ICOI networks (around 100-200 FIs each); the right one contains a very large ICOI network (~5,000 FIs). Apparently, there is no percolated FI network within the former configuration, while for the latter sample the largest ICOI network permeates through the whole box. There is a turning point, a threshold of percolation of ICOI networks, P_c which is marked by the yellow region in Figure 5-15. P_c for our alloy can be approximated as $P_c \approx 26\% * 0.64 = 0.166$. Samples on the left only contain separated

ICOI networks, and they extend to connect through the whole sample on the right of the percolation.

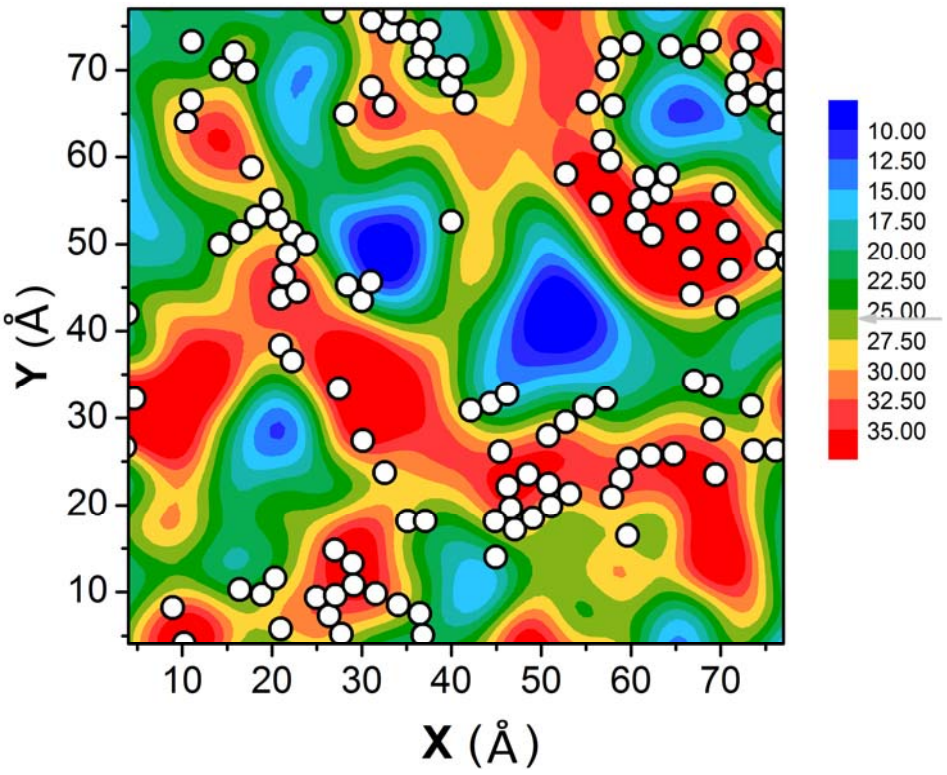

Figure 5-14. The distribution of percolated ICOI networks overlapped with a coarse-grained map of local elastic moduli (C_{44}), within a slice (thickness of 2.5 Å) of $Cu_{64}Zr_{36}$ MG cooled to room temperature at 10^9 K/s. (6)

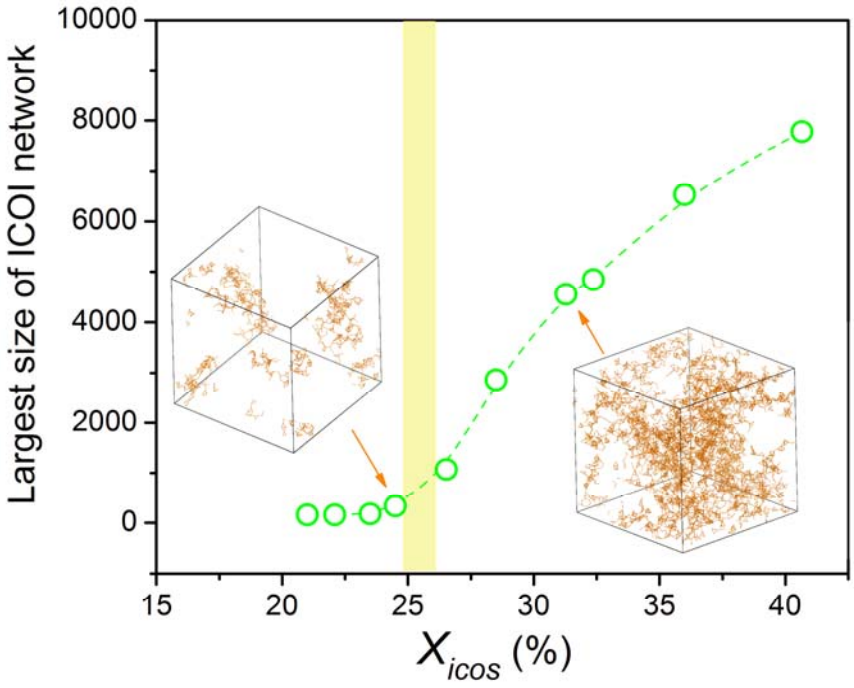

Figure 5-15. Relationship between the largest size of ICOI network and the fraction of Cu-FI in $Cu_{64}Zr_{36}$ MGs. The yellow bar marks the percolation of ICOI networks. The left inset exhibits the four largest (but separated) ICOI networks in the system, while the right inset shows only one ICOI network, a large one made up of many (percolated) smaller networks that extends across the periodic boundaries. (6)

Next, we examine the CPE dependence of the *G* for the $Cu_{64}Zr_{36}$ MG. Previous simulation (33) and experiment results (31, 282) have reported an almost linear relation between the *G* and CPE (lower CPE corresponds to higher *G*). However, we have observed in Figure 5-16a two separate regions of the *G*~CPE scaling: the nearly linear relationship holds for both regimes, but with different slope. Clearly, there exists a

turning point: the slope is about -233 GPa/(eV/atom) on the left but almost doubled (~ -450 GPa/(eV/atom)) on the right. In Figure 5-16a, we observe that this change of slope corresponds to the ICOI network percolation threshold. This can also be viewed from the structural ordering perspective, as there is an almost linear relationship between CPE and fraction of Cu-centered icosahedra, see the inset in Figure 5-16b, which plots the fraction of Cu-centered icosahedra against *G*. *G* increases monotonically with increasing FISRO, corresponding to aging the glass to lower CPE (Figure 5-16b). As expected, we observe again two regions crossing at the P_c. This observation is similar with percolation effect of elastic modulus within composite materials (283, 284).

This indicates that ICOI is a key structural origin of the increasing system *G*, and this increase slows down after the ICOI networks percolate. From the PEL perspective, *G*, and the corresponding energy barrier *W* in Johnson-Samwer's cooperative shear model (31), is sensitively dependent on the configuration. Our finding here highlights the role of the icosahedral networks as the backbone structure, and the sensitivity is especially high if the glass structure only contains unlinked ICOI segments.

Our observation of this turning point underscores the need to sample the glass configurations over a sufficiently wide range. Specifically, the simulation work by Duan et al. only covered rapid cooling rates above 10^{12} K/s (33), and the experimental samples in the laboratory (31, 282) only dealt with well-aged glass configurations. Either one, while each revealing a linear relationship, stays entirely on one side (either left or right) of the P_c in terms of structural development. Our point is that *G* has an explicit FISRO/ICOI dependence, over a wide range of FISRO development but having different

stages before and after ICOI percolation. The backbone role of ICOI networks is thus obvious.

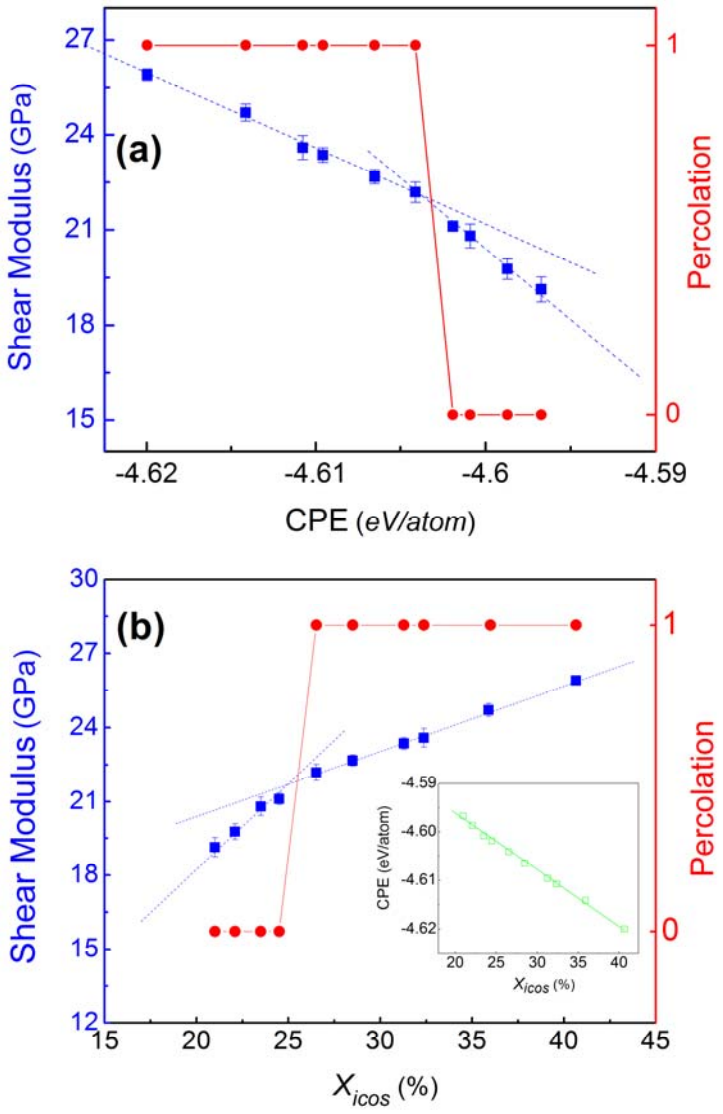

Figure 5-16. (a) Correlation between the shear modulus and the configurational potential energy (CPE) of $Cu_{64}Zr_{36}$ metallic glasses. (b) Correlation between the shear modulus and the fraction of Cu-centered full icosahedra in $Cu_{64}Zr_{36}$ metallic glasses. Inset shows the correlation between the CPE and X_{icos}. (6)

5.4. Conclusions

This chapter has studied the structural origin of elastic heterogeneity in metallic glasses via MD simulation. This study is mainly illustrated on three-fold. One is to correlate deformation-induced anisotropy and local structural order, as well as the roles of the solid-like (FI) and relatively more liquid-like (non-FI) in the anelastic deformation (2). The focus of this work is to demonstrate directly and at atomic level that the atomic strain obtained in the apparently elastic regime correlates with the local topology, using a methodical analysis including the isotropic and anisotropic PDFs. They are insights that shed light on the underlying mechanism of the inhomogeneous elasticity in laboratory-made MGs.

The second goal of this chapter is to introduce a method to quantify relative local solidity/liquidity in metallic glasses from the microscopic origin (4). We have defined a solidity index, Φ, based on bond orientation anisotropy α . The latter was derived using a new scheme to determine nearest neighbors in strained amorphous systems, by plotting the three-dimensional bond density distribution and then finding the zero-flux surface. Interestingly, we discovered a master curve connecting the shear stress and the anisotropy index α , regardless of the structural state and loading conditions. This shows that α and Φindices can characterize how “solid-like” the configuration is for sustaining the shear stress, and could be very useful parameters for the study of intrinsic behavior in metallic glasses.

The third one is to illustrate the formation of spatial connection among full icosahedra short-range order and percolation over longer length-scale, and their impact on various properties such as local shear modulus. The rising shear modulus scales directly with the population of Cu-FI, in particular with ICOI and its spatial distribution, exhibiting a slope change when the ICOI networks percolate (6).

Chapter 6

Low-frequency vibrational modes, soft spots and their structural signature in metallic glasses†

As already discussed the structural signature of thermodynamic, kinetic and mechanical properties in metallic glasses, we focus on their vibrational properties (as discussed in Section 1.3.3), especially low-frequency vibrational normal modes and following identified soft spots, then relate with corresponding atomic packing structure (7). Specifically, in a three-dimensional model mimicking realistic $Cu_{64}Zr_{36}$ metallic glass, we demonstrate that quasi-localized low-frequency vibrational modes correlate strongly with fertile sites for shear transformations. We have also uncovered a direct link between

† Part of the results has been published in Ref.(7)

these soft modes/spots and the local atomic packing structure: geometrically unfavored motifs (GUMs) constitute the most flexible local environments that encourage soft modes and high propensity for shear transformations, while local configurations preferred in this alloy, i.e., the full icosahedra (around Cu) and Z16 Kasper polyhedra (around Zr), contribute the least.

6.1. Introduction of low-frequency vibrational modes in metallic glasses

As discussed in previous chapters, metallic glasses have an inherently inhomogeneous internal structure, with a wide spectrum of atomic-packing heterogeneities (18-21, 66, 285). As a result, an *a priori* identification of structural "defects" that carry atomic rearrangements (strains), under imposed stimuli such as temperature and externally applied stresses, has always been a major challenge (18, 21, 112, 255). In several quasi-2D or 3D models of amorphous solids (such as jammed packings of soft spheres interacting via repulsive potentials or colloidal particles), low-frequency vibrational normal modes have been characterized and it has recently been demonstrated that some of these modes are quasilocalized (160, 161, 164, 286-292). A population of "soft spots" have been identified among them, in terms of their low-energy barriers for local rearrangements (290, 291), correlating also with properties in supercooled liquids such as dynamical heterogeneity (293-295). However, it is not certain where the soft spots are in realistic MGs (160), in terms of an explicit correlation with local atomic packing and topological arrangements (160, 162, 296). In particular, there is a pressing need to determine whether or not it is possible to identify shear transformation zones, i.e., the local "defects" that carry inelastic deformation (104, 117, 118, 120, 121,

297, 298). Accomplishing this would permit the characterization of MG microstructure in a way that directly ties atomic configuration with mechanical response beyond the elastic regime. We will show in this chapter that there is indeed a correlation between soft modes and atoms that undergo shear transformations, and both have their structural signature in specific atomic packing environments defined in terms of coordination polyhedra (18).

6.2. Model systems

Specifically, our molecular dynamics simulations employ embedded atom method (EAM) potentials optimized for realistic amorphous Cu-Zr structures (1, 174), using 10,000 atoms at the $Cu_{64}Zr_{36}$ composition. The MG was prepared by quenching the system at cooling rates between 10^9 K/s and 10^{13} K/s from a liquid state equilibrated at 2,500 K using a Nose-Hoover thermostat (58, 60). The external pressure was held at zero during the quenching process using a Parinello Rahman barostat (60). Periodic boundary conditions (PBCs) were applied in all three dimensions. Structural analysis was implemented using Voronoi tessellation to characterize the nearest-neighbor coordination number (CN) and short-range order (18).

The normal mode analysis of the glass was conducted by diagonalizing the dynamical matrix of the MG inherent structure obtained using the conjugate-gradient (CG) method (60). The dynamical matrix of the inherent structure was defined as $D = (\partial^2 \Phi(r) / \partial r_i^k \partial r_j^k)$, where r_i^k is the kth component of the position $\mathbf{r}_i$ of particle i, $\Phi(r)$ is the Hamiltonian with $\Phi(r) = \sum_{i=0}^{N} \sum_{j=1, j\neq i}^{N} u_{ab}(r_{ij})$, $u_{ab}(r)$ is the intermolecular potential and

$r_{ij} = |r_i - r_j|$. The participation fraction of particle i in eigenmode $\mathbf{e}_\omega$ is defined by $p_i = \left|\vec{e}_\omega^{\,i}\right|^2$, where $\vec{e}_\omega^{\,i}$ is the corresponding polarization vector (294). The phonon calculation was obtained with the software of General Utility Lattice Program (GULP) with certain modifications (http://projects.ivec.org/gulp/) (299, 300). Similar to Ref. (294), p_i was summed over a small fraction (1%) of the lowest-frequency normal modes and denoted as the participation fraction $\mathbf{P}_i$ for the ith atom, which measures the involvement in soft modes for that atom. The chosen fraction of lowest frequency is between the previously used cut-offs of 0.6% (291) and 1.5% (294); only slight variation was found when the cut-off criterion was varied over this range)

6.3. Low-frequency vibrational modes in $Cu_{64}Zr_{36}$ MGs

Figure 6-1 displays the vibrational density of states (V-DOS), $D(\omega)$ of the $Cu_{64}Zr_{36}$MG prepared with the cooling rate of 10^9 K/s, calculated from the eigen-frequencies obtained by normal mode analysis. The blue portion in Figure 6-1 indicates the 1% lowest frequency normal modes, which will be summed over in our calculations of the participation fraction, $\mathbf{P}_i$, in soft modes. Those low-frequency vibrational modes are confirmed to be quasilocalized, similar to previous work on simple models (see Ref. (160, 162, 292, 294)), as they involve a compact group of atoms, on the basis of the amplitude distribution of their corresponding eigenvectors.

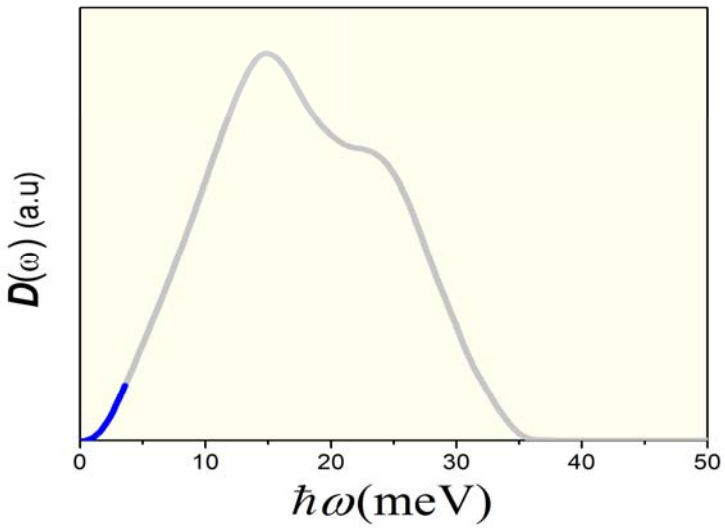

Figure 6-1. Vibrational density of states (V-DOS) of the inherent structure for $Cu_{64}Zr_{36}$ metallic glass produced with the cooling rate of 10^9 K/s. The blue portion indicates the 1% lowest frequency normal modes that were summed over to calculate the participation fraction (in soft modes) of atoms. (7)

Figure 6-2 displays the vibrational density of states (V-DOS), $D(\omega)$, of the $Cu_{64}Zr_{36}$MG prepared with the cooling rates from 10^9 K/s to 10^{13} K/s. The main peak stays around 14 meV and becomes only slightly narrower (or wider), when the cooling rate used to prepare the MG is slower (or faster) as seen in the Figure 6-2 (7); the glasses cooled at slower rates exhibit fewer low-frequency (or low-energy) vibrational modes. Note that MGs with different cooling rate render different state of configurations, as illustrated by potential energy landscape (PEL) (23, 31, 127). And $Cu_{64}Zr_{36}$MGs with various cooling rate have been investigated to exhibit different fraction of full icosahedra short-range-order (FISRO) as well as distorted polyhedra coordination(6, 18) , which will

be studied below to account for contrasting participation fraction in low-frequency vibrational normal modes.

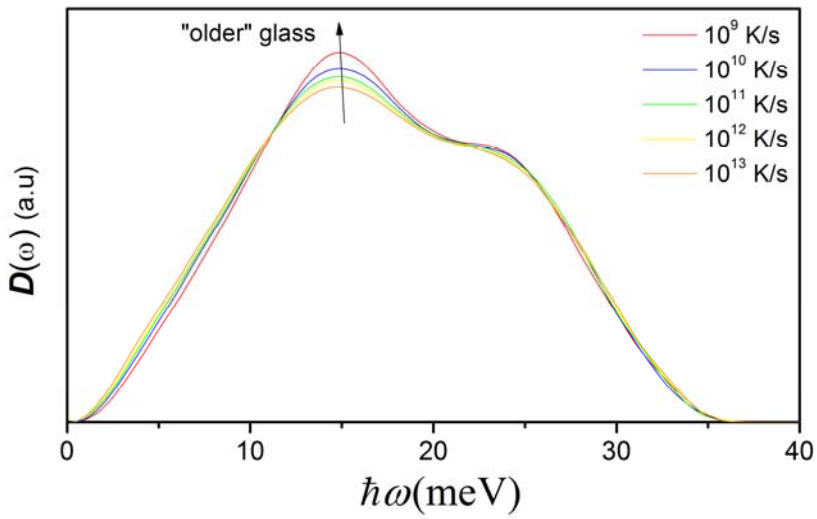

Figure 6-2. Vibrational density of states (V-DOS) for $Cu_{64}Zr_{36}$ metallic glasses quenched with the cooling rates from 10^9 to 10^{13} K/s. (7)

6.4. Relationship between local structure and low-frequency vibrational modes

We first demonstrate that certain types of coordination polyhedra, specifically those geometrically unfavored motifs (GUMs), contribute preferentially to the quasilocalized soft modes identified above, while the geometrically preferable clusters at this alloy composition represent the short-range order that participate the least. To establish the connection between the low-frequency modes and atomic packing structure, we analyze

the latter first from the perspective of Cu-centered coordination polyhedra (6), in terms of the $\mathbf{P}_i$ of Cu atoms that are in the center of different types of polyhedra. In Figure 6-3a, from left to right each solid bar represents a bin that contains 10% of all the Cu atoms, in ascending order from the lowest to the highest $\mathbf{P}_i$. In addition, the 1% Cu atoms with the lowest $\mathbf{P}_i$ and the top 1% with the highest $\mathbf{P}_i$ are displayed on either end, each with a separate bar. The Cu atoms in full icosahedra (with Voronoi index <0, 0, 12, 0>) dominate the lowest $\mathbf{P}_i$, which is consistent with the notion that full icosahedra are the short-range order least likely to participate in soft spots at this MG composition (6). Specifically, ~98% of the Cu atoms with the 1% lowest participation fraction are enclosed in <0, 0, 12, 0>, much greater than the average value that ~40% of Cu atoms center full icosahedra in this MG sample (6). In stark contrast, the local configurations on the other end of the coordination polyhedra spectrum, i.e., the geometrically unfavorable motifs (see examples below) that deviate considerably from the CN=12 full icosahedra and their close cousins (see legends in Figure 6-3), are not found at all amongst the atoms with the lowest 1% participation fraction. For the 1% of Cu atoms with the highest participation fraction, GUMs account for as high as 63% while the share of full icosahedra is as low as only 1.1%. This observation clearly indicates that atoms involved with soft spots in low-frequency normal modes (i.e., soft modes) are those with the most unfavorable local coordination polyhedra.

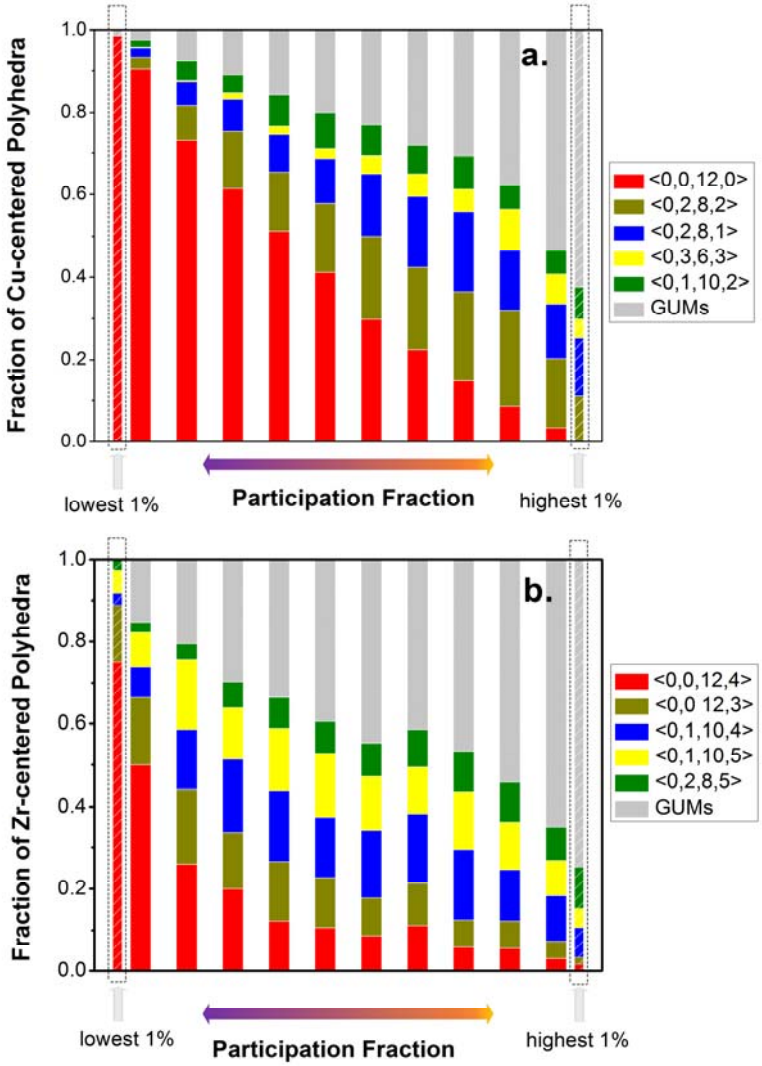

Figure 6-3. Atoms at the center of different types of (a) Cu-centered and (b) Zr-centered coordination polyhedra contribute differently to low-frequency normal modes. Each solid bar contains 10% of all the Cu (or Zr) atoms; from left to right, the bins are ordered from the lowest to the highest participation fraction. Two additional bars describe the make-up of atoms contributing to the lowest 1% participation fraction, and the highest 1% participation fraction, respectively. The latter is seen to be dominated by Cu (or Zr) atoms in GUMs. (7)

We have also examined the dependence on local environments for Zr atoms. A plot analogous to Figure 6-3a, this time for Zr-centered coordination polyhedra, is shown in Figure 6-3b. Here from left to right each solid bar represents a bin that contains 10% of all the Zr atoms, in ascending order from the lowest to the highest $\mathbf{P}_i$. In addition, the 1% Zr atoms with the lowest $\mathbf{P}_i$ and the top 1% with the highest $\mathbf{P}_i$ are displayed on either end, each with a separate bar. The most favorable Zr-centered Kasper polyhedra in this MG are of the Z16 type (<0, 0, 12, 4>) (6). Interestingly, for the Zr atoms with the 1% lowest participation fraction, ~75% of them are enclosed in <0, 0, 12, 4>, much greater than the sample average of ~17% in this MG (6). In contrast, GUMs that deviate considerably from the CN=16 Kasper polyhedra and their close cousins (see legends in Figure 6-3) only constitute ~5%. Conversely, for the 1% of Zr atoms with the highest participation fraction, GUMs account for as high as 76% while the share of Z16 clusters is as low as 1.6%.

We now illustrate the GUMs, i.e., the typical types of coordination polyhedra that are strongly correlated with the soft modes. Figure 6-4 (a) and (b) illustrate the local environments of the top 5 Cu atoms and Zr atoms, respectively, i.e., those with the highest participation fractions. For these five Cu-centered GUMs, the coordination polyhedra have Voronoi indices <0, 0, 12, 2>, <0, 4, 4, 4>, <0, 6, 0, 6>, <0, 4, 4, 3>, <0, 3, 6, 2>. For the five Zr GUMs, they are <1, 3, 4, 4>, <1, 2, 6, 5>, <0, 2, 9, 4>, <0, 3, 7, 4> and <0, 4, 5, 6>. Clearly, they are among the polyhedra that deviate most significantly from the geometrically preferable Frank-Kasper polyhedra <0, 0, 12, 0> (for Cu) and <0, 0, 12, 4> (for Zr). Specifically, they are non-Kasper polyhedra, containing an increased

density of extrinsic (e.g., four-fold) disclinations (18)) at the favored CN, or clusters (including Kasper polyhedra) with unfavorable (too large or too small) CNs. So from the perspective of either constituent element, Cu or Zr, these are the most geometrically unfavored clusters at the given alloy composition and atomic size ratio. According to Ref. (156), transverse vibrational modes associated with defective (more disordered) soft structures could also be an origin of the boson peak (157) (the excess rise in low frequency vibrational modes of the $D(\omega)$).

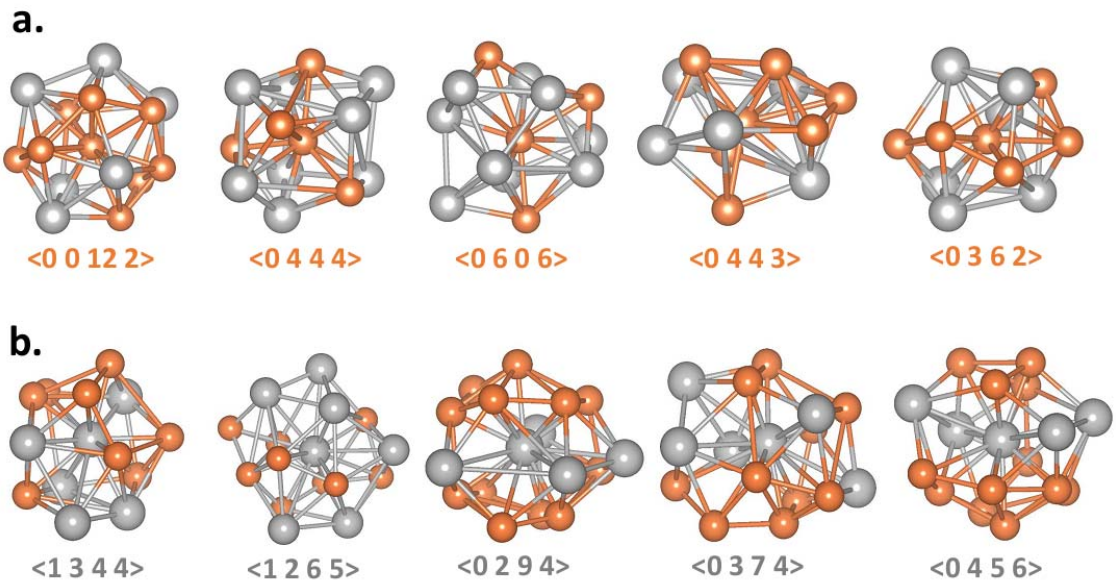

Figure 6-4. Configurations of five different (a) Cu-centered and (b) Zr-centered polyhedra, in which the center atoms are the top five atoms with the highest participation fractions for each constituent species. These are representatives of GUMs in this MG. Orange spheres are for Cu atoms and silver ones for Zr atoms. (7)

6.5. Soft spots identified by low-frequency vibrational modes

One eye-catching feature of mechanical deformation in MGs is that the plasticity in MGs are believed to be carried by STZs (97, 98, 117, 118, 132, 262, 301), which is a group of ~100 atoms that transform cooperatively under shear deformation. This behavior is unlike the plasticity carried by dislocations in crystalline alloys. Different from dislocations in crystals, STZs prior to loading usually do not exist as obvious defects with distinctly different structure compared to the matrix; they are simply local groups of atoms responding to the given applied load to produce shear strains. Thus to identify those "soft spots" that are prone to shear transformation will be important to understand mechanical behavior of amorphous alloys (7).

6.5.1. Characterization of shear transformations in deformed metallic glasses

To study the deformed MG, athermal quasi-static shear (AQS) (274) was imposed on the MG to different shear strains (γ) to induce atomic rearrangements during deformation, which were quantified by the local minimum non-affine displacement ($\boldsymbol{D}^2_{\min}$) (7), as defined in Eqn. (5-2) of Chapter 5. To calculate the parameter, we follow the procedure as detailed in the paper by Refs. (2, 118, 260). Then we characterize the shear transformation in deformed metallic glasses by tracking the atomic strain of each atom during deformation, and dissociating the strain into the best affine fit and the non-affine residue (118). When a shear transformation event sets in, a group of atoms cooperatively rearrange relative to one another, such that there will be a jump in $\boldsymbol{D}^2_{\min}$ (see Eqn. 6-1) to different magnitudes for each of the atoms involved. Ref. (7) presents the details of our

procedure to monitor the $\boldsymbol{D}^2_{\min}$ jumps. The Cu and Zr atoms that are located next to one another and undergo simultaneous $\boldsymbol{D}^2_{\min}$ jumps are identified as those that have experienced obvious shear transformations and contributed the most to inelastic relaxation. In our simulations, we monitor $\Delta\boldsymbol{D}^2_{min}$ to compare two configurations that are close by, i.e., next to one another. Specifically, we compare two consecutive configurations separated by a global shear strain difference of $\Delta\gamma$=0.1% under AQS. A typical example is shown in Figure 6-5a, where $\Delta\boldsymbol{D}^2_{min}$ of three typical atoms are plotted as a function of shear strain up to $\gamma = 5\%$. For instance, Atom I and II can be observed to undertake obvious $\Delta\boldsymbol{D}^2_{min}$ jump at about $\gamma = 4\%$ and $\gamma = 2.3\%$, respectively, whereas atom III exhibits no jump of $\Delta\boldsymbol{D}^2_{min.}$ Figure 6-5b shows the distribution of atoms undergoing different $\Delta\boldsymbol{D}^2_{min}$. As indicated in Figure 6-5b, we chose a threshold (grey bar): atoms that have $\Delta\boldsymbol{D}^2_{min}$ above this threshold are taken to be the most obvious ones that have undertaken shear transformations. The behavior of these atoms is analyzed in the following section.

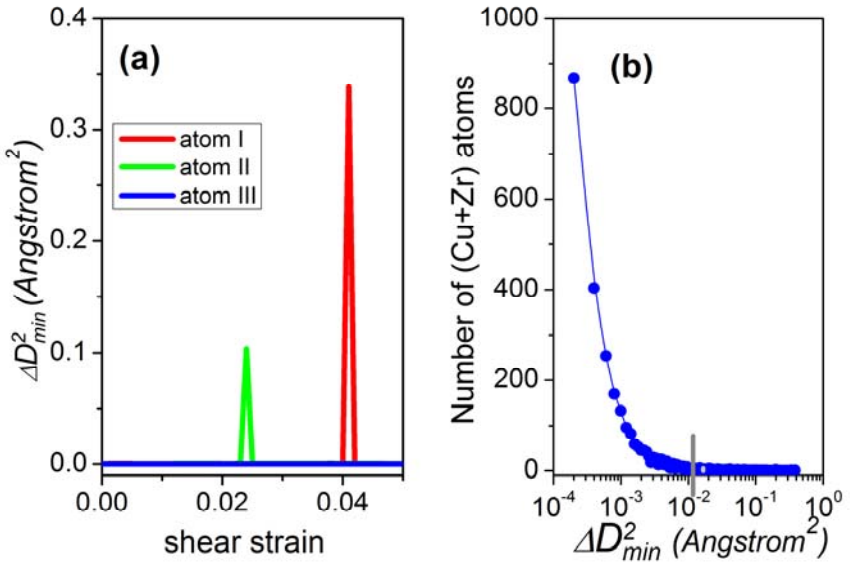

Figure 6-5. (a) $\Delta \boldsymbol{D}^2_{min}$ versus shear strain, for three typical atoms in $Cu_{64}Zr_{36}$ metallic glass under athermal quasi-static shear to a shear strain $\gamma = 5\%$. Atom I and II have apparently experienced shear transformation, but not atom III. (b) Distribution of maximum jump of $\Delta \boldsymbol{D}^2_{min}$. Those atoms in the tail, i.e., those with $\Delta \boldsymbol{D}^2_{min}$ above the threshold grey bar are stand-out atoms that have experienced obvious shear transformations.(7)

6.5.2. Correlation between shear transformation and soft spots

The next task at hand is to correlate the relaxation events with vibrational modes. In a two-dimensional sheared model glass, Manning *et al.* (291) recently utilized low-frequency vibrational modes to identify "soft spots" where particle rearrangements are initiated. Here we employ a similar analysis on our 3-D realistic $Cu_{64}Zr_{36}$ glass. The contoured maps of participation fraction $\mathbf{P}_i$ for all the (Cu and Zr) atoms inside four

representative slabs, each with a thickness of 2.5 Å (roughly the average atomic spacing), are plotted in Figure 6-6 (a-d). We notice that the $\mathbf{P}_i$ distributions are heterogeneous: atoms that participated the most in soft modes tend to aggregate together, with a typical correlation length of ~1 nm. For a direct comparison, the local atomic rearrangements in sheared $Cu_{64}Zr_{36}$ MG (under AQS to a global shear strain $\gamma = 5\%$, well before global yielding/flow of the entire sample, which happens at $\gamma = 12\%$) are superimposed in Figure 6-6(a-d), where white spheres represent the (Cu or Zr) atoms that have experienced the most obvious shear transformations (largest jumps of $\boldsymbol{D}^2_{\min}$ that are clearly above other atoms (7)). The distribution of these atoms is also inhomogeneous and, interestingly, almost always overlaps with the regions with high $\mathbf{P}_i$. This observation is consistent with the correlation between quasi-localized low-frequency modes and low energy barriers (292). However, note that not all regions with the highest participation fraction $\mathbf{P}_i$, undergo shear transformation, as seen in Figure 6-6 (as well as Figure 6-7). This is reasonable because a correlation in an amorphous systems is expected to be statistical (i.e. Fig. 6), rather than definitive, as also seen in Refs.(290, 291). That may be caused by fluctuation in MGs, such as complicate stress field and interaction among a population of shear transformation zones in disordered solids. Thus atomic rearrangement will not necessarily happen in the regions with the lowest energy barrier but could occur in any one of the regions with certain probability.(291)

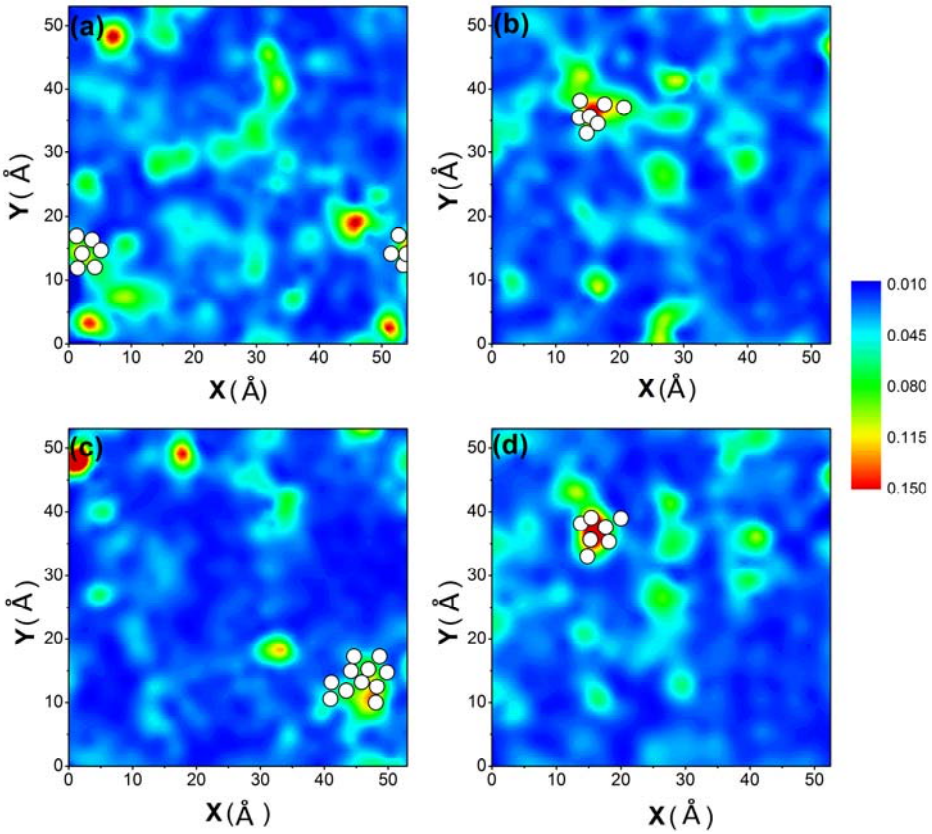

Figure 6-6. Contoured maps showing the spatial distribution of participation fraction $\mathbf{P}_i$ (see sidebar) for all (Cu and Zr) atoms in the $Cu_{64}Zr_{36}$ metallic glass with the cooling rate of 10^9 K/s. The four thin slabs (a-d) each has a thickness of 2.5 Å. White spots superimposed in the maps mark the locations of atoms that have experienced clear shear transformations under athermal quasi-static shear to a strain of 5%. (7)

An implication is that the small groups of atoms involved in soft modes are the most prone to shear transformations under imposed deformation. After $\gamma = 10\%$ (before global yielding), we again plot the contour maps for four thin slabs, similar to those in Figure 6-6. They are shown in Figure 6-7 (a-d) below, where white spheres are the (Cu or

Zr) atoms that have experienced the most obvious shear transformations. Those atoms now amount to ~8% of all the atoms in the system, and all cluster together similar to the case of $\gamma = 5\%$. Of course, not all soft mode locations would undergo shear transformations in a particular loading (given stress and strain tensor), but it is clear that statistically there is an obvious correlation between the two. The same was found in other models (290, 291).

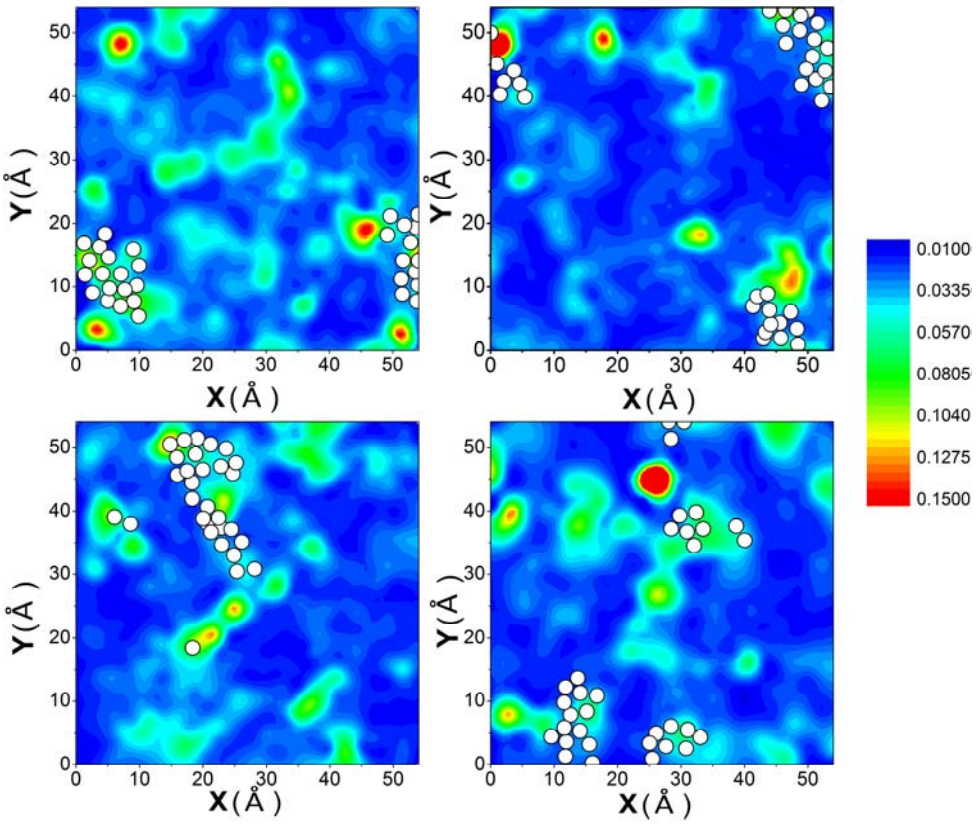

Figure 6-7. Contoured maps showing the spatial distribution of participation fraction $\mathbf{P}_i$ (see sidebar) for all atoms in the $Cu_{64}Zr_{36}$ MG (cooling rate=10^9 K/s). The four slabs (a-d) each has a thickness of 2.5 Å. White spots superimposed in the maps mark the locations of (Cu or Zr)

atoms that have experienced clear shear transformations under athermal quasi-static shear to $\gamma = 10\%$. (7)

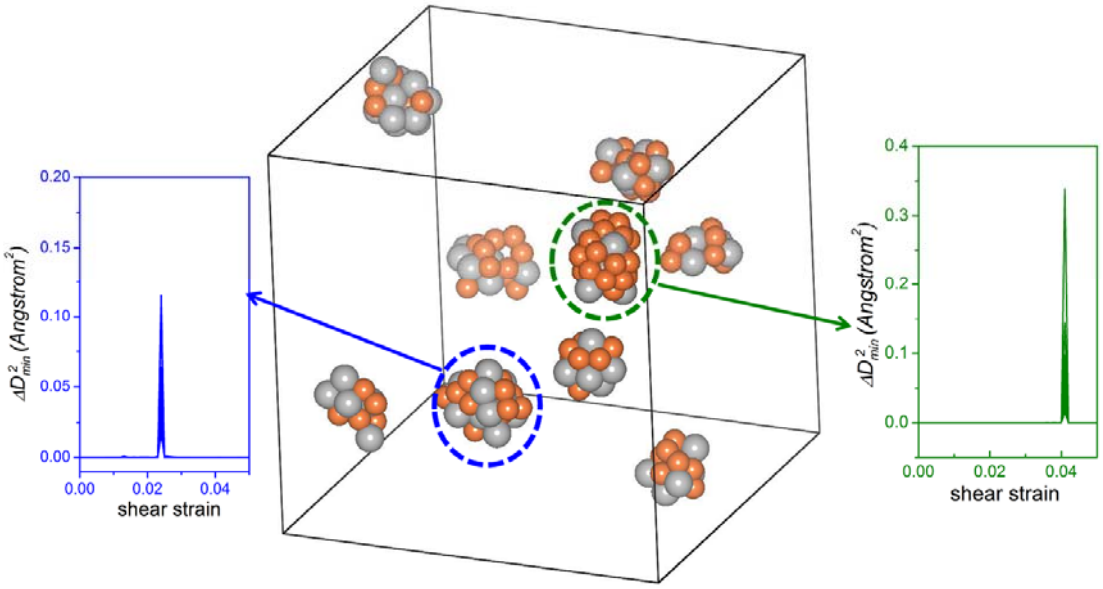

Figure 6-8. Cluster of atoms that have undergone obvious shear transformations (7) in $Cu_{64}Zr_{36}$ metallic glass sheared to $\gamma = 5\%$. Atoms in each cluster are activated at the same time, as indicated by their simultaneous jump in $\Delta \boldsymbol{D}^2_{min}$ at the same shear strain γ. Two such shear transformation zones are circled, with the inset displaying the overlapping $\Delta \boldsymbol{D}^2_{min}$ jumps of the atoms involved in each cluster. (7)

Figure 6-8 displays the locations of all such Cu and Zr atoms in the simulation model, which are about 2% of the total number of atoms in the box. Two features are highly noteworthy. First, they form clusters (only 6 atoms are exceptions, being isolated in a group of <3 atoms), each comprising 10 to 40 atoms (Cu in orange and Zr in gray

color). Second, the atoms in each cluster record a simultaneous jump in $\boldsymbol{D}^2_{\min}$. Taken together, the spatial and temporal correlations clearly indicate that these are the clusters of atoms that each has been through a well-defined shear transformation. An implication is that under imposed deformation the shear transformations have a strong tendency to arise from the collection of atoms involved in soft modes.

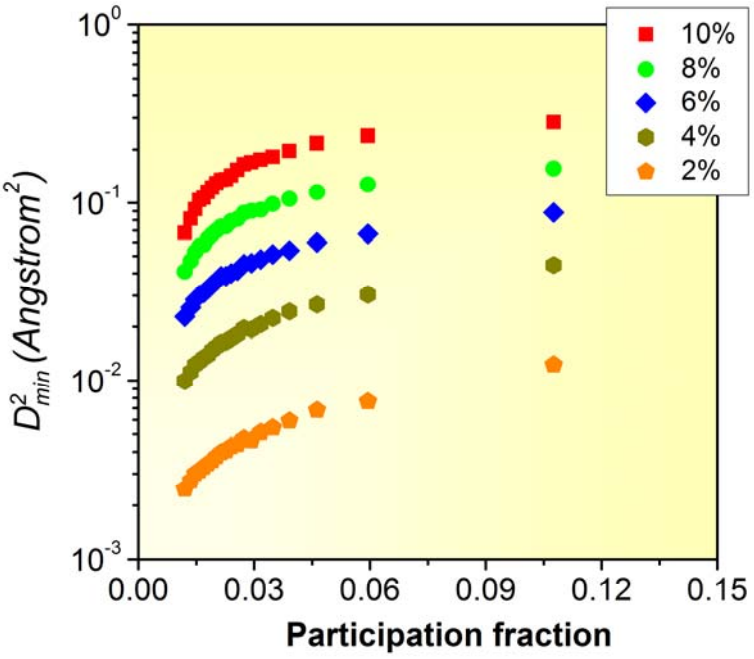

Figure 6-9. Correlation between the average D^2_{min} (with reference to undeformed configuration) with participation fraction $\mathbf{P}_i$, for all the (Cu and Zr) atoms in the $Cu_{64}Zr_{36}$ metallic glass deformed to different γ levels (2% to 10%). Each data point is the average for 5% of all the atoms, sorted in the order of increasing $\mathbf{P}_i$. (7)

The statistical correlation is obvious for the entire range of imposed γ, from 2% to 10%. As another way to see this correlation, we present in Figure 6-9 a plot correlating the average participation fraction with $D^2_{\min}$ (with respect to undeformed configuration), for γ from 2% to 10%. Each data point is an average for 5% of all the atoms inside a bin (each bin contains atoms grouped in ascending participation fraction). Obviously, the atoms with higher participation in soft mode contribute more to the non-affine deformation. This trend persists throughout the entire range of strains we studied.

6.5. Conclusion

In conclusion, we have studied the low-frequency vibrational normal modes and identified soft spots in a $Cu_{64}Zr_{36}$ metallic glass. They are "soft" in the sense that the atoms (Cu, Zr in our case) in those local environments participate preferentially in soft vibrational modes, and at the same time they have the highest propensity to undergo shear transformations. These two aspects are found to be strongly correlated: shear transformations in an MG preferentially occur at localized soft modes. In the language of the potential energy landscape, we have established a correlation between the curvature at the bottom of the basin (stiffness) with the barrier for transitions between basins (energy barrier against reconfiguration). Importantly, we have shown that both have a common signature in the local atomic packing environments: the geometrically uncomfortable motifs are the local configurations most prone to instability. The GUMs, as the most disordered atomic arrangements, have been referred to as "liquid-like" regions in the literature (e.g., Refs. (4, 21, 112, 277)). They tend to be soft and fertile for shear

transformations. Such a correlation, albeit statistical (not all soft modes or GUMs would undergo shear transformations for a given stress state/magnitude and loading duration), is very useful and important as a step forward in establishing a concrete structure-property relationship for MGs, i.e., a direct connection between short-range order and vibrational soft modes as well as stress-induced atomic rearrangements.

Chapter 7

Summary

7.1 Accomplishments and findings

The conclusions reached in this research have been presented in detail in the individual chapters. Before ending this thesis, here we briefly recall the tasks and goals we set out to accomplish, and the achievements we have made in this study of the local structure and the structural signature of properties in metallic glasses and supercooled liquids.

The first and foremost task of this study is to solve the local structures of metallic glasses, which also constitutes the basis for all the other tasks. Taking advantage of classical MD simulations with reliable/realistic EAM potentials and *ab initio* MD, we first focused on full icosahedra short-range order (FISRO, with Voronoi index <0, 0, 12, 0>), which is favored at the Cu-rich Cu-Zr alloy composition ($Cu_{64}Zr_{36}$ MG models were chosen in this research) (6) and illustrated that, Cu-centered full icosahedra (FI) constitute the dominant and characteristic short-range-ordered coordination motif. The ordering of Cu-centered FISRO have been discussed in details (6), including i) the accompanying preference of a particular type of Zr-centered Kapser coordination polyhedral (with Voronoi index <0, 0, 12, 4>); ii) the evolution and conversion of polyhedral connection schemes in the medium range, and iii) the formation and percolation of networks formed by interpenetrating connection of icosahedra to constitute a stiff backbone over extended range. However, most of MGs do not contain the dominated FISRO and two typical models were selected as representative candidates: Mg-based tertiary MG, $Mg_{65}Cu_{25}Y_{10}$ (3) and metal-metalloid MG, $Pd_{82}Si_{18}$ (1, 5). Both of them constitute with the characteristic short-range order (SRO) of prism-type: Cu-centered bi-capped square antiprisms (BSAP) and tri-capped trigonal prisms (TTP) for Mg-Cu-Y (3) and Si-centered TTP for Pd-Si (1, 5).

Despite the topological order in MGs, their electronic structure, especially the bonding nature was also discussed accompanying the investigation of atomic packing structure. For Mg-Cu-Y in our study, bond shortening is observed for Mg-Cu and Y-Cu bonds, due to appreciable charge transfer (or ionicity) that imparts an ionic character to the bonding. This enhances their chemical affinity, accentuating Cu-centered motifs

analogous to solute-centered prisms in metal-metalloid MGs, in this all-metal system. Moreover, other atomic structural indicators, such as atomic volume and atomic stress, can also undertake the influence by charger transfer (229), which thus should attract more research attention to in addition to atomic packing structure , though it's still very challenging to direct link electronic structure with properties in amorphous solids. (see more discussion in Section 7.2)

Armed with atomic-level structural indicators, we move to utilize MD simulation to examine the structural signature of several intriguing properties of MGs and supercooled liquids, such as evolution of excess specific heat as well as dynamical slowdown (1), elastic heterogeneity (2, 4) and low-frequency vibrational normal modes (7) and so on. We have clearly illustrated these underlying local structural correlations, especially by short-to-medium range order in MGs, which will be presented as following:

Firstly, it's widely observed that the specific heat C_p of metallic glass-forming supercooled liquids exhibits different temperature (T) dependence: some follow weak T-dependence in contrast with some others showing rapid development (86). In this study, we have employed MD simulations to compare $Cu_{64}Zr_{36}$ and $Mg_{65}Cu_{25}Y_{10}$/ $Pd_{82}Si_{18}$ liquids (1, 3), while the former system exhibits rapid increase of specific heat in the supercooled liquid region, the latter two systems show much shallower T-dependence. The fast rise in excess specific heat in $Cu_{64}Zr_{36}$ supercooled liquids has been demonstrated to correlate with increasing structural ordering and particular the FISRO as well as the medium-range packing of these local motifs. The drop of the enthalpy H accelerates with undercooling, as the icosahedral clusters increase in number and improve their local five-fold symmetry and chemical SRO. The resulting change in the curvature

of the *H-T* curve is responsible for the fast rising C_p. On the contrary, the characteristic SRO (prism-type) as well as cluster connections in $Mg_{65}Cu_{25}Y_{10}$ and $Pd_{82}Si_{18}$ supercooled liquids are prevalent even at high temperatures, and gradually increase with decreasing temperature. This is consistent with their gradual evolution of excess specific heat (1, 3).

Moreover, the liquid fragility evaluated by evolution of viscosity as well as relaxation time is related directly to the temperature dependence of the excess specific heat as discussed above (86). This is reflected among the studied model liquids, where the $Cu_{64}Zr_{36}$ liquid is more fragile, in comparison with the "stronger" $Pd_{82}Si_{18}$ and $Mg_{65}Cu_{25}Y_{10}$ metallic liquids (1, 3). The existence of ordered clusters enhance the liquid relaxation as well as the lifetime of local topology. In other words, the supercooled liquid with a larger fraction of ordered clusters exhibits longer relaxation times, as well as increased viscosity, influencing the liquid fragility.

The next step attempts to unravel the correlation of structural features with mechanical deformation in metallic glasses. We mainly study the local structural signature of elastic heterogeneity in Cu-Zr MGs with respect to three aspects: i) the correlation of elastic deformation with the internal structure on the atomic level (2); ii) the local solidity/liquidity in metallic glasses (4) (i.e., how solid-like/liquid-like a local region/configuration is), as well as to establish a correlation between the solidity/liquidity and the local topological order; iii) the formation and percolation of networks formed by interpenetrating connection of icosahedra to constitute a stiff backbone over extended range and exert an influence upon the shear modulus (the change in slope of shear modulus versus configurational potential energy) (6).

Finally, we uncover a direct link between local atomic packing structure and the low-frequency quasilocalized vibrational normal modes, which is a characteristic vibrational properties in amorphous solids (7). In a three-dimensional model mimicking realistic $Cu_{64}Zr_{36}$ metallic glass, geometrically unfavored motifs (GUMs) constitute the most flexible local environments that encourage soft modes and high propensity for shear transformations, while local configurations preferred in this alloy, i.e., the full icosahedra (around Cu) and Z16 Kasper polyhedra (around Zr), contribute the least. Moreover, we demonstrated that quasilocalized low-frequency vibrational modes correlate strongly with fertile sites for shear transformations (7).

7.2 Future work

The first task for future work is to develop new theoretical models and methodologies to characterize structure order more accurately at a medium-range scale, which can be advantageous over our currently employed methods. The importance of this task is from the medium range scale (usually with the length scale as ~1 nm or ~100 atoms) for lots of properties in MGs and supercooled liquids, such as dynamics (302-308) and elastic heterogeneity (112, 116), shear localization (e.g., shear transformation zones) (107, 117, 118, 132, 298, 309-313) and so on. This could lead to better understanding of structure-properties relationship than perspectives only from short-range order in metallic glasses and supercooled liquids.

In addition to studied atomic packing structure in amorphous alloys, their electronic structural basis needs to be examined thoroughly and systematically in future work.

Although previous work has been implemented by many researchers including us, to explore the bond nature (such as covalency (221), ionicity (12, 214, 229, 314), etc), density of states (DOS) (219, 252, 315), valence electron density (218, 316-318) etc in MGs, there remains vast room to improve our understanding quantitatively, which is a quite challenging task due to the very complicated nature of those materials. Additionally we hope to relate electronic structure directly to properties of amorphous alloys (such as glass-forming ability, ductility, liquid fragility etc) and how these relate to the short-to-medium range topological and chemical order.

Moreover, glass-forming ability (GFA) of MGs need to be further investigated from the perspective of underlying local structure in the process of crystallization, including nucleation and movement of crystal/liquid interface (319). Previously five-fold symmetry or icosahedral order in liquids was noted to present a pronounced energy barrier to crystallize (22, 28, 169, 182, 307, 320-328). This will have a profound effect on the emerging crystal nucleus and the growth of the crystal phase via moving crystal/liquid interface. Thus this kind of local structural order may account for contrasting behavior with respect to the competition between the glass transition and crystallization, factors critical for the evaluation of GFA.

Another intriguing topic regards the ultra-stable glasses, which deserve to be explored further in the future work. Current so-called ultra-stable metallic glasses are usually made by vapor deposition methods (329, 330) both in experiments and simulation. However, such glasses are controversial because a significant fraction of the stabilization effect is attributed to inhomogeneous compositions that arise near the interfaces of the films (331). Thus new methodologies will be needed to produce ultra-stable metallic

glasses and probe the corresponding local structure in order to elucidate their underlying structure and various properties compared to conventional MGs.

Appendix

This content includes several papers which were published during my PhD study but NOT directly related to the frame of this thesis and hence not discussed in details.

1. Ding J & Cheng Y (2014) Charge transfer and atomic-level pressure in metallic glasses. *Applied Physics Letters* 104(5):051903.

2. Ding J, Cheng Y, & Ma E (2014) On the origin of elastic strain limit of bulk metallic glasses. *Applied Physics Letters* 104(1):011912.

3. Ding J*, et al.* (2014) Temperature effects on atomic pair distribution functions of melts. *The Journal of Chemical Physics* 140(6):064501.

4. Wang C-C*,* Ding J, Cheng Y, Wan JL, Tian L *et al.* (2012) Sample size matters for Al88Fe7Gd5 metallic glass: Smaller is stronger. *Acta Materialia* 60(13-14):5370-5379.

5. Xu M, Ding J, & Ma E (2012) One-dimensional stringlike cooperative migration of lithium ions in an ultrafast ionic conductor. *Applied Physics Letters* 101(3):031901.

Bibliography

1. Ding J, Cheng Y-Q, Sheng H, & Ma E (2012) Short-range structural signature of excess specific heat and fragility of metallic-glass-forming supercooled liquids. *Physical Review B* 85(6).

2. Ding J, Cheng YQ, & Ma E (2012) Correlating local structure with inhomogeneous elastic deformation in a metallic glass. *Applied Physics Letters* 101(12).

3. Ding J, Cheng Y, & Ma E (2013) Charge-transfer-enhanced prism-type local order in amorphous Mg65Cu25Y10: Short-to-medium-range structural evolution underlying liquid fragility and heat capacity. *Acta Materialia* 61(8):3130-3140.

4. Ding J, Cheng Y, & Ma E (2013) Quantitative measure of local solidity/liquidity in metallic glasses. *Acta Materialia* 61(12):4474-4480.

5. Cheng Y, Ding J, & Ma E (2013) Local topology vs. atomic-level stresses as a measure of disorder: Correlating structural indicators for metallic glasses. *Materials Research Letters* 1(1):3-12.

6. Ding J, Cheng Y, & Ma E (2014) Full icosahedra dominate local order in Cu64Zr34 metallic glass and supercooled liquid. *Acta Materialia* 69:343-354.

7. Ding J, Patinet S, Falk ML, Cheng Y, & Ma E (2014) Soft spots and their structural signature in a metallic glass. *Proceedings of the National Academy of Sciences (PNAS)* doi: 10.1073/pnas.1412095111.

8. Klement W, Willens R, & Duwez P (1960) Non-crystalline Structure in Solidified Gold-Silicon Alloys. *Nature* 187(4740):869-870.

9. Chaudhari P & Turnbull D (1978) Structure and properties of metallic glasses. *Science* 199(4324):11-21.

10. Johnson W (1999) Bulk glass-forming metallic alloys: Science and technology. *MRS Bulletin* 24(10):42-56.

11. Greer AL & Ma E (2007) Bulk metallic glasses: At the cutting edge of metals research. *MRS Bulletin* 32(8):611-615.

12. Inoue A (2000) Stabilization of metallic supercooled liquid and bulk amorphous alloys. *Acta Materialia* 48(1):279-306.

13. Dieter GE & Bacon D (1986) *Mechanical metallurgy* (McGraw-Hill New York).

14. Cahn RW & Haasen P (1996) *Physical metallurgy. Vol. 1-3* (North-Holland).

15. Gleiter H (1989) Nanocrystalline materials. *Progress in Materials Science* 33(4):223-315.

16. Villars P & Calvert LD (1985) *Pearson's handbook of crystallographic data for intermetallic phases* (American Society for Metals Metals Park, OH).

17. Barrett CS & Massalski TB (1966) *Structure of metals* (McGraw-Hill New York).

18. Cheng YQ & Ma E (2011) Atomic-level structure and structure-property relationship in metallic glasses. *Progress in Materials Science* 56(4):379-473.

19. Sheng HW, Luo WK, Alamgir FM, Bai JM, & Ma E (2006) Atomic packing and short-to-medium-range order in metallic glasses. *Nature* 439(7075):419-425.

20. Miracle DB (2004) A structural model for metallic glasses. *Nature Materials* 3(10):697-702.

21. Egami T (2011) Atomic level stresses. *Progress in Materials Science* 56(6):637-653.

22. Nelson DR & Spaepen F (1989) Polytetrahedral order in condensed matter. *Solid State Physics* 42:1-90.

23. Debenedetti PG & Stillinger FH (2001) Supercooled liquids and the glass transition. *Nature* 410(6825):259-267.

24. Ediger MD, Angell CA, & Nagel SR (1996) Supercooled liquids and glasses. *Journal of Physical Chemistry* 100(31):13200-13212.

25. Angell CA, Ngai KL, McKenna GB, McMillan PF, & Martin SW (2000) Relaxation in glassforming liquids and amorphous solids. *Journal of Applied Physics* 88(6):3113-3157.

26. Ediger MD & Harrowell P (2012) Perspective: Supercooled liquids and glasses. *Journal of Chemical Physics* 137(8).

27. Barrat JL & Klein ML (1991) Molecular-dynamics simulations of supercooled liquids near the glass-transition. *Annual Review of Physical Chemistry* 42:23-53.

28. Shintani H & Tanaka H (2006) Frustration on the way to crystallization in glass. *Nature Physics* 2(3):200-206.

29. Cugliandolo LF, Kurchan J, & Peliti L (1997) Energy flow, partial equilibration, and effective temperatures in systems with slow dynamics. *Physical Review E* 55(4):3898-3914.

30. Cheng YQ & Ma E (2009) Configurational dependence of elastic modulus of metallic glass. *Physical Review B* 80(6).

31. Johnson WL, Demetriou MD, Harmon JS, Lind ML, & Samwer K (2007) Rheology and ultrasonic properties of metallic glass-forming liquids: A potential energy landscape perspective. *MRS Bulletin* 32(08):644-650.

32. Lind ML, Duan G, & Johnson WL (2006) Isoconfigurational elastic constants and liquid fragility of a bulk metallic glass forming alloy. *Physical Review Letters* 97(1):015501.

33. Duan G*, et al.* (2006) Strong configurational dependence of elastic properties for a binary model metallic glass. *Applied Physics Letters* 89(15).

34. Utz M, Debenedetti PG, & Stillinger FH (2000) Atomistic simulation of aging and rejuvenation in glasses. *Physical Review Letters* 84(7):1471.

35. Chen H (1978) The influence of structural relaxation on the density and Young's modulus of metallic glasses. *Journal of Applied Physics* 49(6):3289-3291.

36. Lu Z & Liu C (2002) A new glass-forming ability criterion for bulk metallic glasses. *Acta Materialia* 50(13):3501-3512.

37. Ding S*, et al.* (2014) Combinatorial development of bulk metallic glasses. *Nature Materials* 13(5):494-500.

38. Li Y, Guo Q, Kalb J, & Thompson C (2008) Matching glass-forming ability with the density of the amorphous phase. *Science* 322(5909):1816-1819.

39. Egami T & Billinge SJ (2003) *Underneath the Bragg peaks: structural analysis of complex materials* (Elsevier).

40. Warren BE (1969) *X-ray Diffraction* (Courier Dover Publications).

41. Klug HP & Alexander LE (1974) X-ray diffraction procedures: for polycrystalline and amorphous materials. *X-Ray Diffraction Procedures: For Polycrystalline and Amorphous Materials, 2nd Edition, by Harold P. Klug, Leroy E. Alexander, pp. 992. ISBN 0-471-49369-4. Wiley-VCH, May 1974.* 1.

42. Cullity BD & Stock SR (2001) *Elements of X-ray Diffraction* (Pearson).

43. Lorch E (1969) Neutron diffraction by germania, silica and radiation-damaged silica glasses. *Journal of Physics C: Solid State Physics* 2(2):229.

44. Allen FH*, et al.* (1987) Tables of bond lengths determined by X-ray and neutron diffraction. Part 1. Bond lengths in organic compounds. *J. Chem. Soc., Perkin Trans. 2* (12):S1-S19.

45. Teo BK (1986) *EXAFS: basic principles and data analysis* (Springer-Verlag Berlin).

46. Rehr J & Albers R (2000) Theoretical approaches to x-ray absorption fine structure. *Reviews of Modern Physics* 72(3):621-654.

47. Sayers DE, Stern EA, & Lytle FW (1971) New technique for investigating noncrystalline structures: Fourier analysis of the extended X-ray—absorption fine structure. *Physical Review Letters* 27(18):1204.

48. Lee P, Citrin P, Eisenberger Pt, & Kincaid B (1981) Extended X-ray absorption fine structure—its strengths and limitations as a structural tool. *Reviews of Modern Physics* 53(4):769.

49. Koningsberger D & Prins R (1988) X-ray absorption: principles, applications, techniques of EXAFS, SEXAFS, and XANES.

50. Voyles P, Gibson J, & Treacy M (2000) Fluctuation microscopy: a probe of atomic correlations in disordered materials. *Journal of Electron Microscopy* 49(2):259-266.

51. Hwang J*, et al.* (2012) Nanoscale structure and structural relaxation in Zr 50 Cu 45 Al 5 bulk metallic glass. *Physical Review Letters* 108(19):195505.

52. Voyles P & Hwang J (2012) Fluctuation Electron Microscopy. *Characterization of Materials*.

53. Williams DB & Carter CB (2009) The Transmission electron microscope. *Transmission Electron Microscopy*, (Springer), pp 3-22.

54. Reimer L & Kohl H (2008) *Transmission electron microscopy: physics of image formation* (Springer).

55. Xi X, Li L, Zhang B, Wang W, & Wu Y (2007) Correlation of atomic cluster symmetry and glass-forming ability of metallic glass. *Physical Review Letters* 99(9).

56. Callaghan PT (1991) *Principles of nuclear magnetic resonance microscopy* (Clarendon Press Oxford).

57. Ernst RR, Bodenhausen G, & Wokaun A (1991) Principles of nuclear magnetic resonance in one and two dimensions.

58. Allen M & Tildesley D (1989) Computer simulation of liquids, 1987. *New York: Oxford* 385.

59. Frenkel D & Smit B (2001) *Understanding molecular simulation: from algorithms to applications* (Academic press).

60. Rapaport DC (2004) *The art of molecular dynamics simulation* (Cambridge university press).

61. Kresse G & Hafner J (1993) Ab initio molecular dynamics for liquid metals. *Physical Review B* 47(1):558.

62. Kresse G & Hafner J (1994) Ab initio molecular-dynamics simulation of the liquid-metal–amorphous-semiconductor transition in germanium. *Physical Review B* 49(20):14251.

63. McGreevy R (2001) Reverse Monte Carlo modelling. *Journal of Physics-Condensed Matter* 13(46):R877-R913.

64. McGreevy R & Pusztai L (1988) Reverse Monte Carlo simulation: a new technique for the determination of disordered structures. *Molecular Simulation* 1(6):359-367.

65. Keen D & McGreevy R (1990) Structural modelling of glasses using reverse Monte Carlo simulation.

66. Hirata A, *et al.* (2011) Direct observation of local atomic order in a metallic glass. *Nature Materials* 10(1):28-33.

67. Hirata A, *et al.* (2013) Geometric Frustration of Icosahedron in Metallic Glasses. *Science* 341(6144):376-379.

68. Bernal J (1960) Geometry of the structure of monatomic liquids. *Nature* 185(4706):68-70.

69. Finney J (1970) Random packings and the structure of simple liquids. I. The geometry of random close packing. *Proceedings of the Royal Society of London. A. Mathematical and Physical Sciences* 319(1539):479-493.

70. Berryman JG (1983) Random close packing of hard spheres and disks. *Physical Review A* 27(2):1053.

71. Gaskell PH (1978) New structural model for transition metal-metalloid glasses. *Nature* 276(5687):484-485.

72. Treacy M & Borisenko K (2012) The local structure of amorphous silicon. *Science* 335(6071):950-953.

73. Sheng HW, Cheng YQ, Lee PL, Shastri SD, & Ma E (2008) Atomic packing in multicomponent aluminum-based metallic glasses. *Acta Materialia* 56(20):6264-6272.

74. Miracle DB (2006) The efficient cluster packing model - An atomic structural model for metallic glasses. *Acta Materialia* 54(16):4317-4336.

75. Ma D, Stoica AD, & Wang XL (2009) Power-law scaling and fractal nature of medium-range order in metallic glasses. *Nature Materials* 8(1):30-34.

76. Zeng Q*, et al.* (2014) Universal fractional noncubic power law for density of metallic glasses. *Physical Review Letters* 112(18):185502.

77. Ding J*, et al.* (2014) Temperature effects on atomic pair distribution functions of melts. *The Journal of Chemical Physics* 140(6):064501.

78. Suzuki Y, Haimovich J, & Egami T (1987) Bond-orientational anisotropy in metallic glasses observed by x-ray diffraction. *Physical review. B, Condensed matter* 35(5):2162.

79. Luo WK*, et al.* (2004) Icosahedral short-range order in amorphous alloys. *Physical Review Letters* 92(14).

80. Tanemura M, Ogawa T, & Ogita N (1983) A new algorithm for three-dimensional Voronoi tessellation. *Journal of Computational Physics* 51(2):191-207.

81. Steinhardt PJ, Nelson DR, & Ronchetti M (1981) Icosahedral Bond Orientational Order in Supercooled Liquids. *Physical Review Letters* 47(18):1297-1300.

82. Steinhardt PJ, Nelson DR, & Ronchetti M (1983) Bond-orientational order in liquids and glasses. *Physical Review B* 28(2):784-805.

83. Angell CA (1995) Formation of glasses from liquids and biopolymers. *Science* 267(5206):1924-1935.

84. Angell CA (2008) Glass-formers and viscous liquid slowdown since David Turnbull: Enduring puzzles and new twists. *MRS Bulletin* 33(5):544-555.

85. Busch R (2000) The thermophysical properties of bulk metallic glass-forming liquids. *JOM* 52(7):39-42.

86. Busch R, Schroers J, & Wang WH (2007) Thermodynamics and kinetics of bulk metallic glass. *MRS Bulletin* 32(8):620-623.

87. Busch R, Liu W, & Johnson WL (1998) Thermodynamics and kinetics of the Mg65Cu25Y10 bulk metallic glass forming liquid. *Journal of Applied Physics* 83(8):4134-4141.

88. Tanaka H (2003) Relation between thermodynamics and kinetics of glass-forming liquids. *Physical Review Letters* 90(5).

89. Tanaka H (2005) Relationship among glass-forming ability, fragility and short-range bond ordering of liquids. *Journal of Non-Crystalline Solids* 351(8-9):678-690.

90. A.V G (2002) The specific heat of simple liquids. *Journal of Non-Crystalline Solids* 307–310(0):376-386.

91. Kauzmann W (1948) The nature of the glassy state and the behavior of liquids at low temperatures. *Chemical Reviews* 43(2):219-256.

92. Zhang C, Hu L, Yue Y, & Mauro JC (2010) Fragile-to-strong transition in metallic glass-forming liquids. *The Journal of Chemical Physics* 133(1):014508.

93. Yamchi MZ, Ashwin S, & Bowles RK (2012) Fragile-Strong Fluid Crossover and Universal Relaxation Times in a Confined Hard-Disk Fluid. *Physical Review Letters* 109(22):225701.

94. Yang X*, et al.* (2014) Anomalous Crystallization as a Signature of the Fragile-to-Strong Transition in Metallic Glass Forming Liquids. *The Journal of Physical Chemistry B*.

95. Sun Q, Zhou C, Yue Y, & Hu L (2014) A Direct Link between the Fragile-to-Strong Transition and Relaxation in Supercooled Liquids. *The Journal of Physical Chemistry Letters* 5(7):1170-1174.

96. Evenson Z, Schmitt T, Nicola M, Gallino I, & Busch R (2012) High temperature melt viscosity and fragile to strong transition in Zr–Cu–Ni–Al–Nb (Ti) and Cu47Ti34Zr11Ni8 bulk metallic glasses. *Acta Materialia* 60(12):4712.

97. Schuh CA, Hufnagel TC, & Ramamurty U (2007) Overview No.144 - Mechanical behavior of amorphous alloys. *Acta Materialia* 55(12):4067-4109.

98. Chen M (2008) Mechanical behavior of metallic glasses: microscopic understanding of strength and ductility. *Annu. Rev. Mater. Res.* 38:445-469.

99. Wang WH (2012) The elastic properties, elastic models and elastic perspectives of metallic glasses. *Progress in Materials Science* 57(3):487-656.

100. Dmowski W & Egami T (2007) Observation of structural anisotropy in metallic glasses induced by mechanical deformation. *Journal of Materials Research* 22(2):412-418.

101. Furukawa A & Tanaka H (2009) Inhomogeneous flow and fracture of glassy materials. *Nature Materials* 8(7):601-609.

102. Hofmann D*, et al.* (2008) Designing metallic glass matrix composites with high toughness and tensile ductility. *Nature* 451(7182):1085-U1083.

103. Zhang Y (2010) Mechanical properties and structures of high entropy alloys and bulk metallic glasses composites. *Pricm 7, Pts 1-3* 654-656:1058-1061.

104. Ye JC, Lu J, Liu CT, Wang Q, & Yang Y (2010) Atomistic free-volume zones and inelastic deformation of metallic glasses. *Nature Materials* 9(8):619-623.

105. Wang WH (2011) Correlation between relaxations and plastic deformation, and elastic model of flow in metallic glasses and glass-forming liquids. *Journal of Applied Physics* 110(5).

106. Shi YF & Falk ML (2005) Strain localization and percolation of stable structure in amorphous solids. *Physical Review Letters* 95(9).

107. Shan ZW*, et al.* (2008) Plastic flow and failure resistance of metallic glass: Insight from in situ compression of nanopillars. *Physical Review B* 77(15).

108. Poulsen HF, Wert JA, Neuefeind J, Honkimäki V, & Daymond M (2004) Measuring strain distributions in amorphous materials. *Nature Materials* 4(1):33-36.

109. Hufnagel T, Ott R, & Almer J (2006) Structural aspects of elastic deformation of a metallic glass. *Physical Review B* 73(6):064204.

110. Vempati U, Valavala P, Falk M, Almer J, & Hufnagel T (2012) Length-scale dependence of elastic strain from scattering measurements in metallic glasses. *Physical Review B* 85(21).

111. Wang G*, et al.* (2012) Correlation between elastic structural behavior and yield strength of metallic glasses. *Acta Materialia* 60(6):3074-3083.

112. Dmowski W, Iwashita T, Chuang C, Almer J, & Egami T (2010) Elastic heterogeneity in metallic glasses. *Physical Review Letters* 105(20).

113. Weaire D, Ashby M, Logan J, & Weins M (1971) Use of pair potentials to calculate properties of amorphous metals. *Acta Metallurgica* 19(8):779-&.

114. Ma D*, et al.* (2012) Elastic moduli inheritance and the weakest link in bulk metallic glasses. *Physical Review Letters* 108(8):085501.

115. Wagner H*, et al.* (2011) Local elastic properties of a metallic glass. *Nature Materials* 10(6):439-442.

116. Liu Y*, et al.* (2011) Characterization of nanoscale mechanical heterogeneity in a metallic glass by dynamic force microscopy. *Physical Review Letters* 106(12):125504.

117. Argon A (1979) Plastic-deformation in metallic glasses. *Acta Metallurgica* 27(1):47-58.

118. Falk ML & Langer JS (1998) Dynamics of viscoplastic deformation in amorphous solids. *Physical Review E* 57(6):7192-7205.

119. Falk ML, Langer JS, & Pechenik L (2004) Thermal effects in the shear-transformation-zone theory of amorphous plasticity: Comparisons to metallic glass data. *Physical Review E* 70(1).

120. Langer J (2004) Dynamics of shear-transformation zones in amorphous plasticity: Formulation in terms of an effective disorder temperature. *Physical Review E* 70(4):041502.

121. Delogu F (2008) Identification and characterization of potential shear transformation zones in metallic glasses. *Physical Review Letters* 100(25):255901.

122. Takeuchi S & Edagawa K (2011) Atomistic simulation and modeling of localized shear deformation in metallic glasses. *Progress in Materials Science* 56(6):785-816.

123. Srolovitz D, Vitek V, & Egami T (1983) An atomistic study of deformation of amorphous metals. *Acta Metallurgica* 31(2):335-352.

124. Hirth JP & Lothe J (1982) Theory of dislocations.

125. Liu Y*, et al.* (2009) Thermodynamic origins of shear band formation and the universal scaling law of metallic glass strength. *Physical Review Letters* 103(6):65504.

126. Johnson W & Samwer K (2005) A Universal Criterion for Plastic Yielding of Metallic Glasses with a (T/T_ {g})^{2/3} Temperature Dependence. *Physical Review Letters* 95(19):195501.

127. Stillinger FH (1995) A topographic view of supercooled liquids and glass-formation. *Science* 267(5206):1935-1939.

128. Ding J, Cheng Y, & Ma E (2014) On the origin of elastic strain limit of bulk metallic glasses. *Applied Physics Letters* 104(1):011912.

129. Dasgupta R, Joy A, Hentschel H, & Procaccia I (2013) Derivation of the Johnson-Samwer T 2/3 temperature dependence of the yield strain in metallic glasses. *Physical Review B* 87(2):020101.

130. Cheng YQ & Ma E (2011) Intrinsic shear strength of metallic glass. *Acta Materialia* 59(4):1800-1807.

131. Cao AJ, Cheng YQ, & Ma E (2009) Structural processes that initiate shear localization in metallic glass. *Acta Materialia* 57(17):5146-5155.

132. Greer A, Cheng Y, & Ma E (2013) Shear bands in metallic glasses. *Materials Science and Engineering: R: Reports* 74(4):71-132.

133. Lewandowski J & Greer A (2005) Temperature rise at shear bands in metallic glasses. *Nature Materials* 5(1):15-18.

134. Zhang Y & Greer A (2006) Thickness of shear bands in metallic glasses. *Applied Physics Letters* 89(7):071907-071907-071903.

135. Zhang Z, Eckert J, & Schultz L (2003) Difference in compressive and tensile fracture mechanisms of Zr< sub> 59</sub> Cu< sub> 20</sub> Al< sub> 10</sub> Ni< sub> 8</sub> Ti< sub> 3</sub> bulk metallic glass. *Acta Materialia* 51(4):1167-1179.

136. Shimizu F, Ogata S, & Li J (2006) Yield point of metallic glass. *Acta Materialia* 54(16):4293-4298.

137. Zhang Y, Wang W, & Greer A (2006) Making metallic glasses plastic by control of residual stress. *Nature Materials* 5(11):857-860.

138. Trexler MM & Thadhani NN (2010) Mechanical properties of bulk metallic glasses. *Progress in Materials Science* 55(8):759-839.

139. Kim JY*, et al.* (2012) Suppression of catastrophic failure in metallic glass–polyisoprene nanolaminate containing nanopillars. *Advanced Functional Materials* 22(9):1972-1980.

140. Kim JY, Jang D, & Greer JR (2011) Nanolaminates Utilizing Size‐Dependent Homogeneous Plasticity of Metallic Glasses. *Advanced Functional Materials* 21(23):4550-4554.

141. Wu Y, Xiao Y, Chen G, Liu CT, & Lu Z (2010) Bulk Metallic Glass Composites with Transformation‐Mediated Work‐Hardening and Ductility. *Advanced Materials* 22(25):2770-2773.

142. Hofmann DC*, et al.* (2008) Development of tough, low-density titanium-based bulk metallic glass matrix composites with tensile ductility. *Proceedings of the National Academy of Sciences* 105(51):20136-20140.

143. Wondraczek L*, et al.* (2011) Towards ultrastrong glasses. *Advanced Materials* 23(39):4578-4586.

144. Wu Y*, et al.* (2012) Ductilizing bulk metallic glass composite by tailoring stacking fault energy. *Physical Review Letters* 109(24):245506.

145. Chu JP, *et al.* (2012) Bendable bulk metallic glass: Effects of a thin, adhesive, strong, and ductile coating. *Acta Materialia* 60(6):3226-3238.

146. Greer JR & De Hosson JTM (2011) Plasticity in small-sized metallic systems: Intrinsic versus extrinsic size effect. *Progress in Materials Science* 56(6):654-724.

147. Tian L, *et al.* (2012) Approaching the ideal elastic limit of metallic glasses. *Nature Communications* 3:609.

148. Wang C-C, *et al.* (2012) Sample size matters for Al88Fe7Gd5 metallic glass: Smaller is stronger. *Acta Materialia* 60(13-14):5370-5379.

149. Jang D & Greer JR (2010) Transition from a strong-yet-brittle to a stronger-and-ductile state by size reduction of metallic glasses. *Nature Materials* 9(3):215-219.

150. Fang JX, *et al.* (2012) Atomic Structure and Structural Stability of Sc(75)Fe(25) Nanoglasses. *Nano Letters* 12(1):458-463.

151. Şopu D, Albe K, Ritter Y, & Gleiter H (2009) From nanoglasses to bulk massive glasses. *Applied Physics Letters* 94(19):191911.

152. Ritter Y, Sopu D, Gleiter H, & Albe K (2011) Structure, stability and mechanical properties of internal interfaces in Cu64Zr36 nanoglasses studied by MD simulations. *Acta Materialia*.

153. Şopu D, Ritter Y, Gleiter H, & Albe K (2011) Deformation behavior of bulk and nanostructured metallic glasses studied via molecular dynamics simulations. *Physical Review B* 83(10):100202.

154. Phillips W (Amorphous Solids: Low Temperature Properties, 1981. (Springer, Berlin).

155. Weintraub H, *et al.* (1995) Through the glass lightly. *Science-AAAS-Weekly Paper Edition* 267(5204):1609-1618.

156. Shintani H & Tanaka H (2008) Universal link between the boson peak and transverse phonons in glass. *Nature Materials* 7(11):870-877.

157. Jakse N, Nassour A, & Pasturel A (2012) Structural and dynamic origin of the boson peak in a Cu-Zr metallic glass. *Physical Review B* 85(17):174201.

158. Malinovsky V & Sokolov A (1986) The nature of boson peak in Raman scattering in glasses. *Solid State Communications* 57(9):757-761.

159. Schober H (2004) Vibrations and relaxations in a soft sphere glass: boson peak and structure factors. *Journal of Physics: Condensed Matter* 16(27):S2659.

160. Laird B & Schober H (1991) Localized low-frequency vibrational-modes in a simple-model glass. *Physical Review Letters* 66(5):636-639.

161. Schober H & Oligschleger C (1996) Low-frequency vibrations in a model glass. *Physical Review B* 53(17):11469-11480.

162. Sheng H, Ma E, & Kramer M (2012) Relating dynamic properties to atomic structure in metallic glasses. *JOM* 64(7):856-881.

163. Derlet P, Maaß R, & Löffler J (2012) The Boson peak of model glass systems and its relation to atomic structure. *The European Physical Journal B-Condensed Matter and Complex Systems* 85(5):1-20.

164. Tan P, Xu N, Schofield A, & Xu L (2012) Understanding the low-frequency quasilocalized modes in disordered colloidal systems. *Physical Review Letters* 108(9).

165. Gaskell PH (2005) Medium-range structure in glasses and low-< i> Q</i> structure in neutron and X-ray scattering data. *Journal of Non-Crystalline Solids* 351(12):1003-1013.

166. Egami T (2007) Icosahedral order in liquids. *Journal of Non-Crystalline Solids* 353(32-40):3666-3670.

167. Egami T (2010) Understanding the properties and structure of metallic glasses at the atomic level. *JOM* 62(2):70-75.

168. Miracle DB, Egami T, Flores KM, & Kelton KF (2007) Structural aspects of metallic glasses. *MRS Bulletin* 32(08):629-634.

169. Frank F (1952) Supercooling of liquids. *Proceedings of the Royal Society of London. Series A, Mathematical and Physical Sciences*:43-46.

170. Shen YT, Kim TH, Gangopadhyay AK, & Kelton KF (2009) Icosahedral order, frustration, and the glass transition: Evidence from time-dependent nucleation and supercooled liquid structure studies. *Physical Review Letters* 102(5).

171. Hollandmoritz D, Herlach D, & Urban K (1993) Observation of the undercoolability of quasi-crystal-forming alloys by electromagnetic-levitation. *Physical Review Letters* 71(8):1196-1199.

172. Yang L, *et al.* (2012) Atomic-scale mechanisms of the glass-forming ability in metallic glasses. *Physical Review Letters* 109(10):105502.

173. Liu A, *et al.* (2013) Systematic mapping of icosahedral short-range order in a melt-spun Zr 36 Cu 64 metallic glass. *Physical Review Letters* 110(20):205505.

174. Cheng YQ, Ma E, & Sheng HW (2009) Atomic level structure in multicomponent bulk metallic glass. *Physical Review Letters* 102(24).

175. Li M, Wang CZ, Hao SG, Kramer MJ, & Ho KM (2009) Structural heterogeneity and medium-range order in Zr(x)Cu(100-x) metallic glasses. *Physical Review B* 80(18).

176. Mendelev M, Kramer M, Ott R, & Sordelet D (2009) Molecular dynamics simulation of diffusion in supercooled Cu-Zr alloys. *Philosophical Magazine* 89(2):109-126.

177. Li MZ, Wang CZ, Mendelev MI, & Ho KM (2008) Molecular dynamics investigation of dynamical heterogeneity and local structure in the supercooled liquid and glass states of Al. *Physical Review B* 77(18).

178. Sha Z, Feng Y, & Li Y (2010) Statistical composition-structure-property correlation and glass-forming ability based on the full icosahedra in Cu-Zr metallic glasses. *Applied Physics Letters* 96(6).

179. Cheng YQ, Cao AJ, & Ma E (2009) Correlation between the elastic modulus and the intrinsic plastic behavior of metallic glasses: The roles of atomic configuration and alloy composition. *Acta Materialia* 57(11):3253-3267.

180. Cheng YQ, Ma E, & Sheng HW (2008) Alloying strongly influences the structure, dynamics, and glass forming ability of metallic supercooled liquids. *Applied Physics Letters* 93(11).

181. Cheng YQ, Sheng HW, & Ma E (2008) Relationship between structure, dynamics, and mechanical properties in metallic glass-forming alloys. *Physical Review B* 78(1).

182. Nelson DR (1983) Order, frustration, and defects in liquids and glasses. *Physical Review B* 28(10):5515.

183. Iwashita T, Nicholson D, & Egami T (2013) Elementary excitations and crossover phenomenon in liquids. *Physical Review Letters* 110(20).

184. Wakeda M & Shibutani Y (2010) Icosahedral clustering with medium-range order and local elastic properties of amorphous metals. *Acta Materialia* 58(11):3963-3969.

185. Lee M, Lee CM, Lee KR, Ma E, & Lee JC (2011) Networked interpenetrating connections of icosahedra Effects on shear transformations in metallic glass. *Acta Materialia* 59(1):159-170.

186. Honeycutt JD & Andersen HC (1987) Molecular-dynamics study of melting and freezing of small Lennard-Jones clusters. *Journal of Physical Chemistry* 91(19):4950-4963.

187. Clarke AS & Jonsson H (1993) Structural-changes accompanying densification of random hard-sphere packings. *Physical Review E* 47(6):3975-3984.

188. Cheng YQ, Cao AJ, Sheng HW, & Ma E (2008) Local order influences initiation of plastic flow in metallic glass: Effects of alloy composition and sample cooling history. *Acta Materialia* 56(18):5263-5275.

189. Guthrie M*, et al.* (2004) Formation and structure of a dense octahedral glass. *Physical Review Letters* 93(11).

190. Krogh-Moe J (1969) The structure of vitreous and liquid boron oxide. *Journal of Non-Crystalline Solids* 1(4):269-284.

191. McMillan P & Piriou B (1983) Raman spectroscopic studies of silicate and related glass structure: a review. *Bulletin de Mineralogie* 106(1-2):57-75.

192. Cox JN & Armstrong JL (2002) *Structure and Composition of Glasses and Amorphous Materials by Vibrational Spectroscopy* (Wiley Online Library).

193. Greaves G (1985) EXAFS and the structure of glass. *Journal of Non-Crystalline Solids* 71(1):203-217.

194. Koyama A, Yamamoto T, Fukao K, & Miyamoto Y (2001) Molecular dynamics studies on local ordering in amorphous polyethylene. *Journal of Chemical Physics* 115(1):560-566.

195. Theodorou DN & Suter UW (1985) Detailed molecular structure of a vinyl polymer glass. *Macromolecules* 18(7):1467-1478.

196. Hui X*, et al.* (2008) Short-to-medium-range order in Mg65Cu25Y10 metallic glass. *Physics Letters A* 372(17):3078-3084.

197. Inoue A & Masumoto T (1993) Mg-Based Amorphous-Alloys. *Materials Science and Engineering a-Structural Materials Properties Microstructure and Processing* 173(1-2):1-8.

198. Inoue A, Ohtera K, Kita K, & Masumoto T (1988) New amorphous Mg-Ce-Ni alloys with high strength and good ductility. *Japanese journal of applied physics* 27(12A):L2248.

199. Luo WK, Sheng HW, & Ma E (2006) Pair correlation functions and structural building schemes in amorphous alloys. *Applied Physics Letters* 89(13).

200. Guan P, Fujita T, Hirata A, Liu Y, & Chen M (2012) Structural origins of the excellent glass forming ability of Pd 40 Ni 40 P 20. *Physical Review Letters* 108(17):175501.

201. Inoue A, Nishiyama N, & Masumoto T (1994) Synthesis and Properties of Mg-Based Amorphous Alloys. *Advanced Materials '93, Iii - a & B* 16(A & B):87-92.

202. Seidel M, Eckert J, ZuecoRodrigo E, & Schultz L (1996) Mg-based amorphous alloys with extended supercooled liquid region produced by mechanical alloying. *Journal of Non-Crystalline Solids* 207:514-517.

203. Ma H, Shi L-L, Xu J, & Ma E (2007) Chill-cast in situ composites in the pseudo-ternary Mg–(Cu, Ni)–Y glass-forming system: microstructure and compressive properties. *Journal of Materials Research* 22(02):314-325.

204. Puech S, Blandin J-J, & Soubeyroux J-L (2007) Mg based bulk metallic glasses with high mechanical strength and large viscoplastic forming capacity. *Advanced Engineering Materials* 9(9):764-768.

205. Soubeyroux JL, Gorsse S, & Orveillon G (2007) Glass formation range of Mg-based bulk metallic alloys. *Materials science forum*, (Trans Tech Publ), pp 2018-2025.

206. Zheng Q, Cheng S, Strader J, Ma E, & Xu J (2007) Critical size and strength of the best bulk metallic glass former in the Mg–Cu–Gd ternary system. *Scripta Materialia* 56(2):161-164.

207. Ma H, Zheng Q, Xu J, Li Y, & Ma E (2005) Doubling the critical size for bulk metallic glass formation in the Mg–Cu–Y ternary system. *Journal of Materials Research* 20(09):2252-2255.

208. Ma H, Shi L, Xu J, Li Y, & Ma E (2005) Discovering inch-diameter metallic glasses in three-dimensional composition space. *Applied Physics Letters* 87(18):181915-181915-181913.

209. Busch R, Bakke E, & Johnson WL (1998) Viscosity of the supercooled liquid and relaxation at the glass transition of the Zr46.75Ti8.25Cu7.5Ni10Be27.5 bulk metallic glass forming alloy. *Acta Materialia* 46(13):4725-4732.

210. Lewandowski JJ, Wang WH, & Greer AL (2005) Intrinsic plasticity or brittleness of metallic glasses. *Philosophical Magazine Letters* 85(2):77-87.

211. Jóvári P*, et al.* (2007) Atomic structure of glassy Mg_{60}Cu_{30}Y_{10} investigated with EXAFS, x-ray and neutron diffraction, and reverse Monte Carlo simulations. *Physical Review B* 76(5):054208.

212. Wang X, Lou H, Wang S, Xu J, & Jiang J (2011) Atomic packing in Mg61Cu28Gd11 bulk metallic glass. *Applied Physics Letters* 98(3):031901.

213. Bailey NP, Schiotz J, & Jacobsen KW (2004) Simulation of Cu-Mg metallic glass: Thermodynamics and structure. *Physical Review B* 69(14).

214. Widom M, *et al.* (2011) Elastic properties of Ca-based metallic glasses predicted by first-principles simulations. *Physical Review B* 84(5).

215. Kresse G & Furthmüller J (1996) Efficiency of ab-initio total energy calculations for metals and semiconductors using a plane-wave basis set. *Computational Materials Science* 6(1):15-50.

216. Kresse G & Joubert D (1999) From ultrasoft pseudopotentials to the projector augmented-wave method. *Physical Review B* 59(3):1758.

217. Blöchl PE (1994) Projector augmented-wave method. *Physical Review B* 50(24):17953.

218. Jiang Q, Chi B, & Li J (2003) A valence electron concentration criterion for glass-formation ability of metallic liquids. *Applied Physics Letters* 82(18):2984-2986.

219. Nagel S & Tauc J (1975) Nearly-free-electron approach to the theory of metallic glass alloys. *Physical Review Letters* 35(6):380.

220. Yu H, Wang W, & Bai H (2010) An electronic structure perspective on glass-forming ability in metallic glasses. *Applied Physics Letters* 96(8):081902-081902-081903.

221. Gu XJ, Poon SJ, Shiflet GJ, & Widom M (2008) Ductility improvement of amorphous steels: Roles of shear modulus and electronic structure. *Acta Materialia* 56(1):88-94.

222. Gilman JJ (2003) *Electronic basis of the strength of materials* (Cambridge University Press).

223. Silvi B & Savin A (1994) Classification of chemical-bonds based on topological analysis of Electron Localization Functions. *Nature* 371(6499):683-686.

224. Becke AD & Edgecombe KE (1990) A simple measure of electron localization in atomic and molecular systems. *The Journal of Chemical Physics* 92(9):5397-5403.

225. Xu M, Cheng YQ, Sheng HW, & Ma E (2009) Nature of atomic bonding and atomic structure in the phase-change Ge(2)Sb(2)Te(5) glass. *Physical Review Letters* 103(19).

226. Ogata S, Li J, & Yip S (2002) Ideal pure shear strength of aluminum and copper. *Science* 298(5594):807-811.

227. Bader RF (1990) *Atoms in molecules* (Wiley Online Library).

228. Henkelman G, Arnaldsson A, & Jonsson H (2006) A fast and robust algorithm for Bader decomposition of charge density. *Computational Materials Science* 36(3):354-360.

229. Ding J & Cheng Y (2014) Charge transfer and atomic-level pressure in metallic glasses. *Applied Physics Letters* 104(5):051903.

230. Takeuchi A & Inoue A (2005) Classification of bulk metallic glasses by atomic size difference, heat of mixing and period of constituent elements and its application to characterization of the main alloying element. *Materials Transactions* 46(12):2817-2829.

231. Allred A (1961) Electronegativity values from thermochemical data. *Journal of Inorganic and nuclear chemistry* 17(3):215-221.

232. Cohen MH & Turnbull D (1959) Molecular transport in liquids and glasses. *The Journal of Chemical Physics* 31(5):1164-1169.

233. Egami T & Srolovitz D (1982) Local structural fluctuations in amorphous and liquid metals: a simple theory of the glass transition. *Journal of Physics F: Metal Physics* 12(10):2141.

234. Nicholson D, Ojha M, & Egami T (2013) First-principles local stress in crystalline and amorphous metals. *Journal of Physics: Condensed Matter* 25(43):435505.

235. Wang WH, Dong C, & Shek CH (2004) Bulk metallic glasses. *Materials Science & Engineering R-Reports* 44(2-3):45-89.

236. Goldstein M (1976) Viscous liquids and the glass transition. V. Sources of the excess specific heat of the liquid. *The Journal of Chemical Physics* 64(11):4767-4774.

237. Martinez LM & Angell CA (2001) A thermodynamic connection to the fragility of glass-forming liquids. *Nature* 410(6829):663-667.

238. Wang D*, et al.* (2004) Bulk metallic glass formation in the binary Cu–Zr system. *Applied Physics Letters* 84(20):4029-4031.

239. Kelton KF*, et al.* (2003) First x-ray scattering studies on electrostatically levitated metallic liquids: Demonstrated influence of local icosahedral order on the nucleation barrier. *Physical Review Letters* 90(19).

240. Wessels V*, et al.* (2011) Rapid chemical and topological ordering in supercooled liquid Cu(46)Zr(54). *Physical Review B* 83(9).

241. Bendert J, Gangopadhyay A, Mauro N, & Kelton K (2012) Volume expansion measurements in metallic liquids and their relation to fragility and glass forming ability: an energy landscape interpretation. *Physical Review Letters* 109(18):185901.

242. Busch R, Kim YJ, & Johnson WL (1995) Thermodynamics and kinetics of the undercooled liquid and the glass-transition of the Zr41.2ti13.8cu12.5ni10.0be22.5 alloy. *Journal of Applied Physics* 77(8):4039-4043.

243. Coslovich D & Pastore G (2007) Understanding fragility in supercooled Lennard-Jones mixtures. I. Locally preferred structures. *The Journal of Chemical Physics* 127(12):124504.

244. Hentschel H, Ilyin V, & Procaccia I (2008) Nonuniversality of the specific heat in glass forming systems. *Physical Review Letters* 101(26):265701.

245. Pedersen UR, Schrøder TB, Dyre JC, & Harrowell P (2010) Geometry of slow structural fluctuations in a supercooled binary alloy. *Physical Review Letters* 104(10):105701.

246. Mauro N*, et al.* (2013) Anomalous structural evolution and liquid fragility signatures in Cu–Zr and Cu–Hf liquids and glasses. *Acta Materialia* 61(19):7411-7421.

247. Mauro N, Blodgett M, Johnson M, Vogt A, & Kelton K (2014) A structural signature of liquid fragility. *Nature Communications* 5.

248. Adam G & Gibbs JH (1965) On the temperature dependence of cooperative relaxation properties in glass‐forming liquids. *The Journal of Chemical Physics* 43(1):139-146.

249. Erpenbeck JJ (1984) Shear viscosity of the hard-sphere fluid via nonequilibrium molecular dynamics. *Physical Review Letters* 52(15):1333.

250. Kob W & Andersen HC (1995) Testing Mode-Coupling Theory for a Supercooled Binary Lennard-Jones Mixture - the Van Hove Correlation-Function. *Physical Review E* 51(5):4626-4641.

251. Kob W & Andersen HC (1995) Testing Mode-Coupling Theory for a supercooled binary Lennard-Jones mixture .2. Intermediate Scattering Function and dynamic susceptibility. *Physical Review E* 52(4):4134-4153.

252. Ke HB, Wen P, Zhao DQ, & Wang WH (2010) Correlation between dynamic flow and thermodynamic glass transition in metallic glasses. *Applied Physics Letters* 96(25).

253. Cowley J (1950) X‐Ray Measurement of Order in Single Crystals of Cu3Au. *Journal of Applied Physics* 21(1):24-30.

254. Iwashita T & Egami T (2012) Atomic mechanism of flow in simple liquids under shear. *Physical Review Letters* 108(19):196001.

255. Spaepen F (1977) A microscopic mechanism for steady state inhomogeneous flow in metallic glasses. *Acta metallurgica* 25(4):407-415.

256. Yavari AR, Lewandowski J, & Eckert J (2007) Mechanical properties of bulk metallic glasses. *MRS Bulletin* 32(08):635-638.

257. Rycroft CH (2009) VORO++: A three-dimensional Voronoi cell library in C++. *Chaos: An Interdisciplinary Journal of Nonlinear Science* 19(4):-.

258. Rycroft CH, Grest GS, Landry JW, & Bazant MZ (2006) Analysis of granular flow in a pebble-bed nuclear reactor. *Physical Review E* 74(2):021306.

259. Li J (2003) AtomEye: an efficient atomistic configuration viewer. *Modelling and Simulation in Materials Science and Engineering* 11(2):173.

260. Peng H, Li M, & Wang W (2011) Structural signature of plastic deformation in metallic glasses. *Physical Review Letters* 106(13):135503.

261. Guo W, Iwashita T, & Egami T (2014) Universal local strain in solid-state amorphization: The atomic size effect in binary alloys. *Acta Materialia* 68:229-237.

262. Zink M, Samwer K, Johnson WL, & Mayr SG (2006) Plastic deformation of metallic glasses: Size of shear transformation zones from molecular dynamics simulations. *Physical Review B* 73(17):172203.

263. Tomida T & Egami T (1993) Molecular-dynamics study of structural anisotropy and anelasticity in metallic glasses. *Physical Review B* 48(5):3048.

264. Ott R, Kramer M, Besser M, & Sordelet D (2006) High-energy X-ray measurements of structural anisotropy and excess free volume in a homogenously deformed Zr-based metallic glass. *Acta Materialia* 54(9):2463-2471.

265. Ott R*, et al.* (2008) Anelastic strain and structural anisotropy in homogeneously deformed Cu< sub> 64.5</sub> Zr< sub> 35.5</sub> metallic glass. *Acta Materialia* 56(19):5575-5583.

266. Rountree CL, Vandembroucq D, Talamali M, Bouchaud E, & Roux S (2009) Plasticity-induced structural anisotropy of silica glass. *Physical Review Letters* 102(19):195501.

267. Concustell A, Godard-Desmarest S, Carpenter MA, Nishiyama N, & Greer AL (2011) Induced elastic anisotropy in a bulk metallic glass. *Scripta Materialia* 64(12):1091-1094.

268. Zhang Y, Mattern N, & Eckert J (2011) Effect of uniaxial loading on the structural anisotropy and the dynamics of atoms of Cu(50)Zr(50) metallic glasses

within the elastic regime studied by molecular dynamics simulation. *Acta Materialia* 59(11):4303-4313.

269. Pan S, Qin J, Wang W, & Gu T (2011) Origin of splitting of the second peak in the pair-distribution function for metallic glasses. *Physical Review B* 84(9):092201.

270. Liu X*, et al.* (2010) Metallic liquids and glasses: atomic order and global packing. *Physical Review Letters* 105(15):155501.

271. Maloney C & Robbins M (2009) Anisotropic power law strain correlations in sheared amorphous 2D solids. *Physical Review Letters* 102(22):225502.

272. Lekka CE, Ibenskas A, Yavari A, & Evangelakis G (2007) Tensile deformation accommodation in microscopic metallic glasses via subnanocluster reconstructions. *Applied Physics Letters* 91:214103.

273. Marsaglia G (1972) Choosing a point from the surface of a sphere. *The Annals of Mathematical Statistics* 43(2):645-646.

274. Maloney CE & Lemaitre A (2006) Amorphous systems in athermal, quasistatic shear. *Physical Review E* 74(1).

275. Wang Z, Pan J, Li Y, & Schuh C (2013) Densification and Strain Hardening of a Metallic Glass under Tension at Room Temperature. *Physical Review Letters* 111(13):135504.

276. Pugh S (1954) XCII. Relations between the elastic moduli and the plastic properties of polycrystalline pure metals. *Philosophical Magazine* 45(367):823-843.

277. Mayr SG (2009) Relaxation kinetics and mechanical stability of metallic glasses and supercooled melts. *Physical Review B* 79(6).

278. Shi YF & Falk ML (2006) Atomic-scale simulations of strain localization in three-dimensional model amorphous solids. *Physical Review B* 73(21).

279. Çain T & Ray JR (1988) Third-order elastic constants from molecular dynamics: Theory and an example calculation. *Physical Review B* 38(12):7940.

280. Tsamados M, Tanguy A, Goldenberg C, & Barrat J-L (2009) Local elasticity map and plasticity in a model Lennard-Jones glass. *Physical Review E* 80(2):026112.

281. Yoshimoto K, Jain TS, Workum KV, Nealey PF, & de Pablo JJ (2004) Mechanical heterogeneities in model polymer glasses at small length scales. *Physical Review Letters* 93(17).

282. Harmon JS, Demetriou MD, Johnson WL, & Tao M (2007) Deformation of glass forming metallic liquids: Configurational changes and their relation to elastic softening (vol 90, art. no. 131912, 2007). *Applied Physics Letters* 91(2).

283. Dufresne A & Cavaille J (1998) Clustering and percolation effects in microcrystalline starch-reinforced thermoplastic. *Journal of Polymer Science Part B-Polymer Physics* 36(12):2211-2224.

284. Favier V, Dendievel R, Canova G, Cavaille J, & Gilormini P (1997) Simulation and modeling of three-dimensional percolating structures: case of a latex matrix reinforced by a network of cellulose fibers. *Acta Materialia* 45(4):1557-1565.

285. Fujita T*, et al.* (2009) Atomic-scale heterogeneity of a multicomponent bulk metallic glass with excellent glass forming ability. *Physical Review Letters* 103(7).

286. Mazzacurati V, Ruocco G, & Sampoli M (1996) Low-frequency atomic motion in a model glass. *EPL (Europhysics Letters)* 34(9):681.

287. Schober H & Laird BB (1991) Localized low-frequency vibrational modes in glasses. *Physical Review B* 44(13):6746.

288. Schober H & Ruocco G (2004) Size effects and quasilocalized vibrations. *Philosophical Magazine* 84(13-16):1361-1372.

289. Kaya D, Green N, Maloney C, & Islam M (2010) Normal modes and density of states of disordered colloidal solids. *Science* 329(5992):656-658.

290. Chen K*, et al.* (2011) Measurement of correlations between low-frequency vibrational modes and particle rearrangements in quasi-two-dimensional colloidal glasses. *Physical Review Letters* 107(10):108301.

291. Manning ML & Liu AJ (2011) Vibrational modes identify soft spots in a sheared disordered packing. *Physical Review Letters* 107(10):108302.

292. Xu N, Vitelli V, Liu A, & Nagel S (2010) Anharmonic and quasi-localized vibrations in jammed solids—Modes for mechanical failure. *EPL (Europhysics Letters)* 90(5):56001.

293. Widmer-Cooper A, Perry H, Harrowell P, & Reichman DR (2009) Localized soft modes and the supercooled liquid's irreversible passage through its configuration space. *The Journal of Chemical Physics* 131(19):194508.

294. Widmer-Cooper A, Perry H, Harrowell P, & Reichman DR (2008) Irreversible reorganization in a supercooled liquid originates from localized soft modes. *Nature Physics* 4(9):711-715.

295. Mosayebi M, Ilg P, Widmer-Cooper A, & Del Gado E (2014) Soft Modes and Nonaffine Rearrangements in the Inherent Structures of Supercooled Liquids. *Physical Review Letters* 112(10):105503.

296. Wyart M, Nagel S, & Witten T (2005) Geometric origin of excess low-frequency vibrational modes in weakly connected amorphous solids. *EPL (Europhysics Letters)* 72(3):486.

297. Mayr SG (2006) Activation energy of shear transformation zones: A key for understanding rheology of glasses and liquids. *Physical Review Letters* 97(19):195501.

298. Delogu F (2008) Atomic mobility and strain localization in amorphous metals. *Physical Review Letters* 100(7):075901.

299. Gale JD (1997) GULP: A computer program for the symmetry-adapted simulation of solids. *Journal of the Chemical Society, Faraday Transactions* 93(4):629-637.

300. Gale JD & Rohl AL (2003) The general utility lattice program (GULP). *Molecular Simulation* 29(5):291-341.

301. Rodney D & Schuh C (2009) Distribution of thermally activated plastic events in a flowing glass. *Physical Review Letters* 102(23):235503.

302. Ediger MD (2000) Spatially heterogeneous dynamics in supercooled liquids. *Annual Review of Physical Chemistry* 51:99-128.

303. Glotzer SC (2000) Spatially heterogeneous dynamics in liquids: insights from simulation. *Journal of Non-Crystalline Solids* 274(1-3):342-355.

304. Sillescu H (1999) Heterogeneity at the glass transition: a review. *Journal of Non-Crystalline Solids* 243(2-3):81-108.

305. Widmer-Cooper A, Harrowell P, & Fynewever H (2004) How reproducible are dynamic heterogeneities in a supercooled liquid? *Physical Review Letters* 93(13).

306. Matharoo GS, Razul MSG, & Poole PH (2006) Structural and dynamical heterogeneity in a glass-forming liquid. *Physical Review E* 74(5).

307. Kawasaki T & Tanaka H (2010) Structural origin of dynamic heterogeneity in three-dimensional colloidal glass formers and its link to crystal nucleation. *Journal of Physics-Condensed Matter* 22(23).

308. Andersen HC (2005) Molecular dynamics studies of heterogeneous dynamics and dynamic crossover in supercooled atomic liquids. *Proceedings of the National Academy of Sciences of the United States of America* 102(19):6686-6691.

309. Varnik F, Bocquet L, Barrat JL, & Berthier L (2003) Shear localization in a model glass. *Physical Review Letters* 90(9):95702.

310. Shi YF & Falk ML (2005) Structural transformation and localization during simulated nanoindentation of a noncrystalline metal film. *Applied Physics Letters* 86(1).

311. Shi YF & Falk ML (2007) Stress-induced structural transformation and shear banding during simulated nanoindentation of a metallic glass. *Acta Materialia* 55(13):4317-4324.

312. Murali P*, et al.* (2011) Atomic scale fluctuations govern brittle fracture and cavitation behavior in metallic glasses. *Physical Review Letters* 107(21).

313. Guan P, Lu S, Spector MJ, Valavala PK, & Falk ML (2013) Cavitation in amorphous solids. *Physical Review Letters* 110(18):185502.

314. Louzguine DV & Inoue A (2001) Electronegativity of the constituent rare-earth metals as a factor stabilizing the supercooled liquid region in Al-based metallic glasses. *Applied Physics Letters* 79(21):3410-3412.

315. Kumar V*, et al.* (2011) Atomic and electronic structure of Pd 40 Ni 40 P 20 bulk metallic glass from ab initio simulations. *Physical Review B* 84(13):134204.

316. Pang J, Tan M, & Liew K (2013) On valence electron density, energy dissipation and plasticity of bulk metallic glasses. *Journal of Alloys and Compounds* 577:S56-S65.

317. Mizutani U (1983) Electronic structure of metallic glasses. *Progress in Materials Science* 28(2):97-228.

318. Han G*, et al.* (2011) The< i> e</i>/< i> a</i> values of ideal metallic glasses in relation to cluster formulae. *Acta Materialia* 59(15):5917-5923.

319. Tang C & Harrowell P (2013) Anomalously slow crystal growth of the glass-forming alloy CuZr. *Nature Materials* 12(6):507-511.

320. Tanaka H (2005) Two-order-parameter model of the liquid-glass transition. I. Relation between glass transition and crystallization. *Journal of Non-Crystalline Solids* 351(43-45):3371-3384.

321. Tanaka H (2005) Two-order-parameter model of the liquid-glass transition. II. Structural relaxation and dynamic heterogeneity. *Journal of Non-Crystalline Solids* 351(43-45):3385-3395.

322. Tanaka H (2005) Two-order-parameter model of the liquid-glass transition. III. Universal patterns of relaxations in glass-forming liquids. *Journal of Non-Crystalline Solids* 351(43-45):3396-3413.

323. Watanabe K & Tanaka H (2008) Direct observation of medium-range crystalline order in granular liquids near the glass transition. *Physical Review Letters* 100(15).

324. Kawasaki T & Tanaka H (2010) Formation of a crystal nucleus from liquid. *Proceedings of the National Academy of Sciences of the United States of America* 107(32):14036-14041.

325. Leocmach A & Tanaka H (2012) Roles of icosahedral and crystal-like order in the hard spheres glass transition. *Nature Communications* 3.

326. Tanaka H (2011) Roles of bond orientational ordering in glass transition and crystallization. *Journal of Physics-Condensed Matter* 23(28).

327. Tanaka H, Kawasaki T, Shintani H, & Watanabe K (2010) Critical-like behaviour of glass-forming liquids. *Nature Materials* 9(4):324-331.

328. Tanaka H (2010) Bond orientational ordering in a metastable supercooled liquid: a shadow of crystallization and liquid-liquid transition. *Journal of Statistical Mechanics-Theory and Experiment*.

329. Singh S, Ediger M, & de Pablo JJ (2013) Ultrastable glasses from in silico vapour deposition. *Nature Materials* 12(2):139-144.

330. Yu HB, Luo Y, & Samwer K (2013) Ultrastable Metallic Glass. *Advanced Materials* 25(41):5904-5908.

331. Lyubimov I, Ediger MD, & de Pablo JJ (2013) Model vapor-deposited glasses: Growth front and composition effects. *The Journal of Chemical Physics* 139(14):144505.

Curriculum Vitae

Jun Ding was born in Taizhou, China on September 10, 1987. He entered Shanghai Jiao Tong University, Shanghai, China in 2006, and received his B.S. in Materials Science and Engineering in 2010. He joined Prof. En Ma's group as a graduate student at the Department of Materials Science and Engineering in Johns Hopkins University and worked on the "structure-property relationship in metallic glasses". He has earned his Master Degree in December 2012 and will graduate in 2014 with Ph.D degree in Materials Science and Engineering.